Phil. Trans. R. Soc. Lond. A **319**, 191–218 (1986) [191]
Printed in Great Britain

A MICROSTRUCTURAL STUDY OF THE OXIDATION OF Fe–Ni–Cr ALLOYS I. PROTECTIVE OXIDE GROWTH

BY S. B. NEWCOMB[1], W. M. STOBBS[1] AND E. METCALFE[2]

[1] *Department of Metallurgy and Materials Science, University of Cambridge, Pembroke Street, Cambridge CB2 3QZ, U.K.*

[2] *Central Electricity Research Laboratories, Technology Planning and Research Division, Central Electricity Generating Board, Kelvin Avenue, Leatherhead, Surrey KT22 7SE, U.K.*

(*Communicated by R. W. K. Honeycombe, F.R.S. – Received 5 February* 1985)

[Plates 1–16]

CONTENTS

The oxidation behaviour of a range of Fe–Ni–Cr alloys has been studied by correlating 'edge-on' TEM observations of the retained metal–oxide interface with data obtained by conventional low resolution techniques for studying oxidation. Results are presented for 'protective' scale formation on three Fe–20Cr–Ni alloys as oxidized at 600 °C in air and in 1% CO–CO_2. The temporal development of thin layers of chromium-rich sesquioxides in air was followed and it was shown that growth occurs by a process essentially dominated by the outward diffusion of chromium. Results

obtained by 'edge-on' TEM demonstrated that decreased chromium gradients in the alloy and higher chromium concentrations at the metal–oxide interface are associated with some inward development of the scale. These minor microstructural changes are paralleled by increases in the rate constants with a tendency towards cube law kinetics. A reverse trend in the mass gain data, as a function of the nickel content of the alloy was characterized for oxidation in 1 % CO–CO_2. Despite this, chemically similar oxides are seen to form although carbides were observed beneath the scales on the higher nickel content alloys. Significantly the trend with increasing nickel content was found to be paralleled by an increasing tendency for inward oxide growth. The iron activity in the alloy of lowest nickel content is sufficiently high for chemically unstable behaviour and the formation of duplex oxide nodules. Mechanisms by which simultaneous inward oxidation and carburization can take place during the formation of both chromium-rich sesquioxides and duplex spinel scales are discussed.

1. Introduction

Here and in an accompanying paper (Stobbs *et al.* 1986), hereafter referred to as II, we characterize the scaling behaviour of a range of Fe–Cr–Ni alloys oxidized at 600 °C in air and in CO–CO_2. While such alloys can exhibit several different modes of oxidation it is often difficult to determine the rate determining part of the scaling process. Indeed, we will find that several oxidation mechanisms would not appear to be as generally applicable as has been previously accepted. We have consequently chosen an essentially phenomenological classification procedure based on the morphologies and structures of the different scales observed. In this paper we use the term 'protective' to describe the oxidation behaviour of such alloys which is associated with a fundamentally *outward* growing scale. In II we apply the description 'non-protective' to those oxidation processes which are characterized by both an outward forming scale and *inward* oxidation relative to the original metal surface. The *inward* grown scales are described here and in II as either 'random inward' or 'orientated inward' oxides, the latter exhibiting epitaxial orientation relationships with the locally unoxidized alloy. Defined in this way such 'non-protective' processes are distinct from those occurring during 'breakaway' (see, for example, Goodison & Harris 1969).

While the work described here includes information obtained by conventional low resolution methods such as X-ray diffraction, SEM and mass gain data, the principal technique we have applied, in order to complete the phenomenological type of characterization described, is the transmission electron microscopy (TEM) of 'edge-on' oxidation specimens. The retained metal–oxide interface region is thereby examined in section allowing a full morphological, structural and compositional characterization of both the oxides and the underlying alloy in any given TEM foil. Such data, when correlated with the oxidation kinetics, provide a unique insight into the different types of oxidation behaviour which can occur as well as giving strong indications of its historical development. Some of our preliminary results on the oxidation of the FeCrNi alloys, obtained using the technique, have been presented previously (Newcomb & Stobbs 1982, 1983; Newcomb *et al.* 1983; Newcomb 1984).

The oxidation resistance of iron-based alloys can be improved by the addition of chromium. The Fe–Cr–O phase diagram at 1000 and 1300 °C (Seybolt 1960) indicates that at these temperatures it is the rhombohedral oxide, Cr_2O_3, with dissolved Fe_2O_3, which is in equilibrium with alloys containing more than 13 % chromium.† Since cationic diffusion through this oxide

† Unless otherwise indicated, all percentage compositions are by mass.

is slow (Hay *et al.* 1970; Kofstad 1972) its formation is generally regarded as protective (Kofstad 1972). However, when alloys containing less than 13% chromium are oxidized at high temperatures an $Fe_{3-x}Cr_xO_4$ $(0 < x < 2)$ spinel is formed rather than the α-$(Cr,Fe)_2O_3$ sesquioxide (Seybolt 1960). While the spinels are considered to be less protective than the sesquioxides, and several mechanisms have been proposed to explain the breakdown of protective scales (for example Caplan & Cohen 1959; Whittle & Wood 1967), no complete description has been given for the different types of oxidation process. Equally, although the oxide likely to be found under low temperature oxidation conditions can be predicted by the extrapolation of thermochemical data (Richardson *et al.* 1950; Majorandorany & Pehlke 1974) the only partial success of such an approach suggests the importance of kinetic rather than equilibrium criteria.

Most of the oxidation data in the literature is on high rate 'breakaway' behaviour and in this field surface-sensitive techniques such as XPS (Castle 1977), AES (Hultquist & Leygraf 1982), LEED (Leygraf & Hultquist 1975) and RHEED (Young & Mitchell 1979) have been used to gain information on the early stages of scale formation at low oxygen partial pressure or low oxidation temperatures. Many Fe–Cr–Ni alloys, however, are used in air and low O_2 partial pressure environments at temperatures between 500 and 600 °C, so that an understanding of the full temporal development of the scale is needed technologically.

The alloys chosen for examination in this investigation cover the maximum range of protective behaviour and, as shown superimposed on a Schaeffler diagram in figure 1, the quantity is the minimum required to be both representative of those of industrial importance and to allow parametrically interesting comparisons. The series, containing either 10 or 20% chromium with specific nickel concentrations ranging from 0 to 34%, allows the separate effects

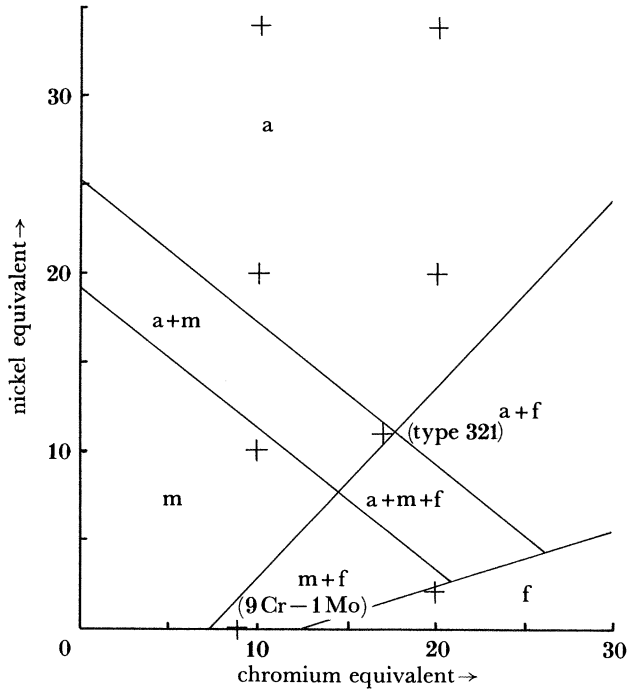

FIGURE 1. The compositions of the 10Cr and 20Cr alloys investigated here and in II superimposed on a Schaeffler diagram, as are the industrial 9Cr–1Mo and type 321 steels. a, austenite; m, martensite; f, ferrite. Nickel equivalent = percentage of Ni + 30 × percentage of C + 0.5 × percentage of Mn. Chromium equivalent = percentage of Cr + percentage of Mo + 1.5 × percentage of Si + 0.5 × percentage of Nb.

of the two additions to be examined as well as the role of the microstructure, some alloys being ferritic and others austenitic. The high-nickel and chromium austenitic alloys are of technological interest as fuel element cladding and sub-assembly wrapper materials in the prototype fast reactor while the types 321 and 9Cr–1Mo commercial steels are used in the power generation industry and allow further comparisons with the laboratory prepared ternary alloys. CO–CO_2 is used as a coolant in the advanced gas cooled reactors and an appropriate low oxygen partial pressure mixture (1 % CO–CO_2) was used as a comparison with the effects of air as the oxidizing medium. The oxidation temperature of 600 °C was used throughout and should both preclude the formation of wustite ($Fe_{1-x}O$) and lead to scales of 'non-breakaway' type, spinels being expected on the Fe–10Cr–Ni alloys and sesquioxides on the Fe–20Cr–Ni materials. The distinction we make here between 'non-protective' and 'protective' scales, despite both types of oxide formation often being regarded as protective (see for example Rowlands & Manning 1980; Wood & Whittle 1964), parallels the distinction made by Wood (1961) on the basis of mass gain characteristics.

2. Experimental details

The three alloys which exhibited characteristically 'protective' oxidation behaviour, and are thus described here, were prepared from 99.99 % pure starting materials under laboratory conditions. Their compositions are given in table 1. The descriptions which follow were made either for 20 × 10 × 3 mm coupons cut from rolled sheet or, in the case of the TEM results, for semi-circular rods. The specimens were ground to 1200 SiC paper and then vacuum annealed in an H_2–N_2 atmosphere for 30 min at 1050 °C. After a vacuum furnace cool they were then reground as above and thoroughly dried before being given their specified oxidation treatment. It should be noted that the coupons would be expected to exhibit of the order of a monolayer coverage of a room-temperature air-formed oxide before their prescribed high-temperature oxidation treatment. While one set of these specimens was oxidized in air at 600 °C, the other was oxidized at the same temperature in 1 % CO–CO_2 containing $1/10^6$ H_2 and $250/10^6$ H_2O at a pressure of 4.14 MPa.

Table 1. Chemical compositions of the Fe–Ni–Cr alloys (percentages by mass)

alloy	Fe	Cr	Ni	C
Fe–20Cr–2Ni(α)	balance	20.24	2.01	0.002
Fe–20Cr–20Ni(γ)	balance	20.63	19.5	0.003
Fe–20Cr–34Ni(γ)	balance	20.20	34.9	0.002

The general experimental approach taken here was based on a comparison of data obtained by conventional methods such as gravimetric analysis, X-ray diffractometry and optical and scanning electron microscopy, with more detailed TEM morphological and chemical studies of the temporal development of both the oxide scale and the underlying alloy structure. This made it essential to develop a reliable technique for the preparation of 'edge-on' thin foil TEM specimens of the various zones across the oxidation interface. The techniques are discussed in more detail elsewhere (Newcomb *et al.* 1985) but were based on the use of nickel plating to protect the fragile oxide formed on semi-cylinders of the metal which were then electroplated together to form a rod. Discs 3 mm in diameter were subsequently cut from this rod and thin

areas at the interface region were produced by a combination of electropolishing and ion beam milling.

Electron micrographs showing the typical microstructures of the three alloys, after their 30 min 1050 °C heat treatment, are shown in figure 2, plate 1. The films were prepared by standard electropolishing techniques using an electrolyte of 10% perchloric acid in 70% ethanol and 20% glycerol operated at 32 V and −5 °C. It may be seen that the microstructure of each alloy, as observed well away from the surface of the heat treated specimens, is as would be expected from the Schaeffler diagram (figure 1) and is consistent with diffraction patterns inset with the micrographs in figure 2. The respective structures and grain sizes are summarized in table 2, where the lattice parameter data presented were obtained by X-ray diffractometry

TABLE 2. SUMMARY OF THE MICROSTRUCTURAL DATA FOR THE Fe–20Cr–Ni ALLOYS BEFORE OXIDATION

alloy	structure		lattice parameter/nm	grain size/μm
	TEM	XRD		
Fe–20Cr–2Ni	α	α	0.287±0.001	30
Fe–20Cr–20Ni	γ	γ	0.359±0.001	20
Fe–20Cr–34Ni	γ	γ	0.359±0.001	20

These data are included to allow a comparison with the changes of sub-scale structure which can occur for some alloys as a function of the oxidation treatment (see tables 6 and 7).

and are consistent with values given for such alloys in the literature (Cook & Brown 1952). Since the microstructural relationship of the oxide to the underlying alloy is often of importance the surface regions of the specimens were also examined in 'edge-on' TEM specimens after the 1050 °C H_2–N_2 heat treatment and the final surface grinding treatment. It was found that the heat treatment in the H_2–N_2 atmosphere could result in the surface regions becoming nitrided as is shown for the Fe–20Cr–20Ni alloy in figure 3, plate 2. The large chromium-rich nitrides were formed, in this case, in a band some 5 μm thick at a depth of about 25 μm and the alloy was found to exhibit chromium depletion (to in this case 16%) to a depth of some 2 μm beneath this band. The final abrasion treatment of the surface was sufficient to remove the nitrided layer. In some cases this had a strong effect on the subsequent oxidation behaviour of the alloy as was evidenced by gross differences in oxidation behaviour of the ground diametric and unground circumferential surfaces of the semicircular section specimens used for the TEM investigation. For example, the Fe–10Cr–34Ni specimen as oxidized in air (and discussed in detail in II) was fully covered by an outward growing haemetite scale where the chromium depleted surface layer had not been ground off, while the ground surface was only partly so covered.

3. EXPERIMENTAL RESULTS

Results obtained by the more conventional techniques of gravimetric analysis, X-ray diffractometry and optical and scanning electron microscopy are presented together, for both oxidation treatments, in §§3 (*a*)–(*d*). The results we have obtained using 'edge-on' transmission electron microscopy are given for oxidation in air and in CO–CO_2 in §§3 (*e*) and (*d*) respectively.

(*a*) *Oxidation kinetics*

The oxidation kinetics were examined for each alloy in the two environments by gravimetry, coupons being weighed after 125, 500 and 1000 h oxidation as well as after 1500 h for the $CO–CO_2$ atmosphere. Logarithmic plots of the time against mass gain information thus obtained are shown in figure 4 where diffusion controlled oxidation by parabolic kinetics would yield mass gain increases following the $n = 2$ line. It is apparent, however, from figure 4 (*a*) that the specimens oxidized in air are common in following rather slower kinetics approximating

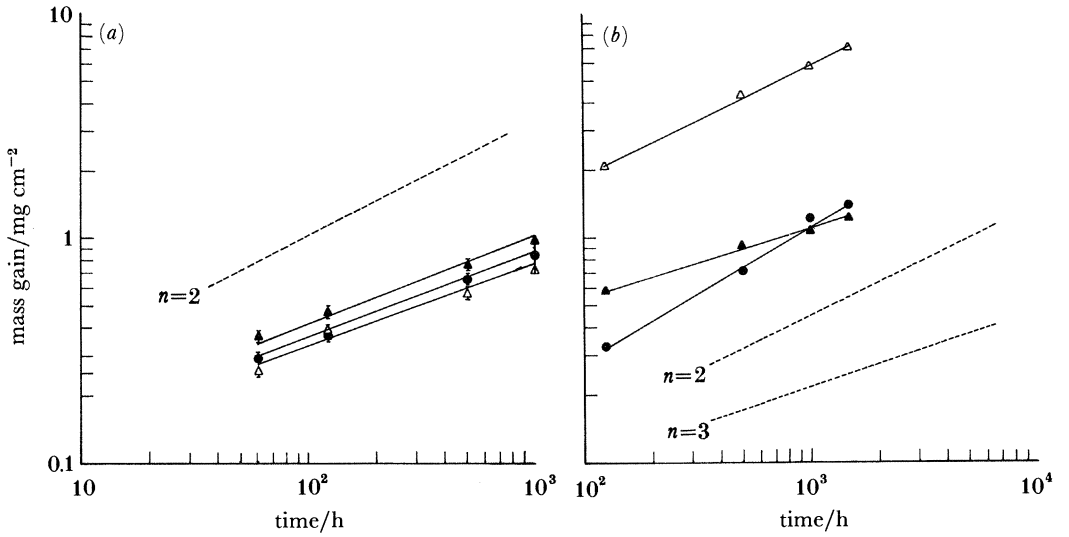

FIGURE 4. Weight gain curves for the Fe–20Cr–Ni alloys oxidized at 600 °C in (*a*) air and (*b*) 1 % $CO–CO_2$. △, Fe–20Cr–2Ni; ●, Fe–20Cr–20Ni; ▲, Fe–20Cr–34Ni.

to the $n = 3$ line. Weight gains after 1000 h, the measured n values and rate constants are presented in table 3 by using k_c and for comparison with other data on more artificial values of $k_p/(g^2\ cm^{-4}\ s^{-1})$. Consistency checks were made between the mass gain data and scale thickness measurements as obtained by 'edge-on' TEM assuming the formation of compact Cr_2O_3 scales. This was partially because of the problems associated with the spalling which was evident for these alloys as oxidized in air. Thus both the mass gain data and the scale thickness measurements, when oxidizing in air, indicated that an *increase* in nickel content is associated with an *increase* in the mass gains whether the alloy microstructure is austenitic or ferritic.

Turning to the data obtained for oxidation in 1 % $CO–CO_2$, both the 20 and 2Ni alloys follow approximately parabolic kinetics, although the ferritic alloy in this case undergoes much larger mass gains (figure 4*b*). The 34Ni alloy, however, again follows nearly cube law kinetics (Kubaschewski & Hopkins 1967) and the rate constant for this alloy in $CO–CO_2$ is given in table 3 as k_c. Comparing the mass-gain behaviour of the 20 and 34Ni alloys, as oxidized in air and in $CO–CO_2$, we see that after short oxidation times the same tendency is apparent in both environments (i.e. an increase in Ni content being associated with an increase in the mass gain) while a reverse trend is seen after longer oxidation times. In all cases, except that of the Fe–20Cr–2Ni as oxidized in $CO–CO_2$, the mass-gain data was consistent with the trends seen in the protective scale thicknesses, though when oxidizing in $CO–CO_2$ approximately 30 % of

TABLE 3. MASS GAINS AND OXIDATION RATE CONSTANTS FOR THE Fe–20Cr–Ni ALLOYS OXIDIZED IN AIR AND IN 1% CO–CO_2 AT 600 °C

(*a*) *air*

alloy	mass gain in 1000 h/mg cm^{-2}	n	$k_p/(g^2\ cm^{-4}\ s^{-1})$	$k_c/(g^3\ cm^{-6}\ s^{-1})$
Fe–20Cr–2Ni	0.72	2.53	1.44×10^{-13}	1.04×10^{-16}
Fe–20Cr–20Ni	0.83	2.47	1.91×10^{-13}	1.59×10^{-16}
Fe–20Cr–34Ni	0.96	2.32	2.56×10^{-13}	2.46×10^{-16}

(*b*) 1% CO–CO_2

			$k_n/[(g\ cm^{-2})^n\ s^{-1}]$
Fe–20Cr–2Ni	7.34	2.01	1.42×10^{-11}
Fe–20Cr–20Ni	1.42	1.53	1.73×10^{-14}
Fe–20Cr–34Ni	1.08	3.20	8.93×10^{-17}

(*c*) *Values of parabolic rate constants,* $k_p/(g^2\ cm^{-4}\ s^{-1})$ *for* Cr *and* Fe–Cr *alloys oxidized in oxygen*

material	temperature/°C	$k_p/(g^2\ cm^{-4}\ s^{-1})$	reference
Cr	750	1.1×10^{-13}	Mortimer & Post (1968)
Fe–50Cr	750	1.7×10^{-13}	Mortimer & Post (1968)
Fe–26Cr	870	1.7×10^{-13}	Caplan & Cohen (1965)
Fe–20Cr	650	1.3×10^{-14}	Mortimer & Sharp (1968)

he mass-gain appeared to be associated with the carbide formation observed by 'edge-on' EM. The mass-gain data for the 2Ni alloy oxidized in CO–CO_2 cannot be treated as if implying single type of oxidation process since this material exhibited fairly extensive nodule formation with the associated formation of duplex oxide layers (§3(*f*)). Nevertheless, the marked change n behaviour of this ferritic alloy on oxidizing in CO–CO_2 indicates the relatively greater effect of the alloy microstructure for this oxidizing atmosphere.

(*b*) X-*ray diffraction data*

All the oxidation specimens were studied by X-ray diffractometry after oxidation periods of 125, 500 and 1000 h. The lattice parameters of the α-M_2O_3 oxides formed in air on the three alloys are given as a function of time in table 4. There is a common trend with increasing oxidation time and nickel content in the 20 and 34Ni alloys for a decrease in both *a* and *c*. This would be consistent with an associated increase in chromium content of the scales. The same temporal trend is seen for the 2Ni alloy thereby suggesting a higher gradient of chromium content in the scale with thickness (see figure 15). While variations in oxide chemistry with

TABLE 4. LATTICE PARAMETERS (NANOMETRES) OF THE OXIDES FORMED ON THE Fe–20Cr–Ni ALLOYS AFTER OXIDATION IN AIR AT 600 °C

(More complete data, including results obtained as a function of time, have been presented previously (see Newcomb 1983).)

time/h ...	lattice parameter/nm 125 α-M_2O_3		500 α-M_2O_3		1000 α-M_2O_3	
alloy	a_H[a]	c_H[a]	a_H	c_H	a_H	c_H
Fe–20Cr–2Ni	[b]	[b]	0.4994	1.3612	0.4971	1.3605
Fe–20Cr–20Ni	0.4998	1.3617	0.4995	1.3613	0.4981	1.3606
Fe–20Cr–34Ni	0.4991	1.3611	0.4984	1.3602	0.4970	1.3601

[a] Indexing based on equivalent hexagonal unit cell.
[b] Oxide too thin for accurate lattice parameter measurement.

depth in the scale are difficult to assess by X-ray techniques, changes of this type may be followed more easily by energy dispersive X-ray analysis of 'edge-on' TEM foils. Disregarding for the present any such changes in structure with thickness, the X-ray data for the 20Cr–2Ni alloy suggest that at 500 h the oxide has a Cr:Fe ratio of about 50:50 whereas that after 1000 h the cationic Fe percentage has fallen to 13–22%. Energy dispersion spectroscopy (EDS) analysis of TEM 'edge on' foils of this specimen (see §3(*e*)), over depths which would be sampled in the X-ray structural analysis, demonstrated Fe concentrations in the scale of between 16 and 28%.

The lattice parameters of the oxides formed in 1% CO–CO_2 after 1000 h are shown in table 5. While minor concentrations of a cubic spinel were identified on the two lower Ni content

TABLE 5. LATTICE PARAMETERS OF THE OXIDES FORMED ON THE Fe–20Cr–Ni ALLOYS AFTER OXIDATION IN 1% CO–CO_2 FOR 1000 h AT 600 °C

(The primary data from which these results were obtained have been presented previously (Newcomb 1983).)

	lattice parameter/nm		
	α-M_2O_3		M_3O_4
alloy	a_H[a]	c_H[a]	a_0
Fe–20Cr–2Ni	0.4995	1.3620	0.8355
Fe–20Cr–20Ni	0.4965	1.3604	0.8341
Fe–20Cr–34Ni	0.4959	1.3604	—

[a] Indexing based on equivalent hexagonal unit cell.

alloys the major oxide was again the rhombohedral α-M_2O_3 phase. The lattice parameters for this oxide on the different alloys indicated that whereas in CO–CO_2 the scales on the 2Ni alloy contained a lower chromium fraction than when oxidized in air, the reverse trend was observed for the two higher Ni content alloys. In fact while the X-ray data suggested an iron content for the M_2O_3 of about 10% in these latter alloys, EDS analysis indicated a still lower figure of only about 2% after 1000 h oxidation.

It thus appears that when oxidation is 'protective' reducing the oxidation potential generally favours the selective oxidation of chromium, relative to iron. The exception to this general trend is exhibited by Fe–20Cr–2Ni which, as we have already indicated, behaves partly 'non-protectively' despite exhibiting apparently parabolic kinetics.

(*c*) *Optical metallography*

Cross-sectional specimens of the alloys were examined optically after 1000 h oxidation treatments. The micrograph in figure 5*a*, plate 2, showing the scale formed in air on Fe–20Cr–20Ni, demonstrates the typically thin and adherent nature of the M_2O_3 oxides formed under such conditions. Thicker scales were observed on the specimens oxidized in CO–CO_2 in a manner which is consistent with the mass gain data (see §3(*a*)) given the carbide formation beneath the scale for the two higher Ni content alloys. An optical micrograph of the Fe–20Cr–34Ni specimen as oxidized in CO–CO_2 is shown in figure 5*b*. The specimen was etched in aqueous sodium cyanide for 30 s to show the carbide distribution which may be seen to a depth of some 5 μm beneath the scale. That no such general carbide formation was seen in the ferritic 2Ni alloy again suggests the importance of kinetic criteria. Rather than the low solubility of carbon encouraging carbide precipitation it would appear that significant general diffusion into the material is hindered, presumably because of the low concentration gradients which can be attained (but see II).

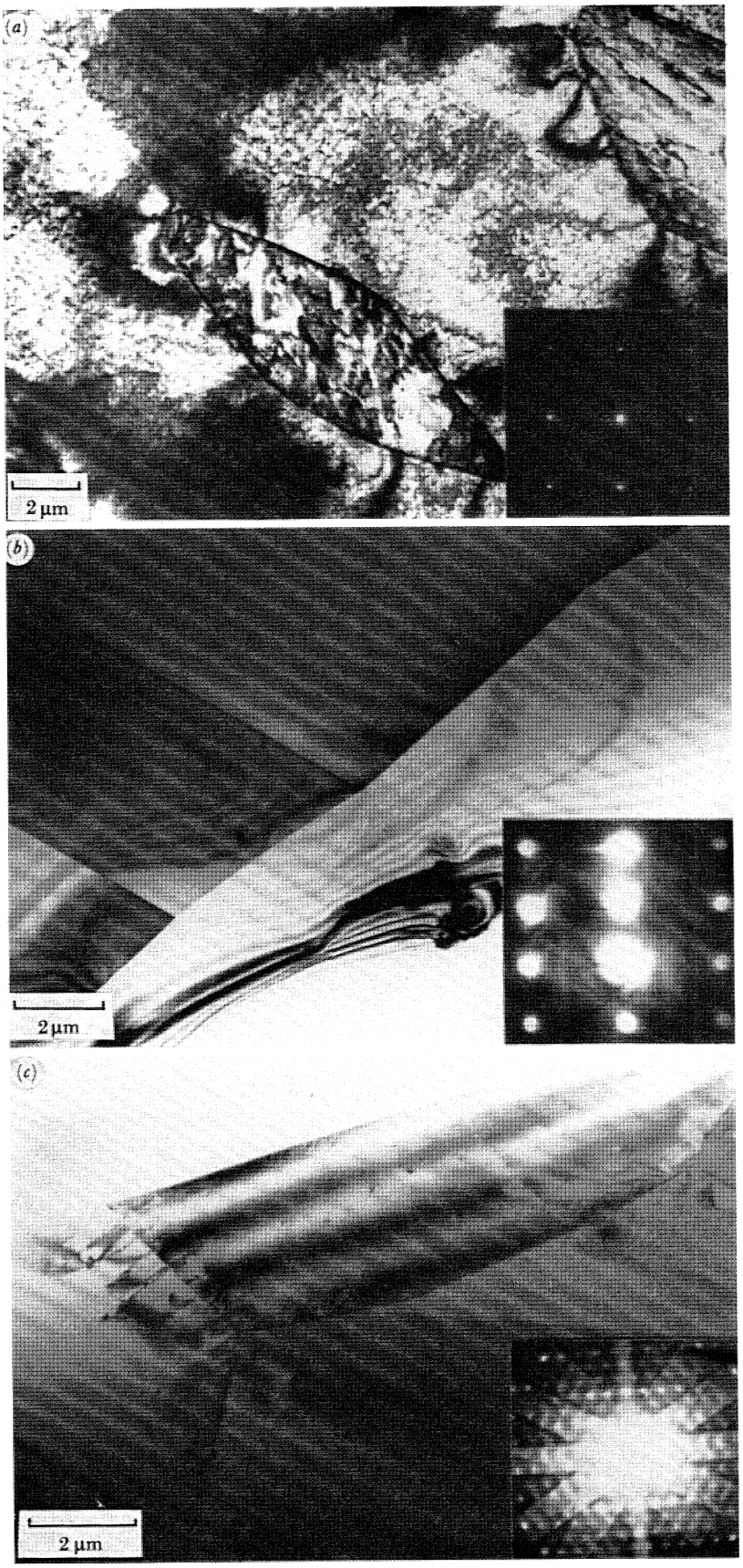

FIGURE 2. Microstructures of the Fe–20Cr–Ni alloys before oxidation. BF TEM. (*a*) Fe–20Cr–2Ni diffraction plane: $(001)_\alpha$; (*b*) Fe–20Cr–20Ni diffraction plane: $(112)_\gamma$; (*c*) Fe–20Cr–34Ni diffraction plane: $(112)_\gamma$.

(*Facing p.* 198)

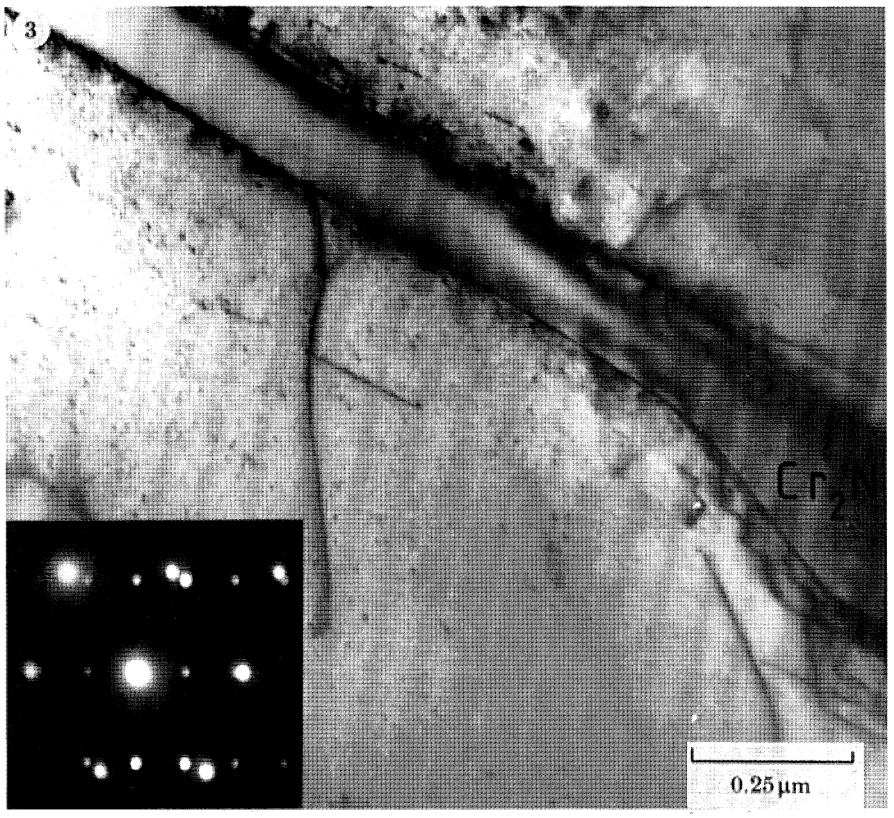

FIGURE 3. A β-Cr_2N nitride lying *ca.* 25 μm beneath the surface of an Fe–20Cr–20Ni alloy after the surface treatment described in the text. The bright-field micrograph was obtained near to the $(110)_\gamma|(2\bar{1}\bar{1}0)_{Cr_2N}$ normals shown in the inset diffraction pattern.

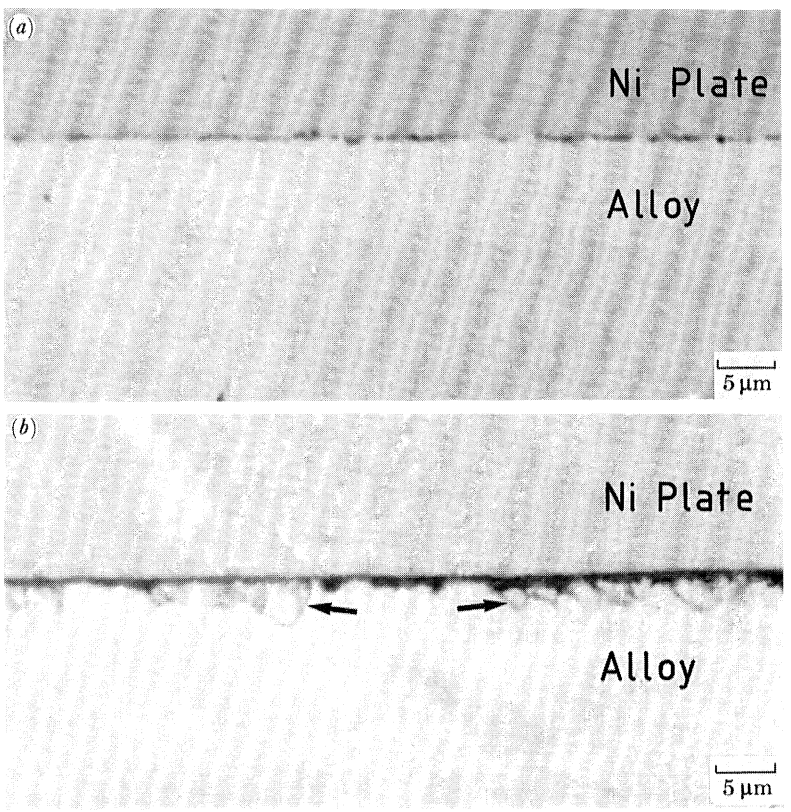

FIGURE 5. Optical micrographs of the scales formed after 1000 h oxidation at 600 °C on: (*a*) Fe–20Cr–20Ni in air and (*b*) Fe–20Cr–34Ni in 1 % CO–CO_2. Regions of the alloy beneath the scale where carbide precipitation has occurred are arrowed.

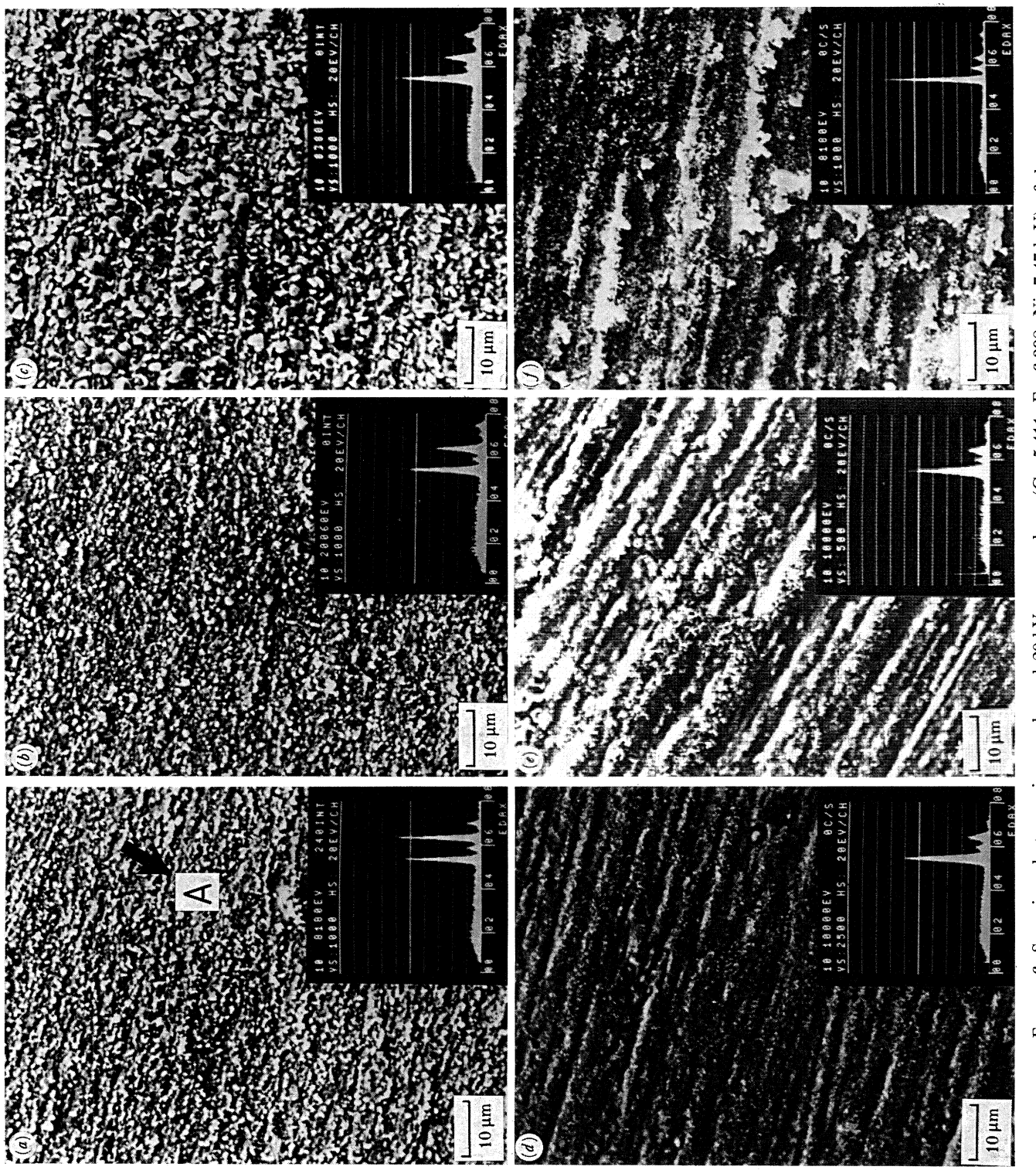

FIGURE 6. Scanning electron micrographs and 20 kV EDX analyses (Cr: 5.411, Fe: 6.398, Ni: 7.47 keV) of the surfaces of the oxides formed in air (*a*)–(*c*) and in CO–CO_2 (*d*)–(*f*) for 1000 h at 600 °C.

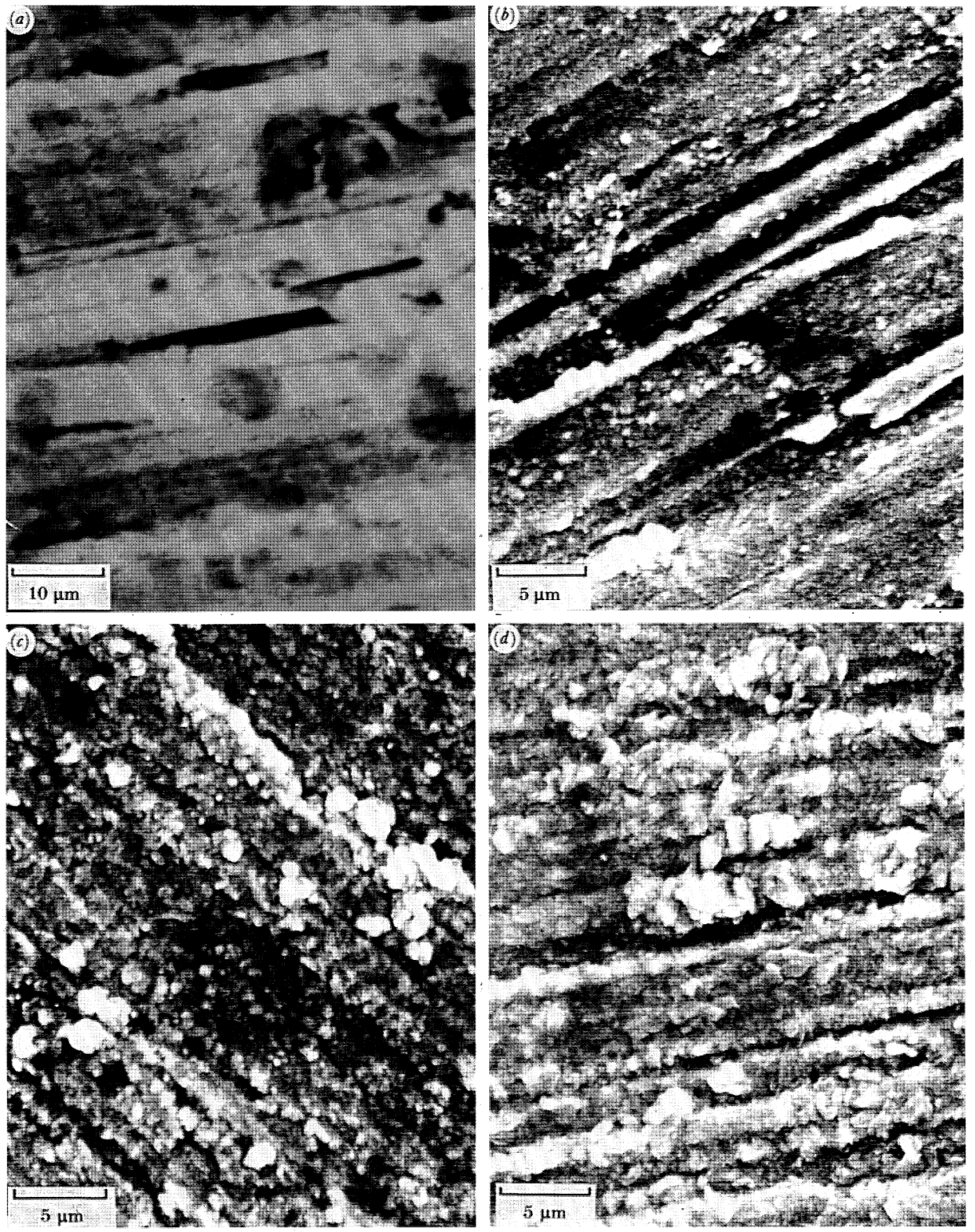

FIGURE 7. Scanning electron micrographs of the Fe–20Cr–34Ni alloy (*a*) before oxidation and the surface the oxides formed after (*b*) 30 min, (*c*) 2 h and (*d*) 17.5 h in air at 600 °C. It may be noted that the post-anneal grinding treatment is reflected in the form of the developing scale.

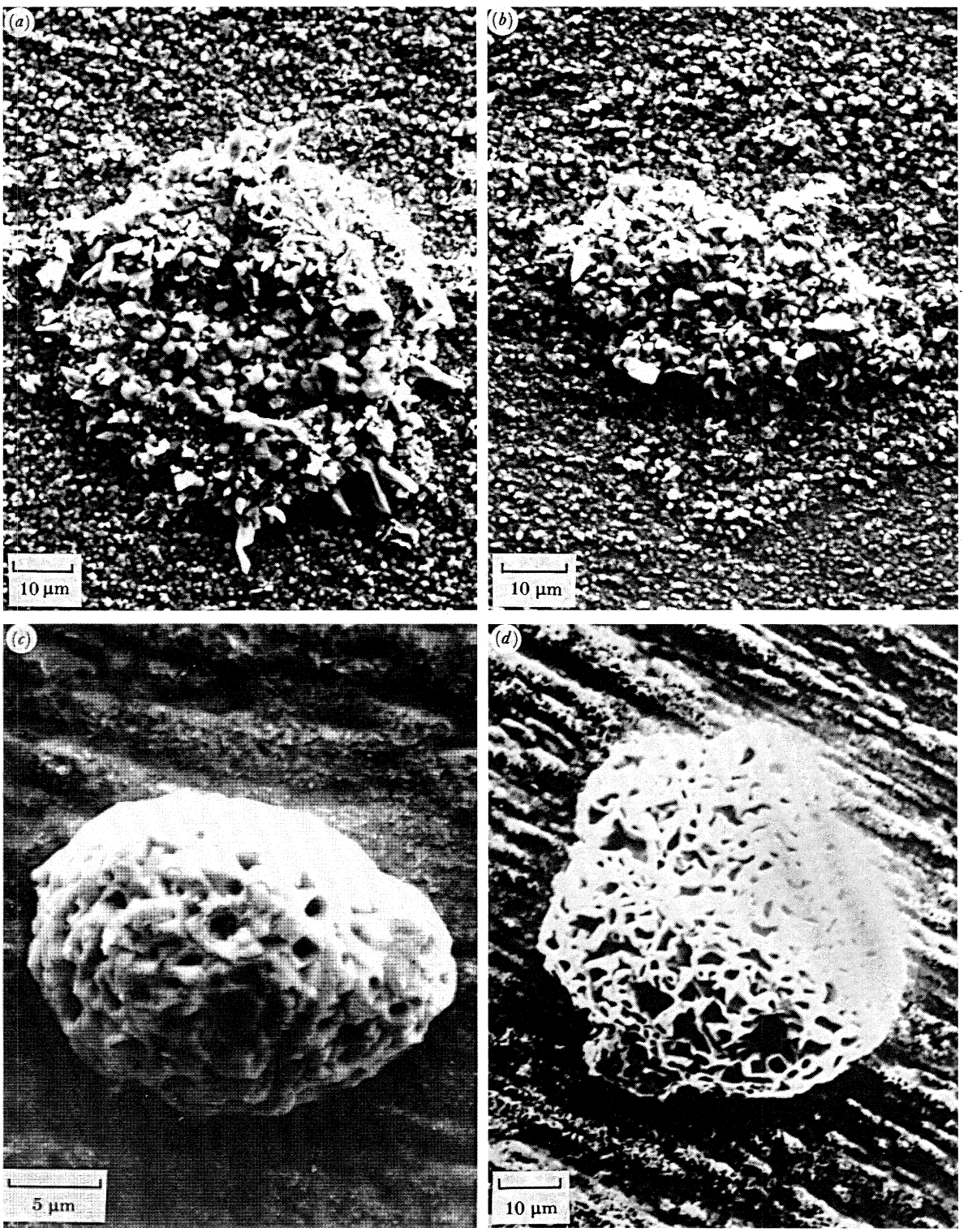

FIGURE 8. Scanning electron micrographs showing the morphologies of oxide nodules formed on (*a*) Fe–20Cr–2Ni and (*b*) Fe–20Cr–20Ni in air, and on (*c*) Fe–20Cr–2Ni and (*d*) Fe–20Cr–20Ni in CO–CO_2 after 1000 h at 600 °C.

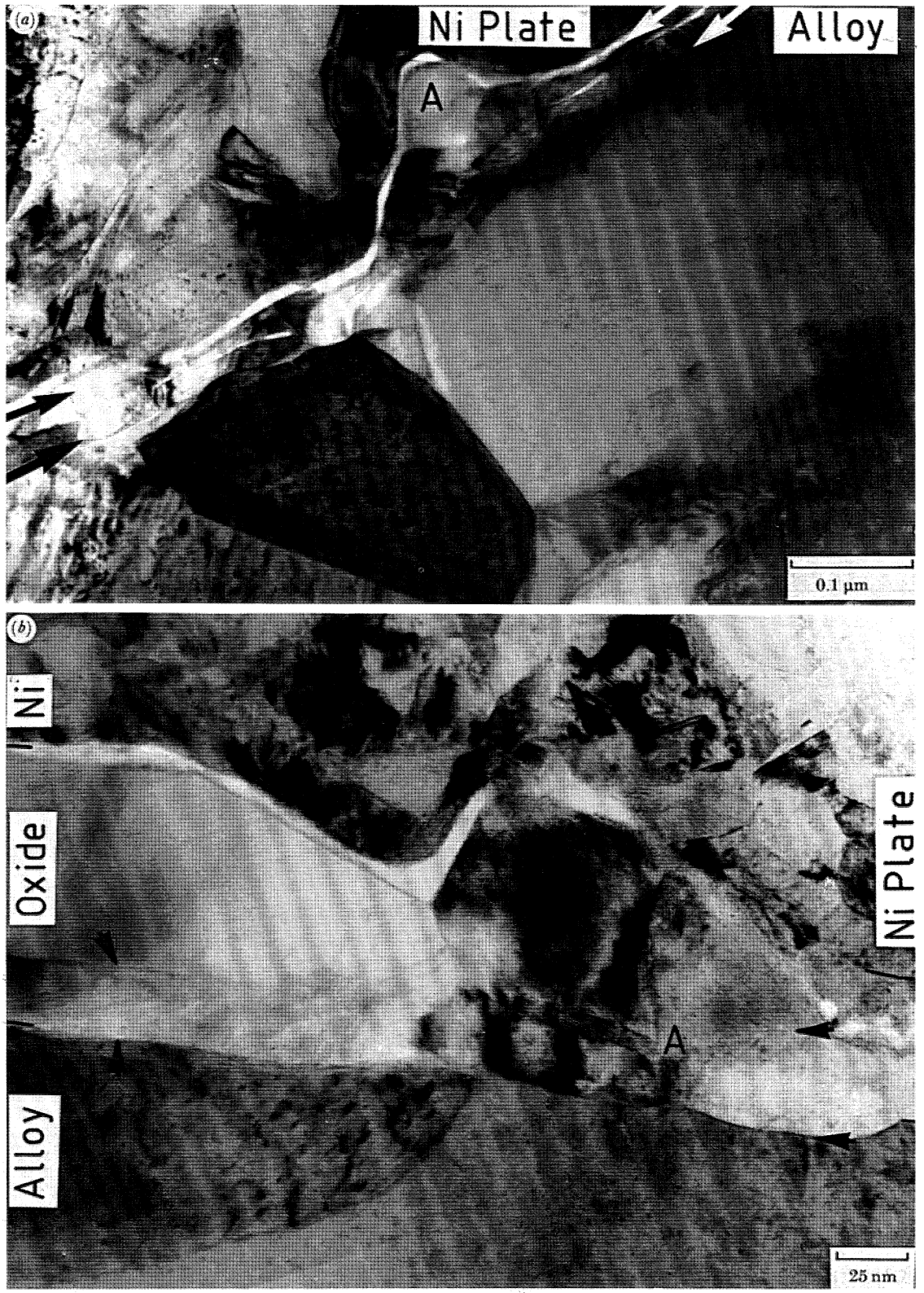

FIGURE 9. Fe–20Cr–34Ni oxidized for 6 h in air at 600 °C. 'Edge-on' bright-field micrographs showing (*a*) a low magnification image of a thin oxide layer (M_2O_3) sandwiched between the alloy and nickel plate, as arrowed (note the relatively fine alloy grains immediately beneath the scale); (*b*) a higher magnification image of the two-layered oxide morphology where the thinner and innermost layer is delineated by arrows (note the cusped morphology of the scale at the alloy–oxide and oxide–nickel plate interfaces).

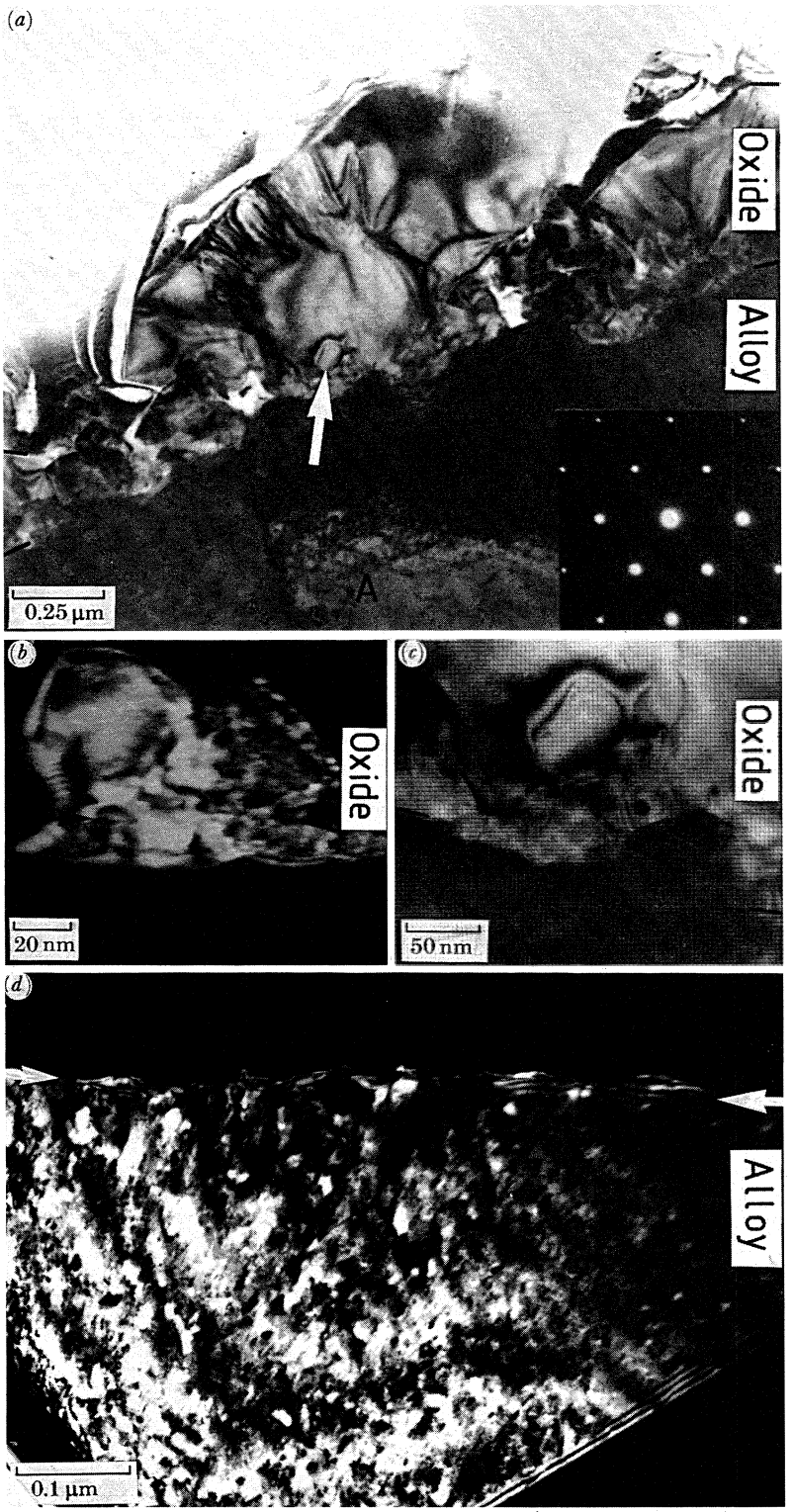

FIGURE 10. Fe–20Cr–34Ni oxidized for 1000 h in air at 600 °C. 'Edge-on' TEM. (*a*) Bright-field micrograph showing large faceted Cr_2O_3 grains and the underlying alloy (the inset is a (011) austenite diffraction pattern) which in some regions is dislocated, as at A. A 75 nm oxide grain near the metal–oxide interface is arrowed. (*b*) Dark-field micrograph showing the two-layered morphology of the scale. An interface between the oxide layers is arrowed. (*c*) Higher magnification image of fine grained oxide at the metal–oxide interface, bright field. (*d*) Dark-field micrograph demonstrating the more fully recovered alloy microstructure beneath the scale. The arrows delineate the metal–oxide interface, which is both inclined and clearly cusped.

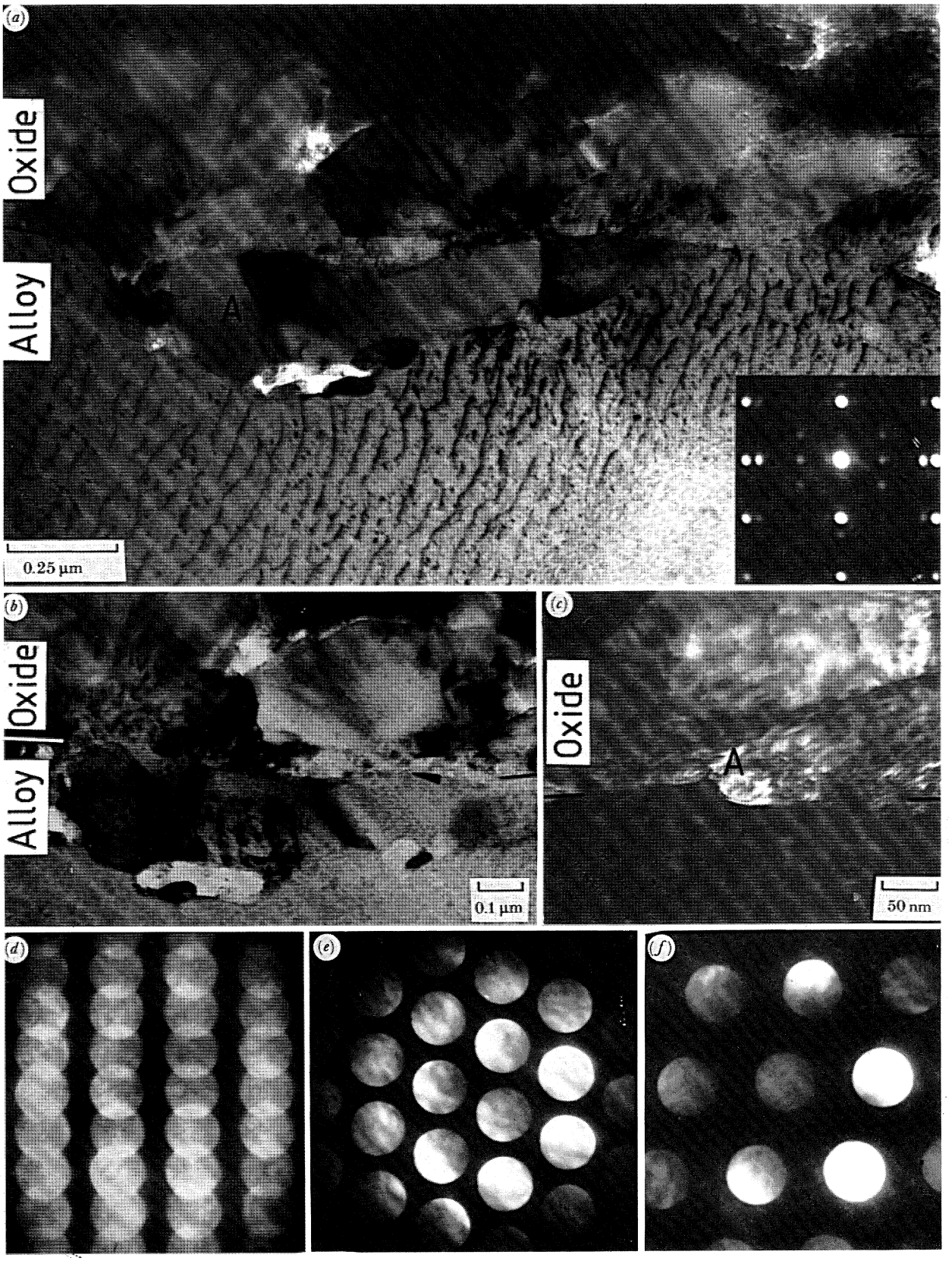

FIGURE 12. Fe–20Cr–20Ni oxidized in air for 1000 h at 600 °C. (*a*) Bright-field micrograph of the scale and underlying oxide. The outer surface of the faceted oxide grains are covered with sputter contamination from the ion beam milling while the surface of the alloy is partly oxidized, as demonstrated by the inset $(112)_{\gamma}//(112)_{M_3O_4}$ diffraction pattern. (*b*) The metal–oxide interface where a discrete layer (*ca.* 50 nm) of fine-grained oxide is arrowed, bright-field. (*c*) Dark-field micrograph showing the cusped morphology of the scale at the metal–oxide interface, as at A. (*d*) $(211)_{Cr_2O_3}$ diffraction pattern. (*e*) (011) austenite diffraction pattern taken from the fine-grained alloy immediately beneath the oxide, as at A in (*a*).

(*d*) *Scanning electron microscopy*

The relative inhomogeneities of the scale developments on the different specimens as well as the temporal development of coarse features such as the oxide grain size were followed by scanning electron microscopy.

The micrographs shown in figure 6, plate 3 are of the upper surfaces of all three alloys as oxidized for 1000 h in air (figure 6*a–c*) and in $CO–CO_2$ (figure 6*d–f*). Considering firstly the air oxidized specimens, it may be seen that as the Ni content is increased so is the grain size from about 0.5–1.0 μm at 2Ni to about 1.5–2.0 μm at 34Ni. The generally thin nature of the scales is demonstrated both by the retention of scratch features such as at A in figure 6*a* and by the accelerating voltage dependence of the EDS analysis. The analyses shown in figure 6 were all obtained at 20 kV, and the measured Cr:Fe ratio for the 20Cr–2Ni alloy changed from about 1:1 to 3:2 and 6:1 on reducing the beam voltage to 15 and 10 kV respectively. Similar trends in the analyses were found for the other air oxidized specimens and while the data could be analysed to give an approximate cation distribution for the scales, this was not done given the more accurate analyses obtained for the 'edge-on' TEM specimens. Comparison of even the above figures with the data presented in § (*e*) demonstrates the general dangers associated with making any inferences on surface oxide chemistry from the essentially bulk averaged analyses obtained by SEM.

Turning to figure 6*d–f*, we see that although there are no striking differences in the upper oxide surfaces formed in $CO–CO_2$ as a function of the alloy structure, the tendency to a general coarsening of oxide features with increased Ni content is clear. The major change observed as a function of the change in oxidizing atmosphere is associated with the change in form of the M_2O_3 to a fine needle morphology.

The temporal development of the grain size at the upper surface of the air formed scale was followed for the Fe–20Cr–34Ni alloy mainly to provide corroborative data for the size distribution found by TEM observation of the 'edge-on' specimens. The scanning electron micrographs in figure 7*a–d*, plate 4 show the upper surface of this alloy before oxidation and after 0.5, 2 and 17.5 h oxidation respectively. While the grain size observed after 0.5 h is between 100 and 200 nm, some 500 nm grains can be seen after 2 h. After 17.5 h the smaller grains are no longer apparent and the larger grains have coarsened to between 500 and 1000 nm.

A general tendency to heterogeneous development of the oxide scale was found for both environments, oxide nodules being formed with decreasing frequency as the nickel content is increased. A nodule formed on Fe–20Cr–2Ni in air is shown in figure 8*a*, plate 5. It has a diameter of about 50 μm and a larger grain size (*ca.* 1.5–2 μm) than that seen in the oxide matrix (*ca.* 0.5–1 μm). The lower number of nodules formed on the Fe–20Cr–20Ni (figure 8*b*) had a very similar appearance to those formed on the ferritic alloy. While no nodules formed on the Fe–20Cr–34Ni alloy oxidized in $CO–CO_2$, those that formed in this atmosphere on the lower Ni alloys had a characteristically 'hopper' morphology (figures 8*c*, *d*). These nodules are similar to the hopper oxide formed on Fe–9Cr (Harrison 1976) and exhibited only an iron peak on EDS analysis suggesting that they were magnetite (cf. table 5).

(e) The transmission electron microscopy of the air formed scales

(i) Fe–20Cr–34Ni(γ)

'Edge-on' foils of the oxide and underlying alloy were prepared for the 20Cr–34Ni alloy as oxidized in air after 6 and 1000 h to examine the temporal development of the scale. A low magnification image of the specimen oxidized for 6 h is shown in figure 9*a*, plate 6. The nickel plate used to protect the upper surface of the oxide is retained and can be seen above the oxide layer. It will be noted that the grain size in this upper region of the austenite is locally markedly smaller than in bulk (cf. table 2) as might be expected given the pre-oxidation abrasion and subsequent partial recrystallization of the upper surface. The scale is generally uniformly thin and adherent with a morphology normally taken to be typical of an outward growing oxide, though it does exhibit some local protuberances, as at A in figure 9*a*. Selected area diffraction indicated that the scale was α-Cr_2O_3 and it can be seen in the higher magnification image shown in figure 9*b* that a two-layered morphology has developed with finer grains at the metal–oxide interface which often exhibits moirés with the larger outer grains where there is overlap, as at A in figure 9*b*. The thickness of the inner more fine grained regions was 20 nm while the outer larger grained region was 40–50 nm thick. It can also be seen from this micrograph that the oxide grains have a cusped morphology at *both* the metal–oxide and the oxide–gas interfaces. Such a cusped morphology at the inner surface of an essentially outward growing scale is normally taken to be associated with limited inward growth taking place to fill the volume left by the outward diffusing cations (Wagner 1956). No preferential oxidation of the alloy is however apparent at alloy grain boundaries as is seen in the Fe–10Cr–Ni alloys and discussed in II.

Figure 10*a*, plate 7, showing the oxide formed on this alloy after 1000 h, demonstrates the typical development of an essentially outward growing scale which is now *ca.* 0.6 μm thick. Large (*ca.* 2 μm) faceted M_2O_3 grains may be observed growing above a finer distribution at the metal–oxide interface, as arrowed in figure 10*a* and shown enlarged in figure 10*b*, *c*. These grains are 20–50 nm in thickness and should be compared with the 20 nm grains observed after 6 h oxidation (figure 9*b*). Whereas we saw partial alloy recrystallization after 6 h oxidation it can now be seen that the alloy microstructure beneath the scale is more fully recovered as demonstrated in figure 10*d*, which is a dark field micrograph of the austenite immediately beneath the scale and also shows the cusped morphology of the alloy–oxide interface. In some areas, however, the recrystallized zone immediately beneath the oxide was seen to be heavily dislocated (figure 10*a*). While the sizes of the outer grains correlate well with SEM observations (§3.4), it would appear that the size of the grains in the inner layer has increased marginally over the oxidation period. This, as well as the cusped form of the smaller inner grains and the fact that no interface of the larger outer grains with the metal has been observed strongly suggests that at least some inward oxide development has taken place. A sufficient area of scale was characterized for possible interfaces of the outer larger grains with the metal surface to have been seen, if they existed, as expected on the basis of the standard model for the overgrowth of preferentially oriented grains nucleated at the original surface. It should be emphasized however that the form of this minimal inward oxidation is very different from that seen in the 'non-protective' scales described in II.

The cation concentrations in both the larger and smaller oxide grains were determined by EDS and results obtained as a function of depth are shown in figure 11. The cation concentrations

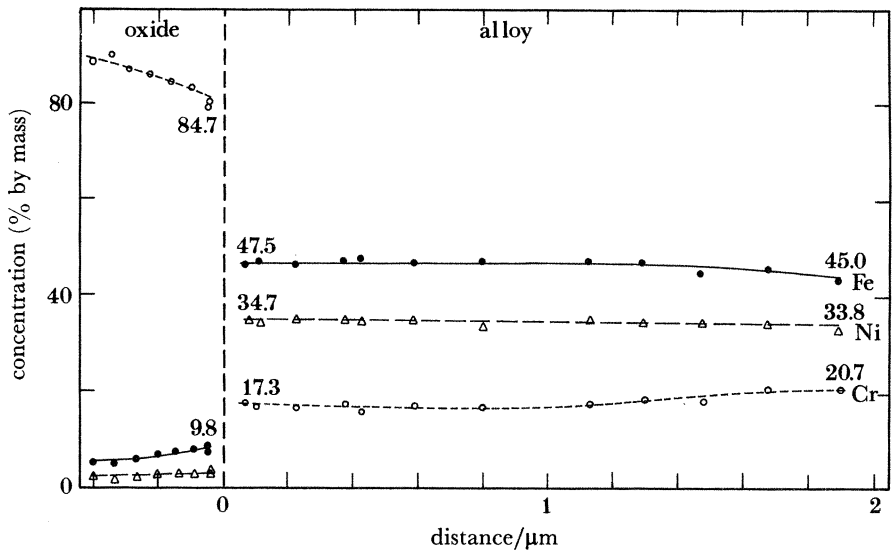

FIGURE 11. Composition profiles for Fe–20Cr–34Ni and the scale formed in air after 1000 h at 600 °C. This and all the other composition profiles shown were obtained by using a fixed total count, and at a count rate minimizing the counting chain dead time. The probe size used was *ca.* 15 nm, but since many of the analyses were obtained in material *ca.* 100 nm in thickness the effective probe size should be treated as having been *ca.* 30 nm. The total count was always such that the statistical error for a total of N counts gave a standard deviation of $N^{\frac{1}{2}}$. No corrections were, however, made for fluorescence or absorption. Thus, while the absolute values should be treated with caution the trends as a function of position are meaningful.

of Cr, Fe and Ni in the outer part of the scale were found to be 88, 9 and 2% respectively while the inner fine oxide had only a marginally higher iron and lower chromium content. This could be explained either on the basis of cationic exchange (Meijerling 1971) or on limited inward growth as would seem more likely given the points noted above. Examining the elemental concentrations in the alloy below the scale it can be seen that the nickel concentration was essentially flat to a point as near to the oxide interface as it could be measured despite nickel being at an extremely low concentration in the scales. There is however an approximately 3% chromium depletion layer in the alloy to a depth of about 1.5 μm.

(ii) Fe–20Cr–20Ni(γ)

The oxide which formed on Fe–20Cr–20Ni was similar to that seen on the 20Cr–34Ni alloy and typical of 'protective' scaling. It was examined 'edge-on' after 1000 h by which time it was about 0.5 μm in thickness (figure 12*a*, plate 8), rather thinner than the scale on the 20Cr–34Ni alloy as is consistent with the mass gain data (table 3). The bright field micrograph in figure 12*b* illustrates the typically faceted morphology of the outward growing grains and also shows a thin (*ca.* 50 nm) layer of finer grained oxide at the metal–oxide interface, as arrowed. Dark field images of the inmost fine oxide grains showed that again they had a cusped morphology at the metal–oxide interface (figure 12*c*). Microdiffraction was used to show that both the coarse and fine grained oxide had the α-M_2O_3 structure (figure 12*d*, *e*).

Most regions of the alloy beneath the scale showed a fully recrystallized morphology of austenite with a grain size of *ca.* 30 μm as observed prior to the surface abrasion and oxidation treatments (cf. figure 2*b*). However, fine grained (*ca.* 200 nm) austenite was retained in some areas, sandwiched between the oxide and coarser grained matrix (see figure 12*a*, *b*), in an only

partially recovered state, though with some recrystallization twinning. A microdiffraction pattern of a grain in such a region, as marked in figure 12*a*, is shown in figure 12*f*. This *retained* alloy microstructure is distinct from that occasionally developed in the *recrystallized* subscale regions of the Fe–20Cr–34Ni alloy. Compositional analysis (figure 13) of these fine grained regions of the austenite, immediately beneath the oxide, showed that they were *not* depleted in chromium as were the adjacent fully recrystallized grains which exhibited slightly greater depletion, but to a similar depth, than the 20Cr–34Ni alloy. It may also be seen from figure 13 that the cation concentrations in the outer part of the scale are 88% Cr, 8% Fe and 2% Ni. On this material the finer grained layers of the scale at the metal–oxide interface had a significantly higher iron and lower chromium concentration than the similar regions seen on the 20Cr–34Ni alloy (cf. figure 11).

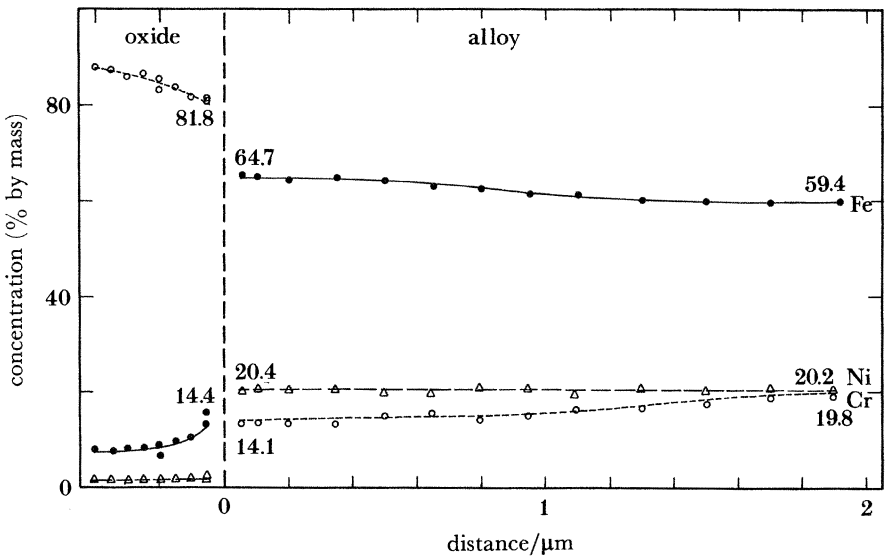

FIGURE 13. Composition profiles for Fe–20Cr–20Ni and the scale formed in air after 1000 h at 600 °C.

The contrast seen in the alloy matrix beneath the scale is associated with the formation of a surface oxide during the ion beam thinning process. As demonstrated by the diffraction pattern inset in figure 12*a* this oxide has the M_3O_4 structure and has grown epitaxially on the austenite. Although the precise oxidation conditions associated with the thinning of this specimen are not known, it is significant that M_3O_4 was seen covering the entire matrix as well as over the 1.5 μm deep chromium depleted region of the metal–oxide interface. We have not examined the very early stages of the oxidation of this alloy under the controlled oxidation conditions used for the abraded coupons so it is not known whether or not a similar layer of M_3O_4 was the first formed oxide on the abraded upper surface prior to the development of the M_2O_3. If such a very fine layer had been retained after extended oxidation of the coupon it would have been difficult to characterize because of the contaminant oxide formed during the thinning process. Attempts to observe such a layer were however unsuccessful, while comparisons of dark field images of the M_2O_3 grains adjacent to the matrix with similar images of the alloy strongly suggested that no M_3O_4 layer was present. This further supports the idea that the oxide scale develops into the metal to some extent as oxidation proceeds.

(iii) Fe–20Cr–2Ni(α)

The microstructure of the 'protective' oxide formed on the ferritic Fe–20Cr–2Ni alloy after 1000 h is shown in figure 14*a*, plate 9. The oxide layer which is 0.4–0.5 μm thick consists of relatively large faceted M_2O_3 oxide grains, above a smaller grain size distribution at the metal–oxide interface. The outer grain size was somewhat smaller than that of the oxide formed on the austenitic alloys as was noted by SEM (see § 3*d*). The metal–oxide interface again has a cusped morphology which is demonstrated in the dark field micrograph (imaged with a ferrite reflection) shown in figure 14*b*, while the alloy immediately beneath the scale is dislocated, as was observed in 20Cr–34Ni (figure 10*a*). EDS analysis (figure 15) showed that the oxide was again chromium rich but with a somewhat higher Cr concentration in the *outer* regions of the scale than the two previous austenitic alloys. The composition profiles at the base of the oxide and in the alloy depletion region, which was again 1.5–2.0 μm thick, had higher gradients than were observed in the austenitic alloys (compare figure 15 with figures 11 and 13).

Essentially we see a trend through the 20Cr alloys for the chromium gradient in the metal beneath the scale to increase as the nickel content is decreased. This is associated both with increasing gradients in the scales to higher outer scale chromium content and with decreased mass gains.

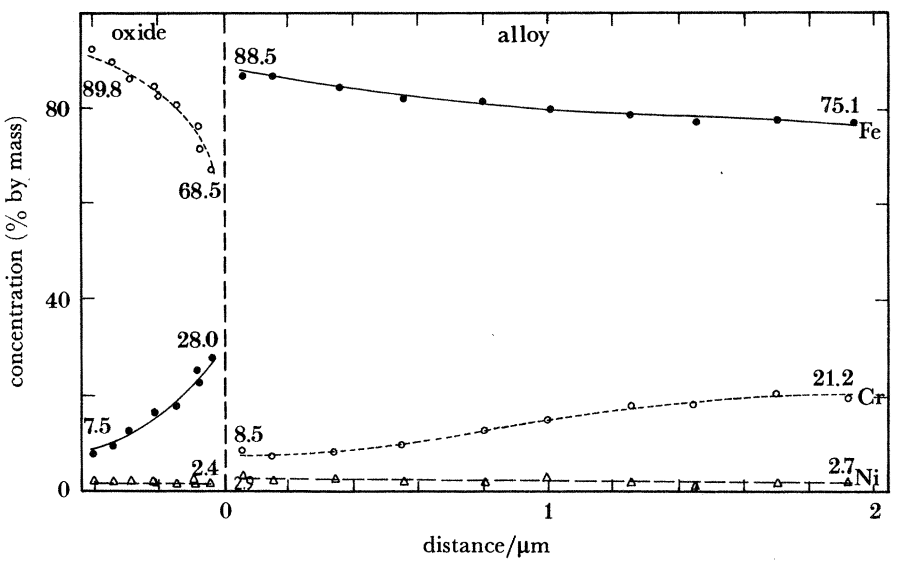

FIGURE 15. Composition profiles for Fe–20Cr–2Ni and the scale formed in air after 1000 h at 600 °C. Note the comparatively steep iron and chromium gradients in the scale (cf. figures 11 and 13).

(*f*) *The transmission electron microscopy of the scales formed in* 1 % CO–CO_2

(i) Fe–20Cr–34Ni(γ)

The microstructure of the 0.5–0.6 μm thick adherent and protective scale formed on this alloy in CO–CO_2 after 1000 h is shown in figure 16*a*, plate 10. The oxide is fine grained (*ca.* 50 nm) but with some variation in morphology towards the oxide–gas interface where the grains appear less equiaxed and more needle like. Selected area diffraction (figure 16(*b*)) indicated that the scale was α-M_2O_3. High resolution examination of the M_2O_3 needles revealed both a tendency

for the retention of non-planar twin boundaries, presumably facilitating the outward diffusion of chromium and that some porosity is retained as the grains coalesce (Newcomb *et al.* 1983).

The metal–oxide interface itself is shown at a higher magnification in figures 16*c* and *d*. No extensive inward oxidation is evident, though there are indications, as for example in the cusped morphology evident in figure 16*d*, that the oxide has grown a little into the alloy, as it did in air. The particles imaged and arrowed in figure 16*c*, however are not an inner oxide but sputter material deposited from the copper based beam blanks and tantalum specimen plates during the ion beam thinning process, as was confirmed by EDS analysis.

The austenite immediately beneath the scale is particularly interesting in that it exhibits, to a well defined depth of between 3 and 5 μm, a lower dislocation density than the substructure at greater depths, as well as more recrystallization twinning than was observed when the same alloy was oxidized in air. A micrograph of this region is shown in figure 17, plate 11. It should be noted that such a change in the recrystallization behaviour is consistent with the inward diffusion of a solute inhibiting grain boundary migration (Lucke & Stuwe 1971). While no carbides were observed at the twin boundaries normal to the metal–oxide interface or anywhere within the scale, large $M_{23}C_6$ carbides may be seen to have formed both at and beneath this 'recovery' zone. EDS analysis of the carbides showed their cation composition to be typically 78% Cr, 18% Fe and 4% Ni. The general cation composition both of the scale (which had a very uniform catonic composition of 97% Cr, 1.5% Fe and 0.5% Ni) and of the chromium depletion layer beneath it is shown in figure 18. Comparison of the composition profiles for this

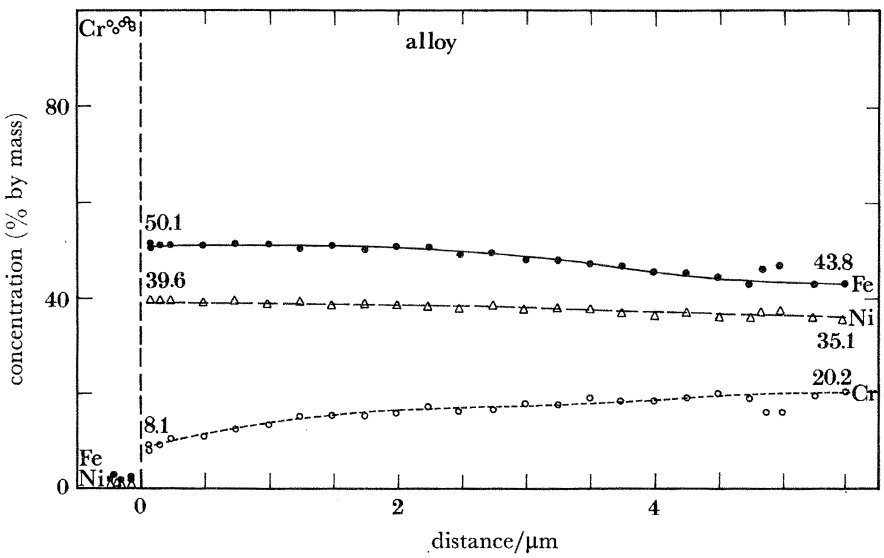

FIGURE 18. Composition profiles for Fe–20Cr–34Ni and the scale formed in 1% CO–CO_2 after 1000 h at 600 °C. The localized depletion of chromium to carbides in the alloy should be noted.

material as oxidized in air (figure 11) and in CO–CO_2 (figure 18) indicates that the chromium content of the scale is markedly higher when formed in the low oxygen potential environment and that the depletion in the alloy is both higher and considerably more extended, apparently to the base of the 'recovery' zone where carbide formation is first seen.

(ii) Fe–20Cr–20Ni(γ)

The oxide and substructure of this alloy, after 1000 h exposure in the CO–CO_2 atmosphere, are shown in figure 19, plate 12. The adherent and 'protective' Cr_2O_3 is only between 0.25 and 0.3 μm in thickness which suggests, given comparisons of the mass gains and SEM scale images for this and the 34Ni alloy, that much of the more open, needle-like outer part of the scale was not retained in the preparation of the 'edge-on' foil. We see however that, as for the 34Ni alloy, there is again a well defined recrystallization zone beneath the scale though this now extends for only about 1 μm into the alloy. The morphology of the scale in the region of the metal–oxide interface is shown in figure 20*a*, plate 13. While the regions nearer to the oxide–gas interface exhibit the needle like forms seen on the 20Cr–34Ni alloy, the grains nearer to the alloy interface are more equiaxed giving the appearance of a two-layered scale. Microdiffraction was used to identify the structure of the oxide here as that of α-Cr_2O_3 (see inset diffraction pattern in figure 20*a*). The lack of any specific orientation relationship between the equiaxed inner oxide grains and the alloy beneath it suggests that any inward growth is, even if more extensive than in the 34Ni alloy, still minimal. That such inward development is occurring is however further supported by evidence for a stepped cationic concentration change between the inner and outer oxide layers (see figure 21).

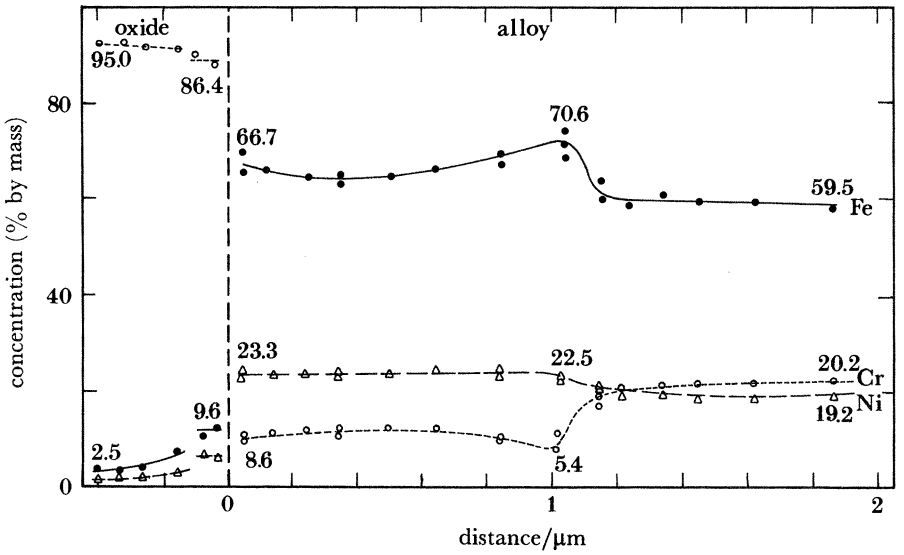

FIGURE 21. Composition profiles for Fe–20Cr–20Ni and the scale formed in 1 % CO–CO_2 after 1000 h at 600 °C. Note that chromium depletion in the alloy occurred only in the *ca.* 1 μm recrystallization zone beneath the scale.

Reconsidering the 1 μm 'recovery' zone seen beneath the scale (see figure 19), it will be remembered that partially recovered but much smaller grain size regions in which there was *no* chromium depletion were seen beneath the scale formed in air. By comparison, the grain size in the zone, as formed in CO–CO_2, is larger and comparable with that identified in the rather thicker region beneath the scale formed on the 34Ni alloy (figure 17). Equally, as can be seen from the composition profiles shown in figure 21, it is only within the recovery zone that there is marked chromium depletion. In a similar manner to the 34Ni alloy, no carbides

are formed either in the oxide or in the recovery zone although they are again precipitated immediately beneath the well defined lower interface of this zone (see figure 20*b*). The morphology of the carbides formed to a depth of some 4–5 μm beneath the 'recovery' interface, is however very different from that in the 34Ni alloy (compare figure 20*c* with figure 17). The carbides were found to be cubic (figure 20*d*) and in epitaxial arrangement with the austenite and we believe that, despite the differences in morphology, the carbides formed in both alloys have the same $M_{23}C_6$ structure.

EDS analysis (figure 21) of the cation distribution in and beneath the scale demonstrated that although the outer part of the scale had a composition of 95% Cr, 2% Fe and 1% Ni, the inner more equiaxed grains described above had a lower chromium and a higher iron and nickel content in a way which was not observed on the 34Ni alloy. While again we see chromium depletion to 8.5% in the alloy at the metal–oxide interface, the lower interface of the recovery zone now has a more distinct chemical nature with still *lower* chromium levels here than at the oxide interface. This indicates competitive diffusion processes for the formation of the oxide and the carbides from the carbon diffusing rapidly and deeply into the alloy.

(iii) Fe–20Cr–2Ni(α)

The mass-gain data for Fe–20Cr–2Ni demonstrated marked changes in its scaling behaviour for the two oxidation environments (see table 3). The data also suggested that there should be distinct differences between the oxides formed on this alloy and on the higher Ni content materials. Regions of essentially 'protective' oxide, formed after 1000 h, were however observed by 'edge-on' transmission electron microscopy and a typical area of this type, where the scale thickness is about 0.5–0.6 μm, is shown in figure 22, plate 14 overlying the ferritic alloy. However, no carbides were found to have been precipitated in the region shown, either in the alloy matrix or in the scale. The morphology of the metal–oxide interface was examined and the cusped shape of the oxide grains suggests some general inward development. In particular, we now see evidence that preferential inward oxidation occurred at alloy grain boundaries as at A in figure 22, a region which is shown enlarged in the inset dark field micrograph. The oxide itself has a grain size of approximately 100 nm, compared with *ca.* 50 nm for both austenitic Fe–20Cr–Ni alloys, but exhibits no specific orientation relation with the underlying alloy (see inset diffraction pattern in figure 22). *Two* oxide phases were however identified in the scale by microdiffraction. These were the α-sesquioxide phase (a $(\bar{1}2\bar{1}6)$ normal is shown in figure 23*a*, plate 15) and a cubic oxide ((223) and (011) FCC normals of this phase are shown in figure 23*b* and *c* respectively). The FCC oxide was found to be randomly distributed through the scale, and not specifically sited at either the metal–oxide or oxide–gas interfaces. No distinction was made between the cubic γ-M_2O_3 and M_3O_4 phases, although the lattice parameter of the cubic oxide (table 5), identified by X-ray diffraction, suggests that the oxide might be M_3O_4. Neither EELS nor convergent beam electron diffraction (CBED) could be used to differentiate between the two possibilities because of the small oxide grain size. Equally the situation is confused by the fact that, in certain areas M_3O_4 is formed in duplex oxide scales.

An EDS analysis of the 'protective' scale and underlying alloy is shown in figure 24. The oxide was found to have a relatively low chromium concentration (less than 40%), compared to that on the austenitic Fe–20Cr–Ni alloys while the alloy beneath the scale was only slightly depleted in chromium. The depth of the chromium depletion layer was however approximately 1.5 μm and thus similar in this context to that on the 20Ni alloy despite the very different processes occurring there.

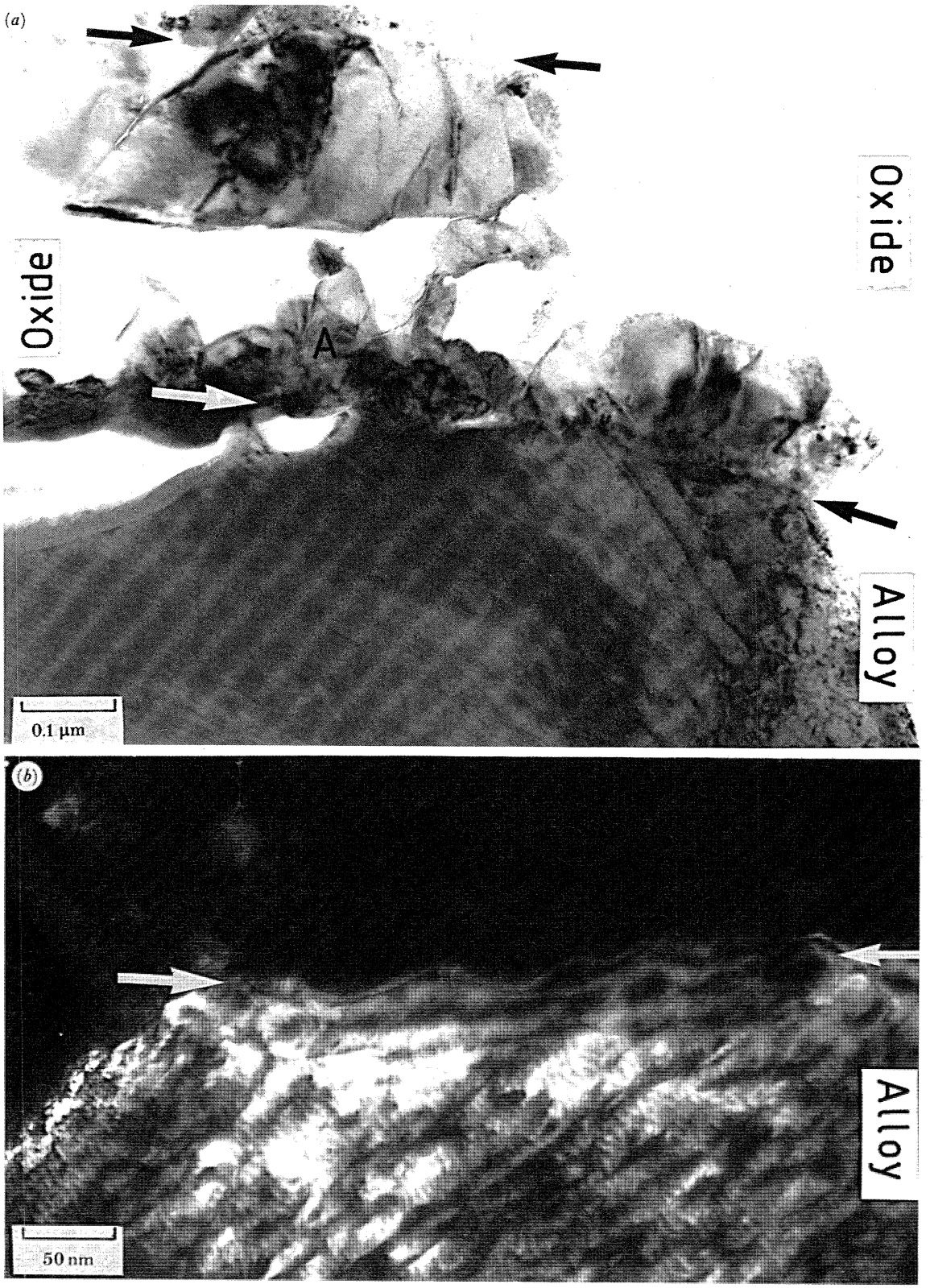

FIGURE 14. Fe–20Cr–2Ni oxidized in air for 1000 h. (*a*) Bright-field micrograph showing the scale and underlying alloy. Note the comparatively 'open' morphology of the scale (see figure 6*a*) and the fine oxide grains at the metal–oxide interface, as at A. (*b*) Dark-field micrograph showing the cusped morphology of the metal–oxide interface (arrowed) which is inclined. The surface of the ferrite has also been partly oxidized during the preparation of the foil, as indicated by the moiré fringes.

(*Facing p.* 206)

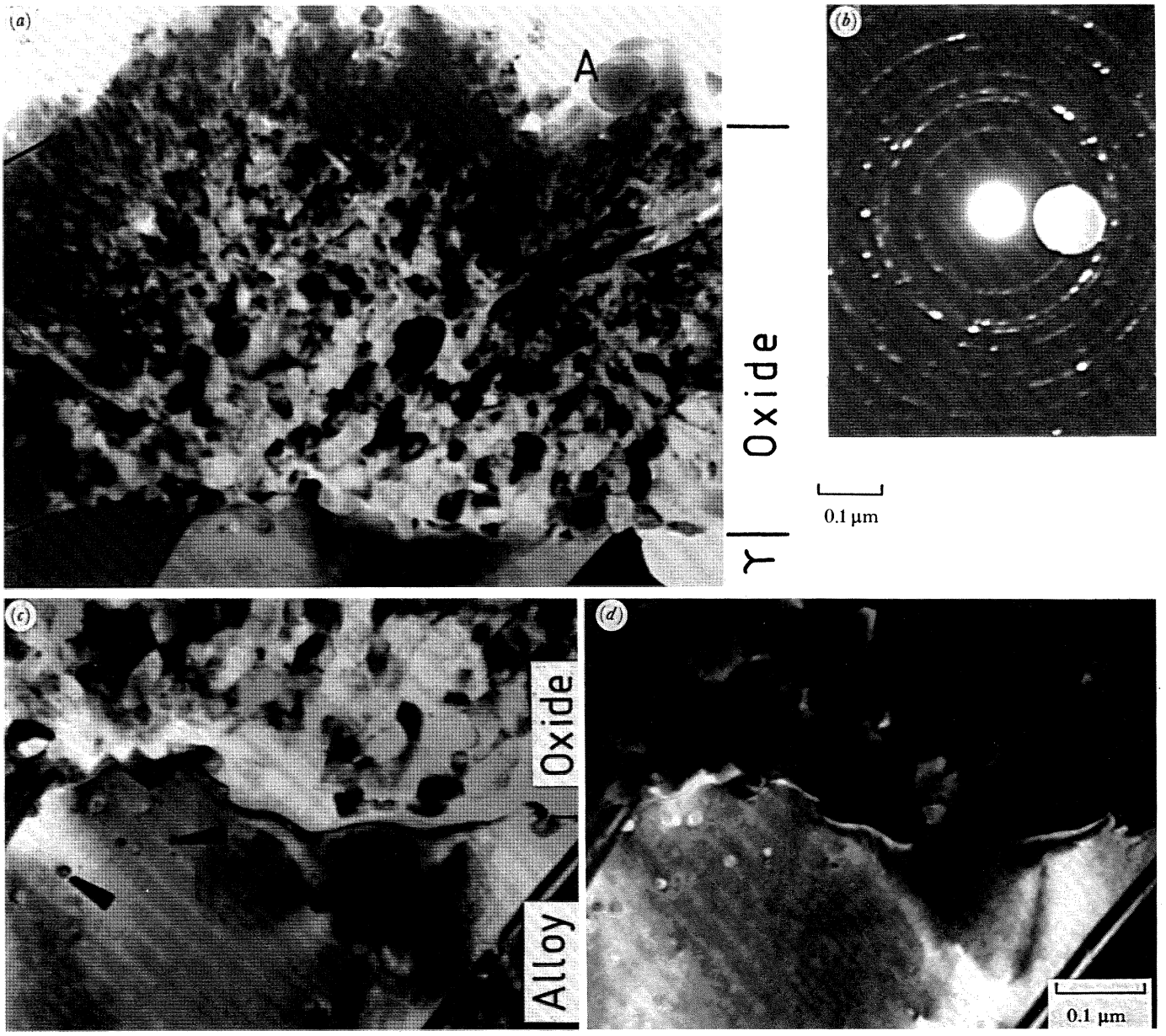

FIGURE 16. Fe–20Cr–34Ni oxidized in 1% CO–CO_2 for 1000 h at 600 °C. 'Edge-on' TEM. (*a*) Bright-field micrograph showing the scale morphology. Note the progressive change in morphology towards the oxide gas interface, which in some regions is sputter contaminated from ion beam thinning, as at A. (*b*) α-M_2O_3 diffraction pattern. (*c*) Bright-field and (*d*) dark-field micrograph (imaged with an austenite reflection) showing the cusped morphology of the metal–oxide interface. The arrowed particles in (*c*) are again sputter contamination.

DESCRIPTION OF PLATE 11

FIGURE 17. Fe–20Cr–34Ni oxidized in 1% CO–CO_2 for 1000 h at 600 °C. 'Edge-on' bright field TEM. $M_{23}C_6$ as precipitated at alloy grain boundaries are arrowed. Contamination of the scale–gas interface where partial separation from the nickel plate has occurred during the ion beam thinning preparation of the foil is apparent.

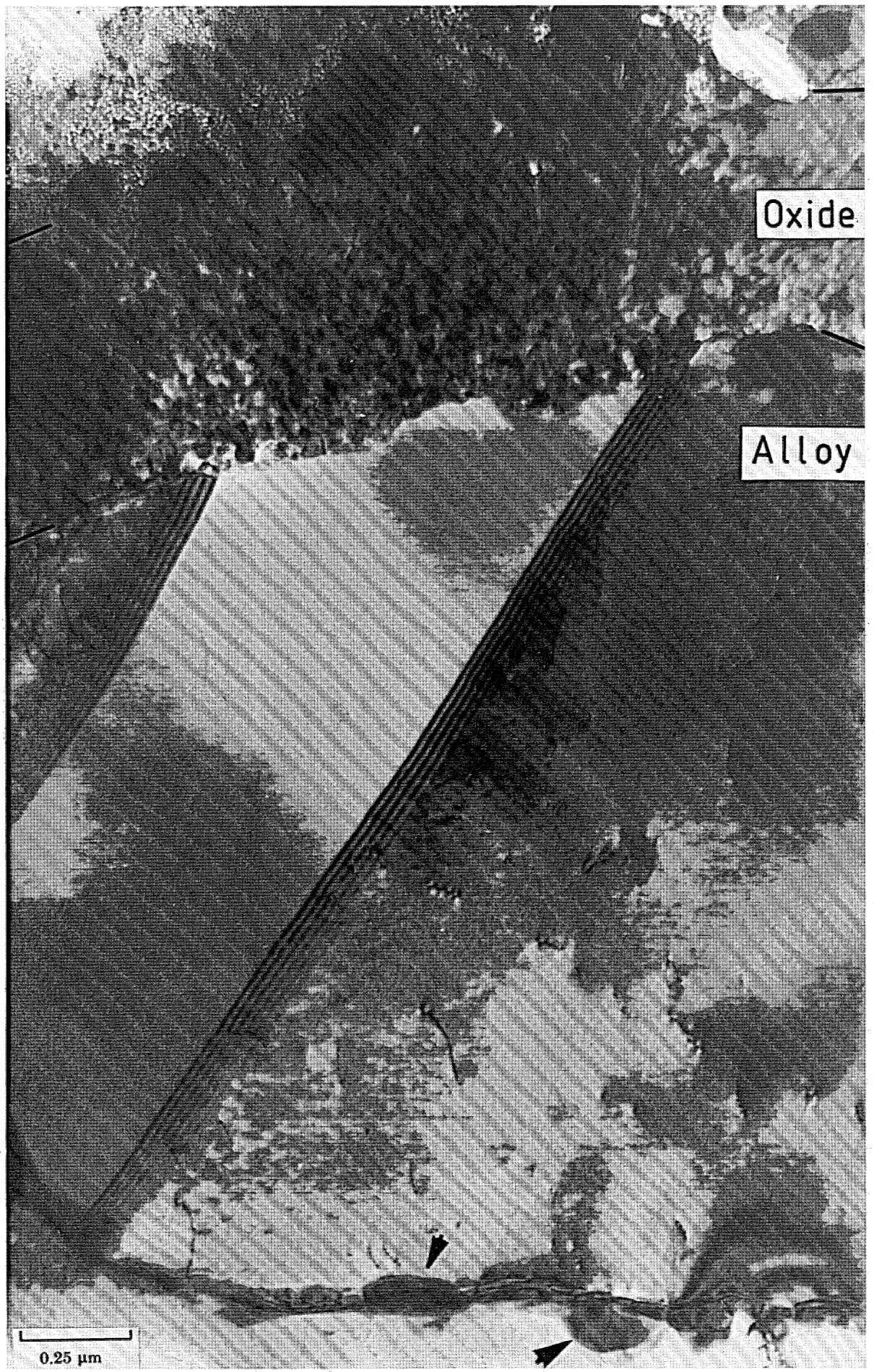

FIGURE 17. For description see opposite.

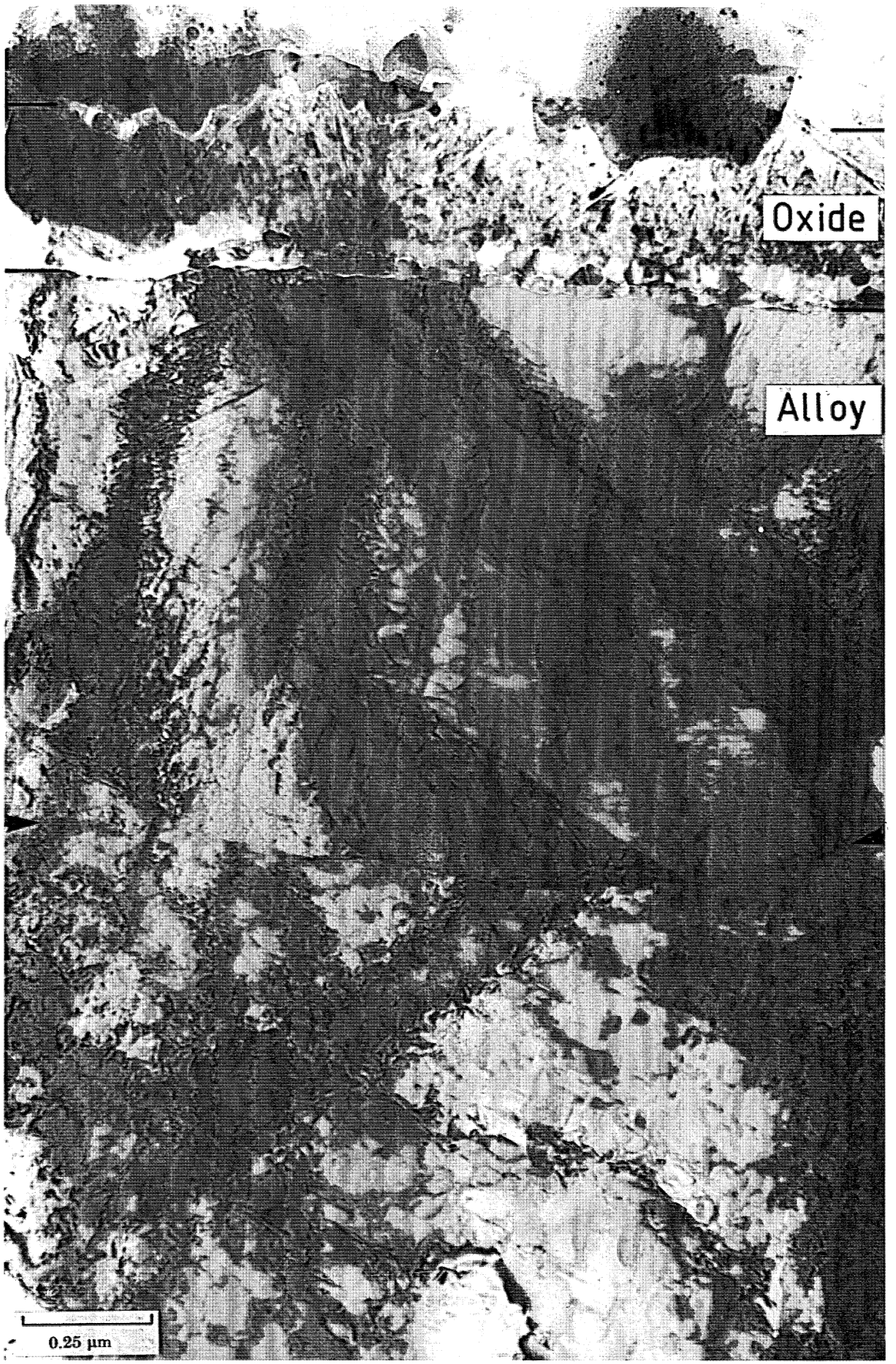

FIGURE 19. For description see plate 15.

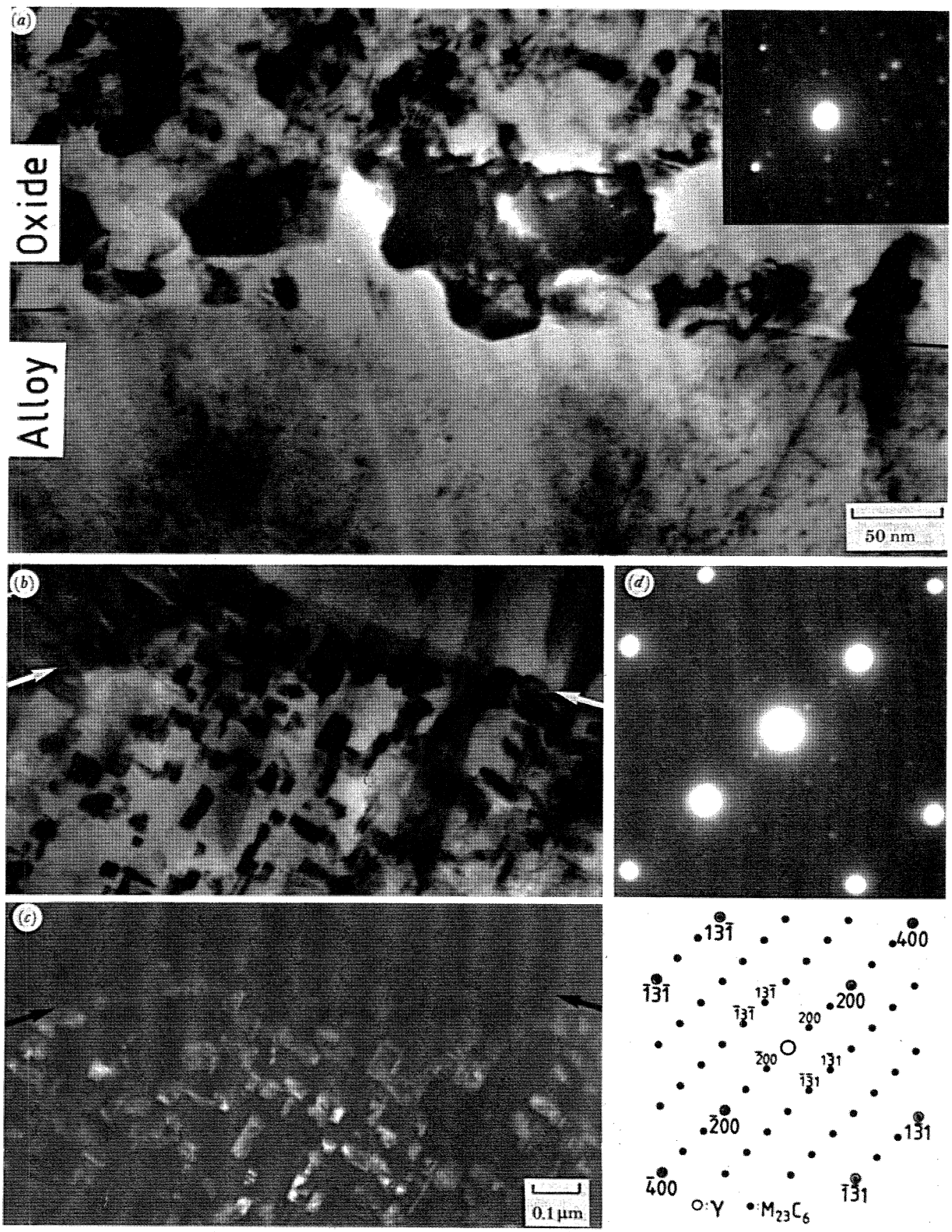

FIGURE 20. Fe–20Cr–20Ni oxidized in 1 % CO–CO_2 for 1000 h at 600 °C. (*a*) Bright-field micrograph of the alloy scale interface showing equiaxed oxide grains which again have a cusped morphology. The inset shows a $(\bar{1}2\bar{1}6)_{Cr_2O_3}$ diffraction pattern. (*b*) Bright-field and (*c*) dark-field micrograph (imaged with a (200) carbide reflection showing $M_{23}C_6$ precipitates in the alloy. The interface between the recrystallized and bulk alloy (see figure 19) is arrowed in (*b*) and (*c*). It is apparent that carbide precipitation has not occurred in the recrystallized region of the alloy. (*d*) $(310)_\gamma//(310)_{M_{23}C_6}$ diffraction pattern.

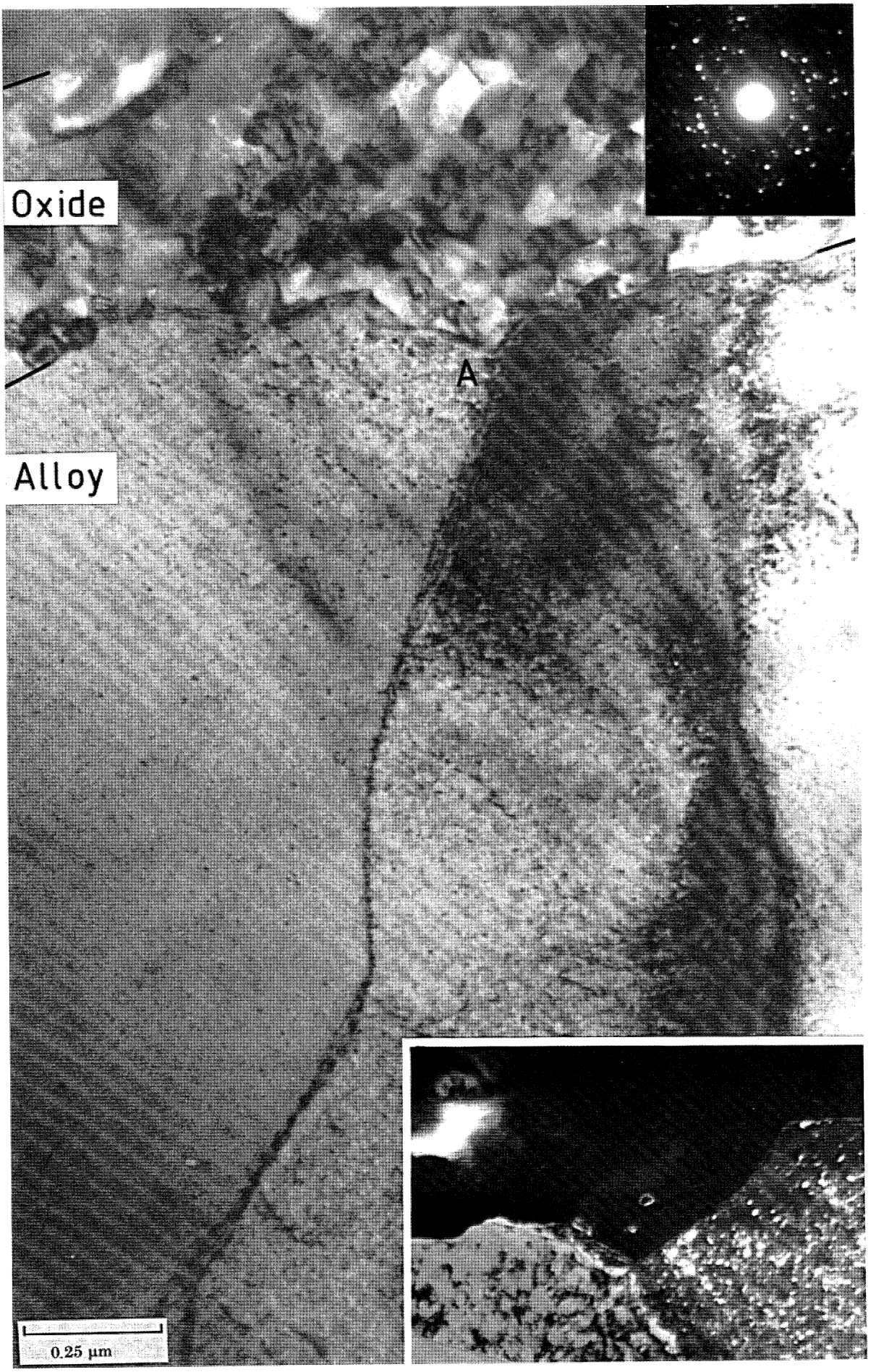

FIGURE 22. For description see plate 15.

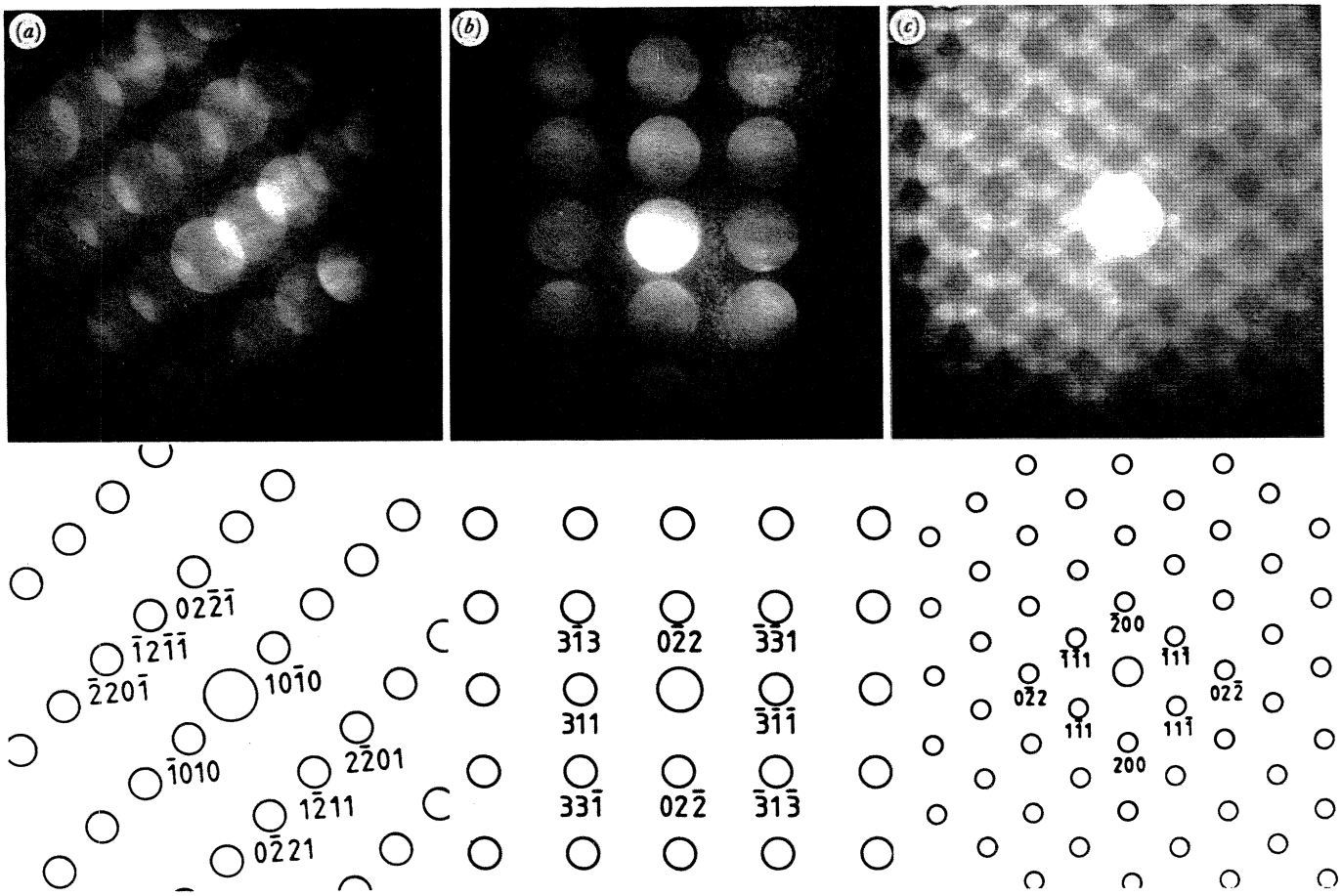

FIGURE 23. Diffraction patterns from the 'protective' scale formed on Fe–20Cr–2Ni in 1 % CO–CO_2 after 1000 h at 600 °C showing α-sesquioxide and cubic oxide phases. (*a*) $(\bar{1}2\bar{1}6)_{M_2O_3}$, (*b*) $(233)_{M_3O_4}$, (*c*) $(011)_{M_3O_4}$.

DESCRIPTION OF PLATE 12

FIGURE 19. Fe–20Cr–20Ni oxidized in 1 % CO–CO_2 for 1000 h at 600 °C. 'Edge-on' bright-field TEM. The interface between the recrystallized austenite, which extends for *ca.* 1 μm beneath the scale, and the bulk of the alloy is arrowed. Note the equiaxed oxide grains at the metal–oxide interface which give the scale a two-layered appearance.

DESCRIPTION OF PLATE 14

FIGURE 22. Fe–20Cr–2Ni oxidized in 1 % CO–CO_2 for 1000 h at 600 °C. 'Edge-on' bright-field TEM. Partial growth of the fine-grained oxide into the metal has occurred at the alloy grain boundary, as at A, a region which is shown enlarged in the inset dark field micrograph (imaged with a ferrite reflection). Carbide precipitation in either the alloy or the scale is not apparent.

DESCRIPTION OF PLATE 16

FIGURE 25. Fe–20Cr–2Ni oxidized for 1000 h in 1 % CO–CO_2 at 600 °C. 'Edge-on' bright-field micrographs showing the microstructure of the 'non-protective' and inward grown scale formed beneath 'hopper' magnetite. (*a*) Fine-grained spinel (see inset diffraction pattern) approximately 5 μm from the duplex oxide interface. (*b*) Approximately 10 μm beneath the duplex oxide interface. M_3O_4 spinel grains encapsulating ferrite, beneath which $M_{23}C_6$ carbides have been precipitated in the alloy. The inset shows a twinned $(011)_{M_3O_4}$ diffraction pattern. (*c*) Coarse $M_{23}C_6$ precipitates in the alloy approximately 5 μm beneath the region shown in (*b*). The inset shows an $(011)_{M_{23}C_6}$ diffraction pattern, which exhibits streaking indicative of internal faulting in the carbides.

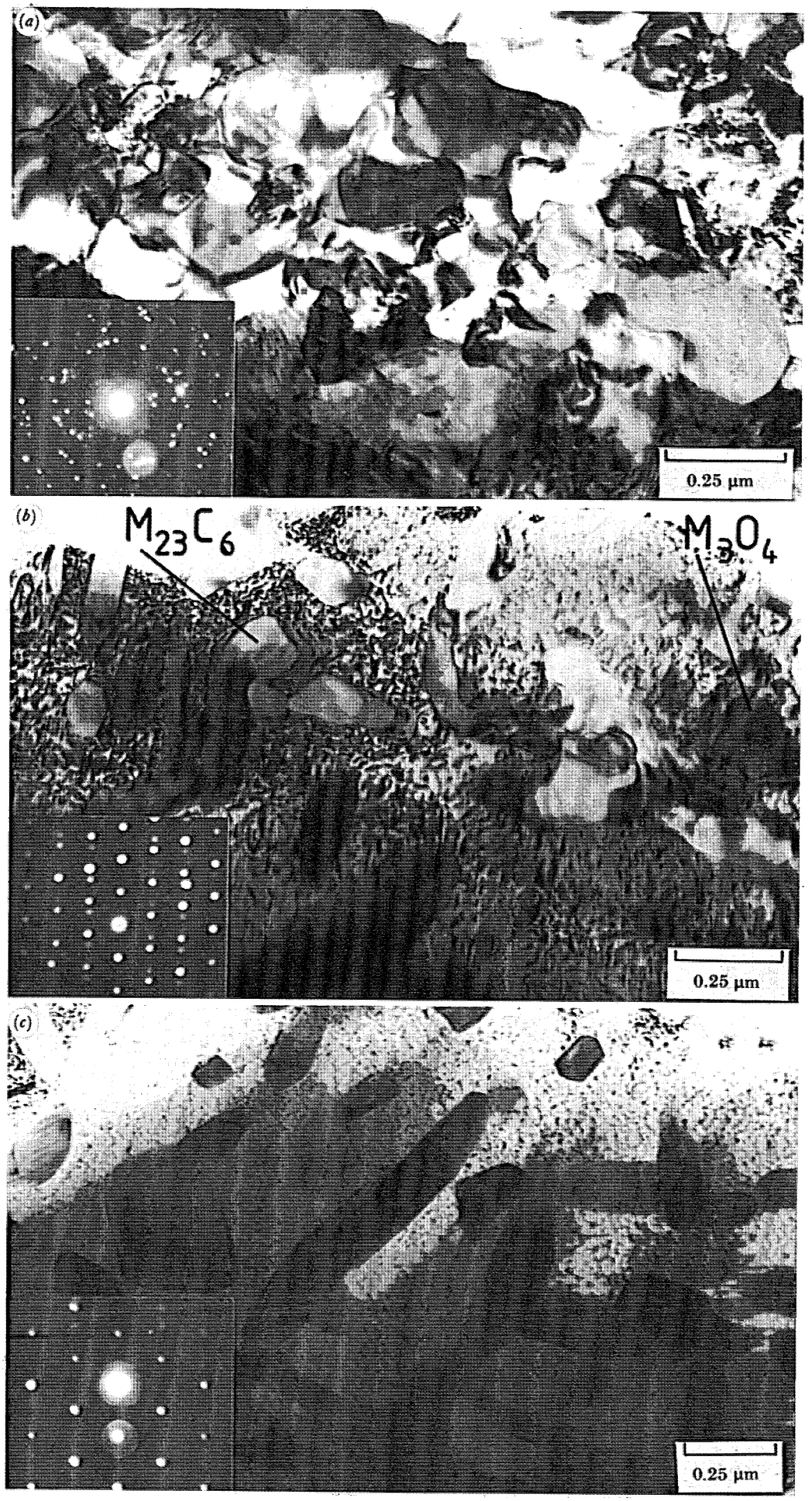

FIGURE 25. For description see plate 15.

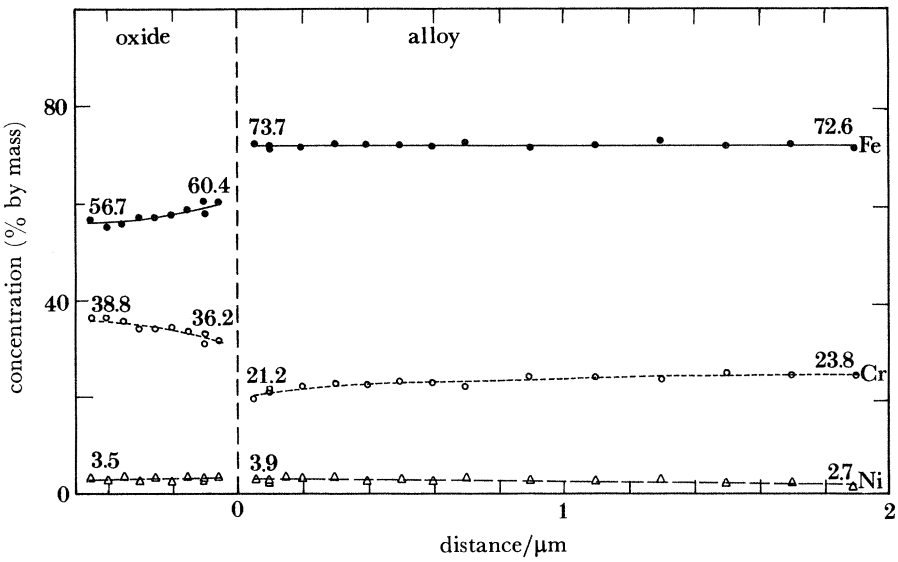

FIGURE 24. Composition profiles for Fe–20Cr–2Ni and the 'protective' scale formed in 1% CO–CO_2 after 1000 h at 600 °C. Note the comparatively high chromium concentration in the scale.

It will be remembered that characteristic nodular oxides with a 'hopper' morphology were observed on this material as oxidized in CO–CO_2 (figure 8*c*). This type of 'non-protective' duplex oxide growth was also observed by 'edge-on' TEM, thus explaining both the high mass gains for this alloy, despite the form of the 'protective' scale described above, and demonstrating that the apparently parabolic kinetics observed are not associated with a single process. The outer layer of the 'hopper' nodules was not retained in the 'edge-on' foil preparation procedure but regions, which were probably originally beneath such nodules, were found where a fine grained oxide was seen to be growing 'non-protectively' into the metal surface. Such a region of a well developed growing scale is shown in figure 25, plate 16. The oxide seen in figure 25*a* was found to be the FCC spinel phase with a grain size *ca.* 250 nm. No carbides or alloy phase were identified in this part of the inward growing oxide. The spinel was found by EDS to exhibit a cation composition of *ca.* 40% Fe, 56% Cr and 2% Ni.

Direct evidence for oxide growth having taken place into the metal is provided by figure 25*b* which shows a region approximately 10 μm from the duplex oxide interface, and *ca.* 1 μm in thickness, where ferrite is encapsulated by the oxide. The form of these M_3O_4 grains, which exhibited no orientation relationship with the ferrite, should be compared with the 'orientated inward' scales formed in the austenitic Fe–10Cr–Ni alloys (see II). While $M_{23}C_6$ precipitates are also seen in this region, as indicated in figure 25*b*, there is again no evidence to suggest that the continuous part of the inward grown scale itself (figure 25*a*) contains carbides, despite the lack of any discrete interfaces between the alloy and scale. The development of a coarse precipitation of *ca.* 0.4 μm $M_{23}C_6$ in the alloy beneath the region shown in figure 25*b* and to a depth of 10 μm is demonstrated in figure 25*c*.

It would appear that while extensive regions of apparently 'protective' scale form on this alloy with only limited indications of a tendency to inward oxide growth, as for example at alloy grain boundaries, chemical instabilities can also allow the formation of a typical '*non-protective*' scale of the type that will be described in detail for other alloys in II.

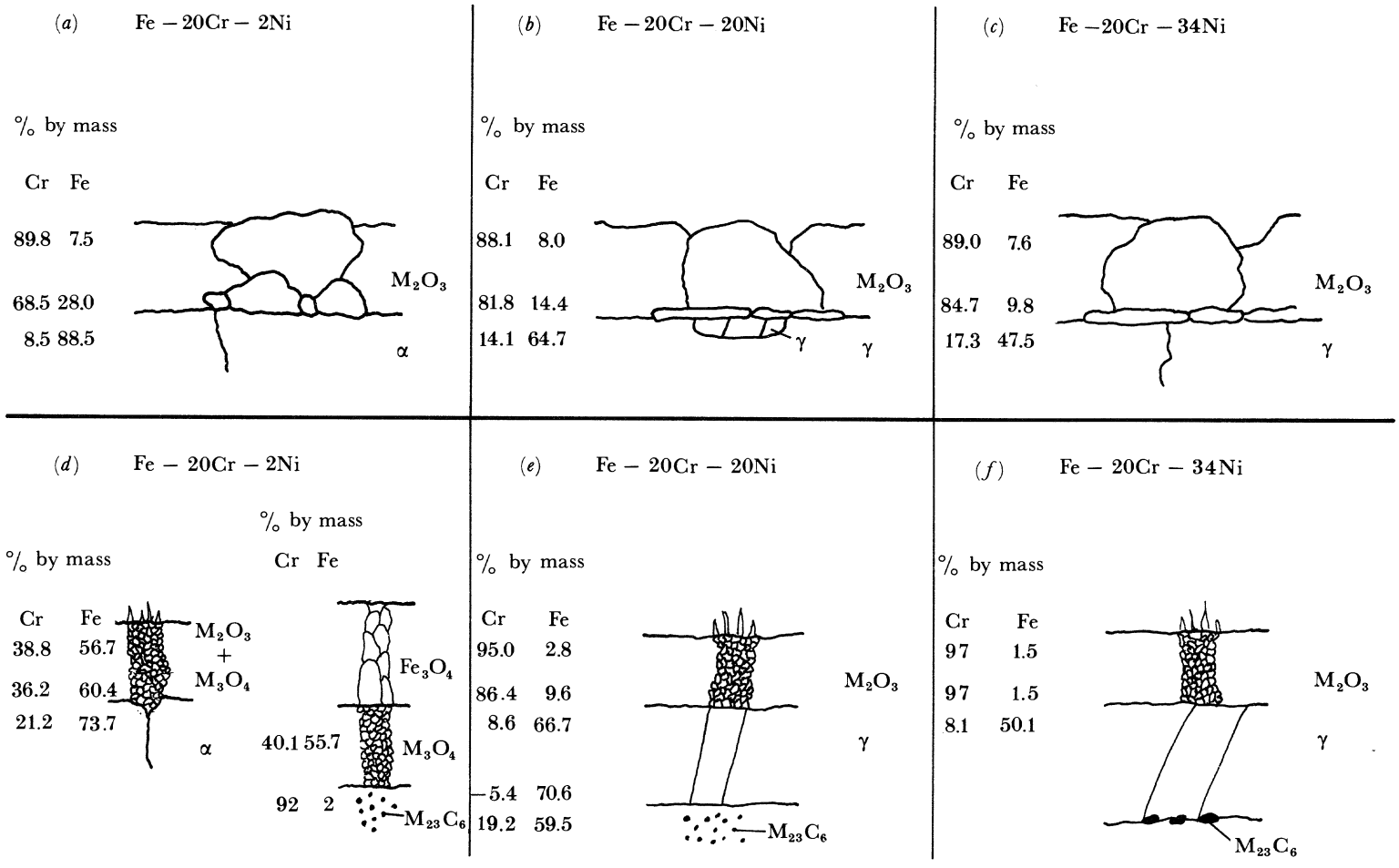

FIGURE 26. Schematic diagrams of the oxides formed on the Fe–20Cr–Ni alloys after oxidation for 1000 h at 600 °C.
(*a*)–(*c*) Scales formed in air, (*d*)–(*f*) scales formed in 1 % CO–CO_2.

4. Experimental results summary

The characteristics of the 'protective' scales formed after 1000 h oxidation in air and in CO–CO_2 are summarized in tables 6 and 7 respectively. The data is also set out schematically as an aid to the visualization of the various trends in figure 26.

Table 6. Summary of the oxidation characteristics of the Fe–20Cr–Ni alloys oxidized in air at 600 °C

(The data refer to the oxides formed after 1000 h.)

alloy	Fe–20Cr–2Ni	Fe–20Cr–20Ni	Fe–20Cr–34Ni
alloy microstructure			
pre-oxidation			
XRD	α	γ	γ
TEM	α	γ	γ
post-oxidation			
XRD	α(+γ)	γ	γ
TEM	α	γ	γ
X-ray diffraction			
lattice parameters/nm			
α-M_2O_3 a_H[a]	0.4971	0.4981	0.4970
c_H[a]	1.3605	1.3606	1.3601
oxidation kinetics			
mass gain/(mg cm^{-2})	0.72	0.83	0.96
n	2.53	2.47	2.32
10^{13} k_p/(g^2 cm^{-4} s^{-1})	1.44	1.91	2.56
10^{16} k_c/(g^3 cm^{-6} s^{-1})	1.04	1.59	2.46
optical metallography			
scale thickness/μm	< 1	< 1	< 1
scanning electron microscopy			
oxide grain size/μm	0.5–1	1–1.5	1.5–2
EDS Cr:Fe	1:1	3:2	3:1
transmission electron microscopy			

	α	Cr_2O_3		γ	Cr_2O_3		γ	Cr_2O_3	
oxide identification									
oxide thickness/μm			0.5			0.4			0.6
oxide grain size/μm			0.6			1.0			1.5
alloy[b]–oxide[c] Fe:Cr:Ni composition (% by mass)									
Fe	88.5	28.0	7.5	64.7	14.4	8.0	47.5	9.8	7.6
Cr	8.5	68.5	89.8	14.1	81.8	88.1	17.3	84.7	89.0
Ni	2.9	2.4	2.3	20.4	2.1	2.2	34.7	2.5	2.4
depth of alloy Cr depletion/μm	1.5			1.5			1.5		

[a] Indexing based on equivalent hexagonal unit cell.

[b] Data refers to the alloy composition 50 nm from the metal–oxide interface.

[c] Both sets of data refer to the composition of the oxide 50 nm from the metal–oxide and oxide–gas interfaces, as indicated.

The broken lines refer to the position of the metal surface before oxidation.

TABLE 7. SUMMARY OF THE OXIDATION CHARACTERISTICS OF THE Fe–20Cr–Ni ALLOYS OXIDIZED IN 1% CO–CO_2 AT 600 °C. THE DATA REFERS TO THE OXIDES FORMED AFTER 1000 h

alloy	Fe–20Cr–2Ni			Fe–20Cr–20Ni			Fe–20Cr–34Ni		
alloy microstructure									
pre-oxidation									
XRD	α			γ			γ		
TEM	α			γ			γ		
post-oxidation									
XRD	α(+γ)			γ			γ		
TEM	α			γ			γ		
X-ray diffraction									
lattice parameters/nm									
M_3O_4 a_0	0.8355			0.8341			—		
α-M_2O_3 a_H[a]	0.4995			0.4965			0.4959		
c_H[a]	1.3620			1.3604			1.3604		
oxidation kinetics									
mass gain/mg cm^{-2}	7.34			1.41			1.08		
n	2.01			1.53			3.20		
$k_n/(g\ cm^{-2})^n\ s^{-1}$	1.4×10^{-11}			1.73×10^{-13}			8.93×10^{-16}		
optical metallography									
scale thickness/μm	< 1			< 1			< 1		
scanning electron microscopy									
surface morphology	whisker (Cr_2O_3)			whisker (Cr_2O_3)			whisker (Cr_2O_3)		
transmission electron microscopy									
oxide identification	α	M_2O_3+M_3O_4	α+ $M_{23}C_6$	M_3O_4	Fe_3O_4	γ+ $M_{23}C_6$	Cr_2O_3		γ+ $M_{23}C_6$	Cr_2O_3	
oxide thickness/μm		0.6		12	ND		0.3			0.6	
oxide grain size/μm		0.1		0.25	ND		0.05			0.5	
alloy[b]–oxide[c] Fe:Cr:Ni composition (% by mass)											
Fe	73.7	60.4	56.7	92	55	ND	66.5	9.6	2.8	50.1	1.5	1.5
Cr	21.2	36.2	38.8	2	40	ND	8.5	86.4	95.0	8.1	97	97
Ni	3.9	3.4	3.5	5	3.5	ND	23.3	2.5	1.0	39.6	0.5	0.5
depths of alloy Cr depletion	1.5		< 10			≈ 1.0			≈ 4.5		

[a] Indexing based on equivalent hexagonal unit cell.
[b] Data refers to the alloy composition 50 nm from the metal–oxide interface.
[c] Two sets of data refer to the oxide composition 50 nm from the metal–oxide and oxide–gas interfaces, as indicated.
The broken lines refer to the position of the metal surface before oxidation, the double lines separate different behaviours.
ND, no determination.

5. DISCUSSION

In the following discussion the various trends observed in the 'protective' oxidation behaviour, as morphologically and chemically characterized for the different alloys, are considered first for oxidation in air (§5*a*) and then for the low partial pressure 1% CO–CO_2 atmosphere (§5*b*).

(*a*) *Oxidation in air*

Since α-Cr_2O_3 is the only oxide formed in the dry oxidation of chromium (Mortimer & Post 1968), the oxidation behaviour of pure chromium can be usefully compared with that of the Fe–20Cr–Ni alloys. Caplan & Cohen (1965) for example, oxidized chromium and Fe–26Cr

at 870–1200 °C and discussed the comparable oxidation characteristics of the two systems on the basis of their similar BCC lattice parameters. Comparison of the oxidation rate constants, taken to be parabolic, for the Fe–20Cr–Ni alloys (table 3), with the parabolic rate constant derived for the oxidation of chromium (Hagel 1965) and of Fe–50Cr (Mortimer & Post 1968) demonstrates that the 20Cr–Ni alloys follow similar trends, the increase in rate constant with nickel content thus being arguably simply associated with a parallel decrease in the Fe activity relative to that of chromium at the alloy–oxide interface. It would also appear that the structure of the alloy has little effect on this type of oxidation behaviour. The argument is further supported by the way the iron concentrations in the scales progressively increase, and have a bigger gradient with depth in the scale, as the nickel content is decreased in the series. So, although the depletion layer beneath the scale was of similar depth for each alloy, the decrease in chromium concentration immediately beneath the scale was greater the lower the nickel content (being 4, 6 and 12 % for the 34, 20 and 2Ni alloys respectively). Thus we see a paralleled increase in rate constant with decreased chromium gradients in the alloy and higher chromium concentrations at the metal–oxide interface. In this way the potential supply of chromium at the alloy–oxide interface, as determined by its concentration and diffusivity near the alloy surface, may critically determine the oxidation kinetics and the microstructure of the oxides formed on these alloys. Certainly, the composition of the first formed oxide will be critically affected by the chromium activity at the metal–oxide interface. Symptomatic of how the composition and structure of oxide nuclei and mature scales may differ was the fact that *in situ* TEM of the Fe–20Cr–Ni alloys indicated that it is the spinel-type oxide which is nucleated at room temperature rather than a chromium-rich sesquioxide. M_3O_4 was observed on both the austenitic Fe–20Cr–20Ni alloy and on the ferritic Fe–20Cr–2Ni alloy when 'edge-on' foils were prepared at low oxygen partial pressures by ion beam thinning. Evidence from AES (Hultquist & Leygraf 1982) and LEED studies (Leygraf & Hultquist 1975) similarly shows that an iron-rich spinel-type oxide is preferentially formed on Fe–20Cr alloys at 525 °C, at least at low oxygen partial pressures (10^{-9} to 10^{-7} Torr).† Such observations suggests that at 600 °C the oxidation reaction initially involves the formation of non-equilibrium nuclei of the oxides of each alloy constituent. However, the stability of an oxide phase is dependent upon several factors other than its free energy of formation (see table 8) including the activity of chromium in the alloy beneath the scale, and the oxygen activity. The equilibrium constant for the oxidation of chromium:

$$2Cr + \tfrac{3}{2}O_2 \rightarrow Cr_2O_3$$

may be written as:

$$K = [Cr_2O_3]/[Cr]^2\,[O_2]^{\frac{3}{2}}$$

in which case the change in free energy for the reaction is given by

$$\Delta G^{\circ} = -RT\ln[K] \quad \text{and} \quad [Cr] = (K[O_2]^{\frac{3}{2}})^{-\frac{1}{2}}.$$

The oxygen activity is determined by the dissociation pressure of the spinel oxide, present at the start of oxidation. Thus at 600 °C the activity of oxygen at the alloy–oxide interface is approximately 10^{-27} atm‡ (Lloyd *et al.* 1977), while K, calculated from free energy data (Kubaschewski & Evans 1958) is approximately 10^{53} so that, on this basis, a chromium activity greater than only 10^{-6} should lead to the formation of Cr_2O_3 (Lloyd *et al.* 1977).

† 1 Torr = (101 325/760) Pa [≈ 133.322 368 Pa].
‡ 1 atm = 101 325 Pa.

After 6 h oxidation at 600 °C Fe–20Cr–34Ni was shown to have formed a 50–100 nm thick layer of chromium oxide (figure 9) confirming at least that selective, if not exclusive, oxidation of chromium occurs after only a relatively short incubation period, although whether or not the spinel is first formed at 600 °C is unknown. Equally all the data obtained, both from the chemical analysis of 'edge-on' foils and from the temporal development of the M_2O_3 lattice parameters (table 4), point to a progressive enrichment in chromium of the scales being formed at the outer oxide–gas interface. However, they way in which the general development of the scales, as studied here by 'edge-on' TEM, has taken place would not appear to be consistent with some conventional models for the growth of chromium rich scales. For example, the growth of 'protective' chromium oxide scales on an Fe–27.3Cr–39.3Ni alloy at 1000 and 1200 °C has been studied by Hobby & Wood (1969) who identified Cr_2O_3 scales containing nickel and iron. The maximum concentration of iron and nickel was observed at the outer edge of the scale (as in the oxidation of Ni–Cr alloys (Wood *et al.* 1966)) using conventional electron-probe microanalysis. On this basis, Hobby & Wood (1969) proposed that the rapidly growing iron and nickel doped oxides overgrow the chromium containing nuclei. However, the compositional profiles of the 'protective' oxides formed at 600 °C may be taken, at least to first order, to show the compositional history of the scale formation. Any detailed non-historically recorded effects can of course be checked by examining 'edge-on' foils produced after different oxidation periods (for example §3*f*). It is thus significant that the EDS analyses indicated that the iron concentration at the base of the scales was always higher than nearer to the oxide–gas interface, and that the scale formed here was fine grained, giving the appearance of being two layered. Furthermore, the thickness of the inner fine grained layer of oxide was shown to change, but only minimally with time. For example, the 20Cr–34Ni alloy was examined 'edge-on' after 6 and 1000 h over which period the thickness of fine grained layers at the metal–oxide interface increased from 20 to 20–50 nm. This both confirms the minimal development of any inward oxidation and suggests that the chromium oxide has preferentially grown to cover the iron-rich first-formed oxide by the outward migration of cations in a similar manner to that described by Wagner (1956). The microstructure of the fine-grained oxide identified at the alloy–oxide interface is, however, characteristically different from the 'orientated inward' oxide found in the Fe–Ni–Cr alloys of lower chromium content (see II). It would thus appear that the high resolution compositional data obtained here by EDS is not consistent with Hobby & Wood's (1969) description of the oxidation mechanism for Fe–27.3Cr–39.3Ni.

If we consider the kinetics of the oxidation observed in air (figure 4*a* and table 3) we see that the rate law communally observed is intermediate between $n = 2$ and $n = 3$. While a parabolic law is usually taken to imply a process controlled by the outward diffusion of Cr^{3+} ions the observed behaviour might be reasonably explained on the basis of the additional effect of a progressive reduction with time of the chromium activity relative to that of iron at the base of the scale. There is in fact some evidence that such a reduction occurs. For example, we have shown that limited but characteristic inward growth of the fine-grained oxide takes place at increased chromium activity relative to that of the outer scale. It should, however, be noted both that little oxide development occurred at alloy grain boundaries and that easier oxide creep might be expected the greater the non-stoichiometry of the oxide (Kofstad 1981), this facilitating the continued contact of the oxide with the retreating metal surface. Essentially we must emphasize that, under the conditions discussed here, even with limited growth of the oxide into the alloy, the principal process is 'protective' with outward growth.

(*b*) *Oxidation in* 1% CO–CO_2

A number of workers (see, for example, Francis & Whitlow 1965; Francis 1968) have studied the high-temperature (> 750 °C) growth of two-layer oxides on steels, containing more than 16% Cr in carbon dioxide. Under these conditions, the scale has been found to consist of an inner layer of Cr_2O_3 bounded by an outer layer of iron–chromium spinel. Microprobe and SEM techniques have been used to infer that chromium oxide was the first formed oxide and that spinel subsequently grew by the cationic diffusion of metal ions through this protective layer. This mechanism has also been proposed for the oxidation of an unstabilized austenitic stainless steel (En58A) at low oxygen partial pressures (Wild 1977) and is consistent with the thermodynamic arguments of Hales & Smith (1974) that chromium oxide is the stable oxide formed on this type of Fe–Ni–Cr alloy. Turner (1980) however, took into account the presence of iron oxides formed during the early stages of the oxidation reaction and showed that an iron–chromium spinel should then be the thermodynamically preferred oxide. On this basis, Tempest & Wild (1981) studied the initial stages of the oxidation of a 20Cr–25Ni–Nb steel by AES and X-ray diffraction and found that chromium oxide was formed only after approximately 1.5 h. An iron rich oxide was observed in the initial stages of the reaction.

The 'edge-on' TEM examination of the 'protective' scales formed on both austenitic 20Cr alloys, as reported here, has provided no evidence for the formation of a two-layer scale, with inner chromium oxide and outer spinel, as observed on some other high chromium alloys (Garrett *et al.* 1982) after long periods of exposure. The M_2O_3 formed on both the 20 and 34Ni alloys had a high chromium content and in neither case was an outer spinel found either in the 'edge on' samples or in samples of oxide scraped from the outer surface of the scale (Newcomb *et al.* 1983). Equally, no evidence was obtained to suggest the formation of a distinct oxide subscale in the chromium depleted regions of these two alloys. Should subscaling have occurred it would be expected to be of the form identified on the austenitic Fe–10Cr–Ni alloys (see II).

Despite minimal depletion of chromium in the zone beneath the oxide formed on Fe–20Cr–2Ni, it was this alloy which showed evidence of inward growth at alloy grain boundaries, even where the scale was generally 'protective'. This 'protective' oxide was found to contain both rhombohedral and cubic phases of high iron composition (56% Fe, 36% Cr and 4% Ni). However, no carbides were observed in Fe–20Cr–Ni beneath the 'protective scale', despite the fact that this alloy is ferritic, presumably because the solubility of carbon in the ferrite is too low to allow a significant concentration gradient into the alloy. While Jepson *et al.* (1965) reported that iron does not react with carbon monoxide to form a metal oxide and carbon, the free energy change accompanying this reaction (shown in table 8) has a negative value for the temperature at which oxidation was carried out in this study. The absolute value of ΔG, however, is considerably lower than that for the corresponding reaction of chromium with carbon monoxide (see table 8). Thus while we have shown that heavy carburization occurs in this alloy locally where 'non-protective' scaling is occurring it remains surprising that carburization does not occur more generally. Further discussion of the essentially competitive nature of inward oxidation and carburization will be found in II.

The morphology of the 'protective' scale, as examined by TEM, does not appear significantly different from that of the 'protective' oxides formed on the alloys of higher nickel content. The relatively high concentration of iron (*ca.* 56%) in the 'protective' scale formed on Fe–20Cr–2Ni

TABLE 8. STANDARD FREE ENERGIES OF REACTION $\Delta G_T = A + CT$

reaction	ΔG/cal† A	C	temperature (T) range/K	reference
$2Cr + \frac{3}{2}O_2 = Cr_2O_3$	−267750	−62.1	298–1200	Richardson & Jeffes (1948)
$2Fe + O_2 = 2FeO$	−124100	29.9	298–1642	
$\frac{3}{2}Fe + O_2 = \frac{1}{2}Fe_3O_4$	−130387	37.3		
$\frac{4}{3}Fe + O_2 = \frac{2}{3}Fe_2O_3$	−129149	40.62		
$6FeO + O_2 = 2Fe_3O_4$	−149250	59.80	298–1642	
$4Fe_3O_4 + O_2 = 6Fe_2O_3$	−119250	67.25	298–1460	
$2Fe + O_2 + Cr_2O_3 = FeCr_3O_4$	−131600	24.2	1173–1700	Richardson *et al.* (1950)
$Ni + \frac{1}{2}O_2 = NiO$	−58450	23.55	298–1725	Richardson & Jeffes (1948)
$C + \frac{1}{2}O_2 = CO$	−26700	20.95	298–2500	
$C + O_2 = CO_2$	−94200	0.2	298–2000	
$2CO + O_2 = 2CO_2$	−135000	41.5		
$C + CO_2 = 2CO$	40800	−41.7		
$23Cr + 6C = Cr_{23}C_6$	−98280	−9.24	298–1673	Richardson (1953)
$7Cr + 3C = Cr_7C_3$	−41700	−6.10	298–1673	
$3Cr + 2C = Cr_3C_2$	−20150	−2.78	298–1673	
$2Cr + 3CO_2 = Cr_2O_3 + 3CO$	−65250	0.15		
$2Cr + 3CO = Cr_2O_3 + 3C$	−187650	0.75		
$4Cr + 3CO_2 = 2Cr_2O_3 + 3C$	−252900	−123.61		
$3Fe + C = Fe_3C$	6200	5.53	298–463	Richardson (1953)
$3Fe + C = Fe_3C$	6380	5.92	463–1115	
$3Fe + 4CO_2 = Fe_3O_4 + 4CO$	9226	−8.45		
$3Fe + 4CO = Fe_3O_4 + 4C$	−153974	158.4		
$Fe_3O_4 + 2CO_2 + CO = {}_3FeCO_3$	−52800	11.22	298–700	Richardson & Jeffes (1948)
$3Fe + 2CO_2 = Fe_3O_4 + 2C$	−72374	74.2		
$Ni + CO_2 = NiO + CO$	9050	−44.3		

† 1 cal = 4.168 J.

may however be a result of the fact that the rate of oxidation of iron has been found to be independent of pressure, at oxygen partial pressures below 10^{-24} atm at 600 °C (Dieckmann & Schmalzried 1977). At the low oxygen partial pressure the dominant diffusion mechanism could change from a vacancy mechanism to one controlled by the diffusion of interstitial ions, thereby encouraging the oxidation of iron and the formation of M_3O_4. Given the initial formation of oxide nuclei of both iron and chromium, the subsequent development of M_3O_4 would then be more favoured in an alloy of high iron content, such as Fe–20Cr–2Ni, than in Fe–20Cr–20Ni or Fe–20Cr–34Ni. Equally, differences in the mobilities of Cr^{3+}, Fe^{3+} and Fe^{2+} in the phases M_3O_4, γ-M_2O_3 and α-M_2O_3 enable oxide transformations during the course of the oxidation reaction (Azaroff 1961). For example, low chromium concentrations in the scale, as observed for the 20Cr–2Ni alloy, would favour the transition of the unstable γ-M_2O_3 phase to M_3O_4. Equally, Fe^{3+} has been shown to have a higher diffusivity than Cr^{3+} in M_3O_4 (Cox *et al.* 1974) so that the outward diffusion of iron could then be perpetuated. One thus has a picture of a chemically unstable switch in oxidation process towards a greater tendency for the oxidation of iron relative to chromium initiated by the independence of the oxidation rate of iron on the oxygen potential at very low partial pressures.

It is thus equally interesting that we have identified the *parallel* development of both 'non-protective' (with inward diffusing anions) and 'protective' scaling on this alloy. Wood & Whittle (1967) have suggested that the transition from the growth of a thin layer of chromium-rich oxide to the growth of a stratified scale is stress induced and is associated with oxide cracking. This is a reasonable mechanism for 'breakaway'. However, whereas our results

suggest that the above mechanism, by which outward Fe^{3+} diffusion is promoted over that of Cr^{3+}, can lead to the formation of a well developed outward growing scale we will see in II that the more iron rich scales also allow more ready ingress of anions to give a parallel development of either a fully 'non-protective' scale or subscale carburization.

We now consider the formation of carbides in the two austenitic alloys. The standard free energies of reaction for the formation of iron, chromium and nickel oxides in oxygen and in carbon dioxide are shown in table 8. Two reactions must be considered when the Fe–20Cr–Ni alloys are exposed to a carbon dioxide based atmosphere, i.e.

$$M + CO_2 \rightarrow MO + CO, \tag{1}$$

$$2M + CO_2 \rightarrow 2MO + [C], \tag{2}$$

where M represents a metallic element, [C] elementary or combined carbon and MO the metal oxide formed on the alloys. The oxide observed on the austenitic Fe–20Cr–Ni alloys was identified as α-Cr_2O_3, so that equations (1) and (2) are represented by:

$$2Cr + 3CO_2 \rightarrow Cr_2O_3 + 3CO; \quad \Delta G^\circ = -65250 + 0.15T, \tag{3}$$

$$2Cr + \tfrac{3}{2}CO_2 \rightarrow Cr_2O_3 + \tfrac{3}{2}C; \quad \Delta G^\circ = -126450 - 61.8T. \tag{4}$$

The deposition of carbon is therefore determined by the relative contribution of (4) to the overall mass gain. However, some account must be made of the oxidation reaction:

$$M + CO \rightarrow MO + [C] \tag{5}$$

as well as the catalysed Bouduard reaction:

$$2CO \rightarrow C + CO_2. \tag{6}$$

Previous studies of the oxidation of austenitic alloys in CO_2 and CO–CO_2 atmospheres have shown that carburization of the metal often does take place. Jepson *et al.* (1965), for example, used ^{14}C sensitive techniques to establish that carbon was transferred from pure carbon dioxide to a 20–25Nb steel at 650–850 °C. The carbon deposition was found to be *ca.* 1 % of the total weight gain of the specimens. The results showed that most of the carbon deposition occurred within the first few hours of oxidation and then ceased although no data for the behaviour after 300 h exposure was obtained. Jepson *et al.* (1965) found that the majority of the mass gain was a result of (1) and that (2) contributed only 7 % of the total mass gain in the 300 h tests. The deposition of carbon was therefore attributed to reaction (5). This reaction occurs before the carbon monoxide is desorbed from the oxidation site and may be assumed to be effectively the only source of carbon in the oxidation of the austenitic alloys forming 'protective' Cr_2O_3 scales. The catalysed Bouduard reaction could provide carbon, but chromium oxide has been found not to catalyse the reaction (Jepson *et al.* 1965) while chromium itself has no significant catalytic activity (Kehrer & Leidheiser 1954). On this basis the Bouduard reaction may be assumed not to occur during the 'protective' oxidation of the austenitic Fe–20Cr–Ni alloys with outward scale development of oxides of very low iron content. It is possible however that it is the increased Fe content of the inward growing 'non-protective' M_3O_4 on the ferritic Fe–20Cr–2Ni alloy which in this case promotes the Bouduard reaction and thus subscale carbide formation.

The subsequent diffusion of carbon through the 'protective' scales after oxidation by (5) may be facilitated by the fine-grained microstructure of the chromium oxide. Moreover, the

retention of carbon monoxide in the reaction zone (for sufficient time for transfer of carbon to occur) would also be favoured by a porous scale. That porosity naturally arises in the formation of Cr_2O_3 needles at the oxide–gas interface has been previously demonstrated by high resolution TEM (Newcomb *et al.* 1983). The voids seen amongst the irregularly growing crystallites were about 40 nm in size and would favour the retention of carbon monoxide rather than its desorption into the gas phase.

Comparing now the kinetic behaviour observed in $CO–CO_2$ with that seen in air, we may note that for Fe–20Cr–34Ni the rate law changes from $n = 2.32$ in air to $n = 3.20$ in $CO–CO_2$. This supports the argument presented in §5*a* that a temporal reduction in chromium activity at the base of a scale will increase n: in $CO–CO_2$ the process is accentuated by carbide formation. It is thus at first sight surprising that for Fe–20Cr–20Ni, where there is also carbide formation and a similarly accentuated chromium depletion layer beneath the Cr_2O_3 scale when oxidizing in $CO–CO_2$, n is decreased. However the probable reason for this may be understood by comparison with the parallel changes in behaviour of the Fe–20Cr–2Ni alloy on which we have seen the characteristic but localized development of 'non-protective' duplex scaling. Comparison of the SEM images of the upper surfaces of the $CO–CO_2$ formed scales on all the alloys demonstrates that hopper oxides are commonly found on Fe–20Cr–20Ni as well as on Fe–20Cr–2Ni. Thus while the mass gains of 20Cr–20Ni are similar to those of 20Cr–34Ni, this masks the fact that more than one type of oxidation behaviour is occurring on this alloy (as it is on Fe–20Cr–2Ni), thus allowing n to take a lower value (2.53) than would have been exhibited given exclusively 'protective' oxidation (see table 3, and note that $n = 3.20$ for the 20Cr–34Ni alloy).

6. Conclusions

We have seen that both in air and in $CO–CO_2$ there are clear trends in the 'protective' oxidation behaviour of the range of Fe–20Cr alloys of differing nickel contents. Equally these trends generally point to this type of oxidation being kinetically controlled, with essentially 'instability switching'. We have argued, for example, that while all three alloys show a common tendency towards cube law kinetics in air with increased oxidation rates at highest nickel content, this is actually paralleled by the chromium activity at the base of the scale being higher when the oxidation is proceeding most rapidly. It is essentially the phenomenological approach which we have taken to the characterization of the scale morphology which allows us to note changes in the general trends and then to see the parallels of these trends with mass gain data. In $CO–CO_2$, relative to air, for example, we find an initially surprising reverse relative behaviour of the weight gain data as a function of nickel content. But this is, we can now see, paralleled by an increasing tendency for inward growth culminating, as the nickel content is lowered to that of the 20Cr–2Ni alloy, in chemically unstable behaviour. Interestingly it would appear that the reasons for the increased mass gain behaviour of the 20 and 2Ni relative to that of the 34Ni alloy are actually rather different. If we take it that in $CO–CO_2$, iron oxidation can proceed more readily than at higher oxygen partial pressures (Dieckmann & Schmalzried 1977) provided that the chromium activity falls below some initial level, then in the 20Ni alloy the chromium activity is progressively lowered (apparently to below this level) by the competitive demands of carbide formation. By contrast it would appear that in the 2Ni alloy the relative Fe activity must be sufficiently high to allow some inward oxidation with higher

relative iron content even without such a reduction in the local chromium concentration. In this alloy once true chemical instability is reached, with carbide formation into the alloy, as under nodules, then the oxidation of iron proceeds much more rapidly with the kinetics, even if apparently simply parabolic, undoubtedly masking many competitively different processes.

We are not thus able to point to a unique phenomenon which might control either the kinetics or any tendency to instability and thus a change over from 'protective' to 'non-protective' behaviour. Even in a simple range of ternary alloys there are apparently several factors which can promote such instabilities. We have however demonstrated how both the use of the 'edge-on' TEM technique and the classification approach we have adopted can provide an extremely useful insight into the ways the oxidation kinetics, and thus the morphology of the scales are controlled. A more detailed discussion of the different forms of the kinetics observed in both this paper and in II is in preparation.

We are grateful to Professor R. W. K. Honeycombe, F.R.S., for the provision of laboratory facilities and to the SERC and the CEGB for partial financial support. This paper is published by the permission of the Central Electricity Generating Board.

References

Azaroff, L. V. 1961 *J. appl. Phys.* **32**, 1638–1662.
Caplan, D. & Cohen, M. 1959 *Corrosion* **15**, 141–146.
Caplan, D. & Cohen, M. 1965 *J. electrochem. Soc.* **112**, 471–477.
Castle, J. 1977 *Surf. Sci.* **68**, 583–602.
Cook, A. J. & Brown, B. R. 1952 *J. Iron Steel Inst.* **171**, 345–353.
Cox, M. G. C., McEnaney, B. & Scott, V. D. 1974 *Phil. Mag.* **29**, 585–600.
Dieckmann, R. & Schmalzried, S. 1977 *Ber. BunsenGes. phys. Chem.* **81**, 414–419.
Francis, J. M. & Whitlow, W. H. 1965 *J. Iron Steel Inst.* **203**, 468–479.
Francis, J. M. 1968 *Br. Corros. J.* **3**, 113–119.
Garrett, J. C. P., Crook, J. T., Lister, S. K., Nolan, P. J. & Twelves, J. A. 1982 *Corros. Sci.* **22**, 37–50.
Goodison, D. & Harris, R. J. 1969 *Br. Corros. J.* **4**, 146–153.
Hagel, W. C. 1965 *J. appl. Phys.* **36**, 2596–2597.
Hales, R. & Smith, A. F. 1974 *CEGB Report* No. RD/B/N2938.
Harrison, P. L. 1976 *CEGB Report* No. RD/L/R/933.
Hay, K. A., Hicks, F. G. & Holmes, D. R. 1970 *Werkstoffe Korros., Mannheim.* **21**, 917–921.
Hobby, M. G. & Wood, G. C. 1969 *Oxidat. Metals* **1**, 23–54.
Hultquist, G. & Leygraf, C. 1982 *Corros. Sci.* **22**, 331–346.
Jepson, W. B., Antill, J. E. & Warburton, J. B. 1965 *Br. Corros. J.* **1**, 15–25.
Kehrer, W. J. & Leidheiser, H. 1954 *J. phys. Chem.* **58**, 550–561.
Kofstad, P. 1972 *Non-stoichiometry, diffusion and electrical conductivity in binary metal oxides*, p. 207. New York: Wiley-Interscience.
Kofstad, P. 1981 In *6th N.A.C.E. conference on high temperature corrosion* (ed. R. A. Rapp), p. 123. Houston, Texas: National Association of Corrosion England.
Kubaschewski, O. & Evans, E. 1958 *Metallurgical thermochemistry* 2nd ed. London: Pergamon.
Kubaschewski, O. & Hopkins, B. E. 1967 *Oxidation of metals and alloys* 1st ed. London: Butterworths.
Leygraf, C. & Hultquist, G. 1975 In *Proc. 6th international congress on metallic corrosion.* Sydney.
Lloyd, G. O., Saunders, S. R. J., Kent, B. & Fursey, A. 1977 *Corros. Sci.* **17**, 269–299.
Lucke, K. & Stuwe, H. P. 1971 *Acta metall.* **19**, 1087–1099.
Majorandorany, F. N. & Pehlke, R. D. 1974 *J. electrochem. Soc.* **121**, 711–714.
Meijerling, J. L. 1971 *Adv. mater. Sci.* **5**, 1–39.
Mortimer, D. & Post, M. L. 1968 *Corros. Sci.* **8**, 499–512.
Mortimer, D. & Sharp, W. B. A. 1968 *Br. Corros. J.* **3**, 61–67.
Newcomb, S. B. & Stobbs, W. M. 1982 *Electron microscopy and analysis 1981* (ed. M. J. Goringe), pp. 379–381. Bristol: Institute of Physics.
Newcomb, S. B. 1983 Ph.D. thesis, University of Cambridge.
Newcomb, S. B., Smith, D. J. & Stobbs, W. M. 1983 *J. Microsc.* **130**, 137–146.

Newcomb, S. B. & Stobbs, W. M. 1983 *J. Microsc.* **130**, 233–248.
Newcomb, S. B. 1984 In *Proceedings of 42nd annual meeting EMSA* (ed. G. W. Bailey), p. 612. Baton Rouge: Claitors.
Newcomb, S. B., Boothroyd, C. B. & Stobbs, W. M. 1985 *J. Microsc.* **140**, 195–208.
Richardson, F. D. & Jeffes, J. H. E. 1948 *J. Iron Steel Inst.* **160**, 261–270.
Richardson, F. D., Jeffes, J. H. E. & Withers, G. 1950 *J. Iron Steel Inst.* **166**, 213–234.
Richardson, F. D. 1953 *J. Iron Steel Inst.* **175**, 33–51.
Rowlands, P. C. & Manning, M. I. 1980 *CEGB Report* No. RD/L/N4680.
Seybolt, A. U. 1960 *J. electrochem. Soc.* **107**, 147–156.
Stobbs, W. M., Newcomb, S. B. & Metcalfe, E. 1986 A microstructural study of the oxidation of Fe–Ni–Cr alloys II: 'non-protective' oxide growth. *Phil. Trans. R. Soc. Lond.* A **319**, 219–247.
Tempest, P. A. & Wild, R. K. 1981 *CEGB Report* No. RD/B/5013/N81.
Turner, D. J. 1980 *CEGB Report* No. RD/L/N33/80.
Wagner, C. 1956 *J. electrochem. Soc.* **103**, 627–633.
Whittle, D. P. & Wood, G. C. 1967 *J. electrochem. Soc.* **114**, 986–993.
Wild, R. K. 1977 *Corros. Sci.* **17**, 87–104.
Wood, G. C. 1961 *Corros. Sci.* **2**, 173–196.
Wood, G. C. & Whittle, D. P. 1964 *Corros. Sci.* **4**, 263–292.
Wood, G. C., Hodgkeiss, T. & Whittle, D. P. 1966 *Corros. Sci.* **6**, 129–147.
Wood, G. C. & Whittle, D. P. 1967 *Corros. Sci.* **7**, 763–782.
Young, D. J. & Mitchell, D. F. 1979 *Oxidat. Metals* **13**, 437–456.

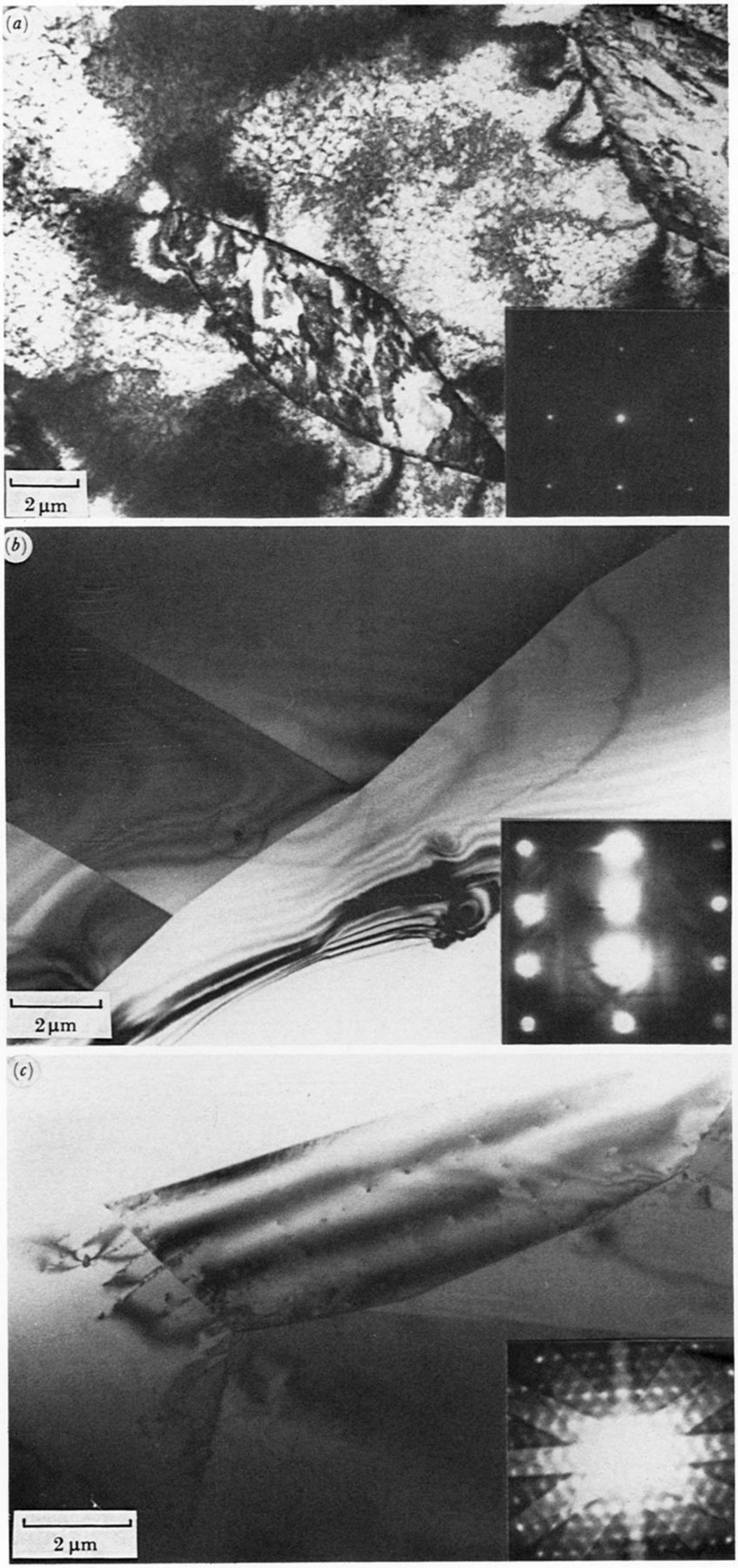

FIGURE 2. Microstructures of the Fe–20Cr–Ni alloys before oxidation. BF TEM. (*a*) Fe–20Cr–2Ni diffraction plane: $(001)_\alpha$; (*b*) Fe–20Cr–20Ni diffraction plane: $(112)_\gamma$; (*c*) Fe–20Cr–34Ni diffraction plane: $(112)_\gamma$.

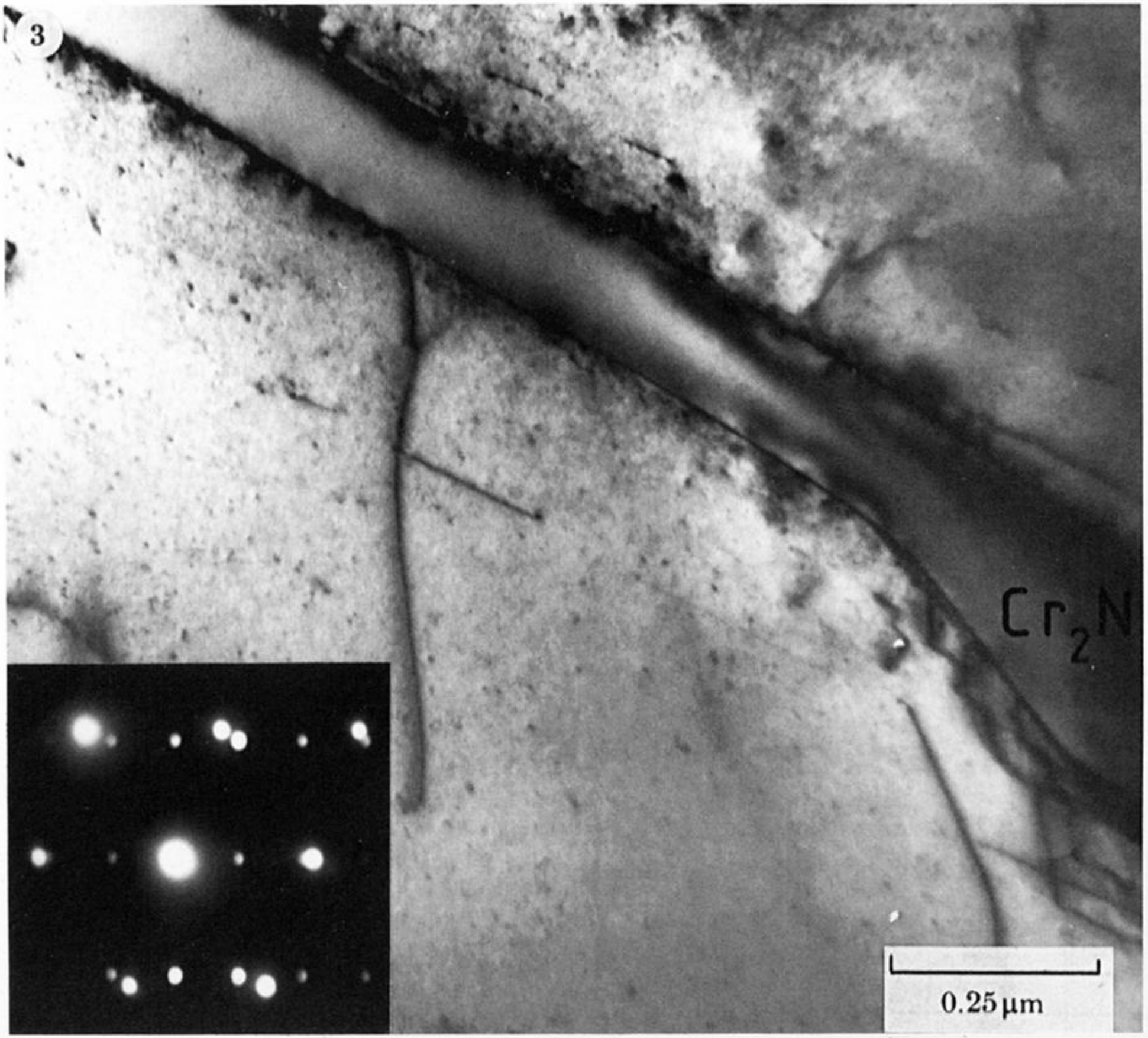

FIGURE 3. A β-Cr_2N nitride lying *ca.* 25 μm beneath the surface of an Fe–20Cr–20Ni alloy after the surface treatment described in the text. The bright-field micrograph was obtained near to the $(110)_\gamma|(2\bar{1}\bar{1}0)_{Cr_2N}$ normals shown in the inset diffraction pattern.

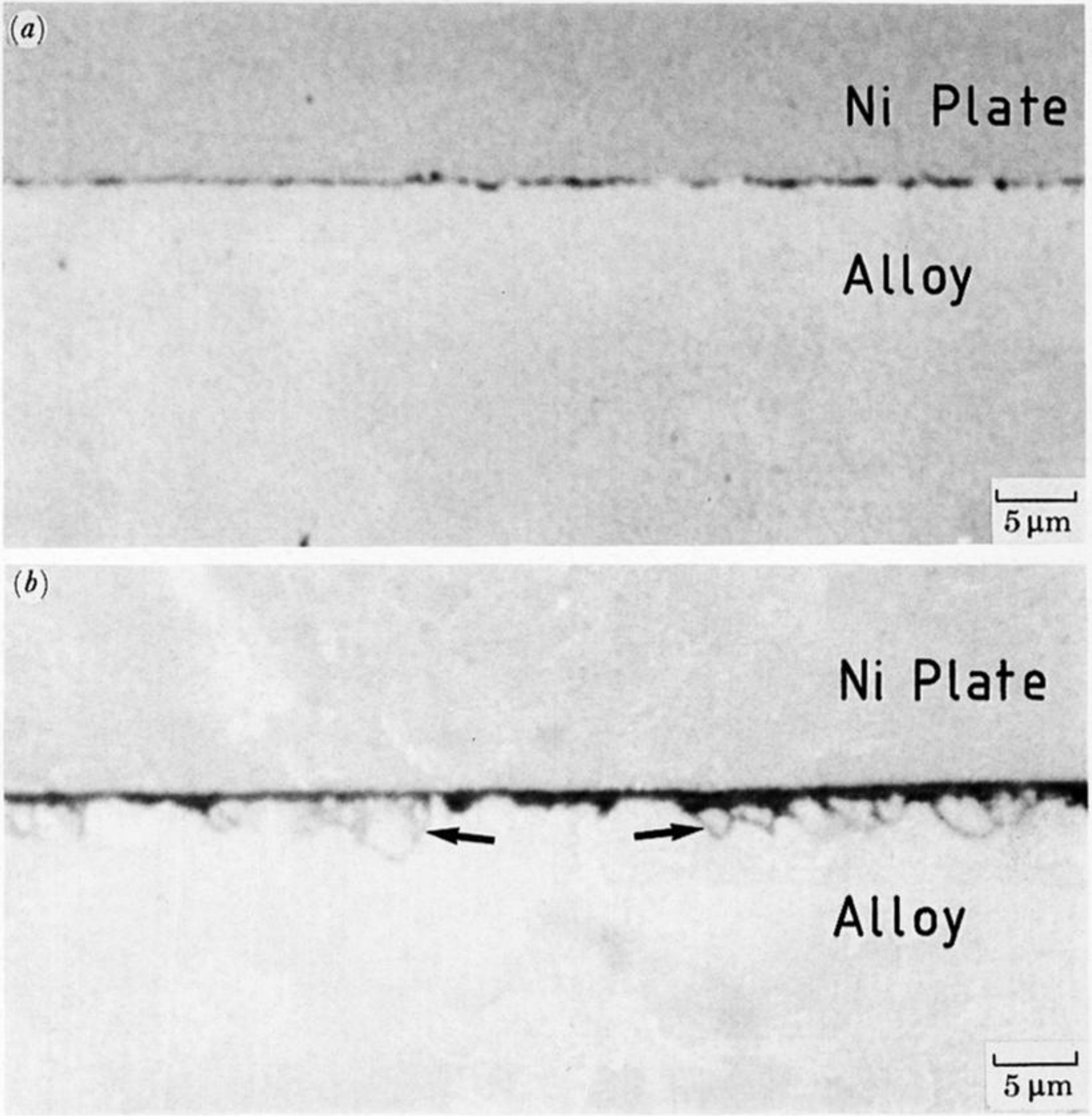

FIGURE 5. Optical micrographs of the scales formed after 1000 h oxidation at 600 °C on: (*a*) Fe–20Cr–20Ni in air and (*b*) Fe–20Cr–34Ni in 1 % CO–CO_2. Regions of the alloy beneath the scale where carbide precipitation has occurred are arrowed.

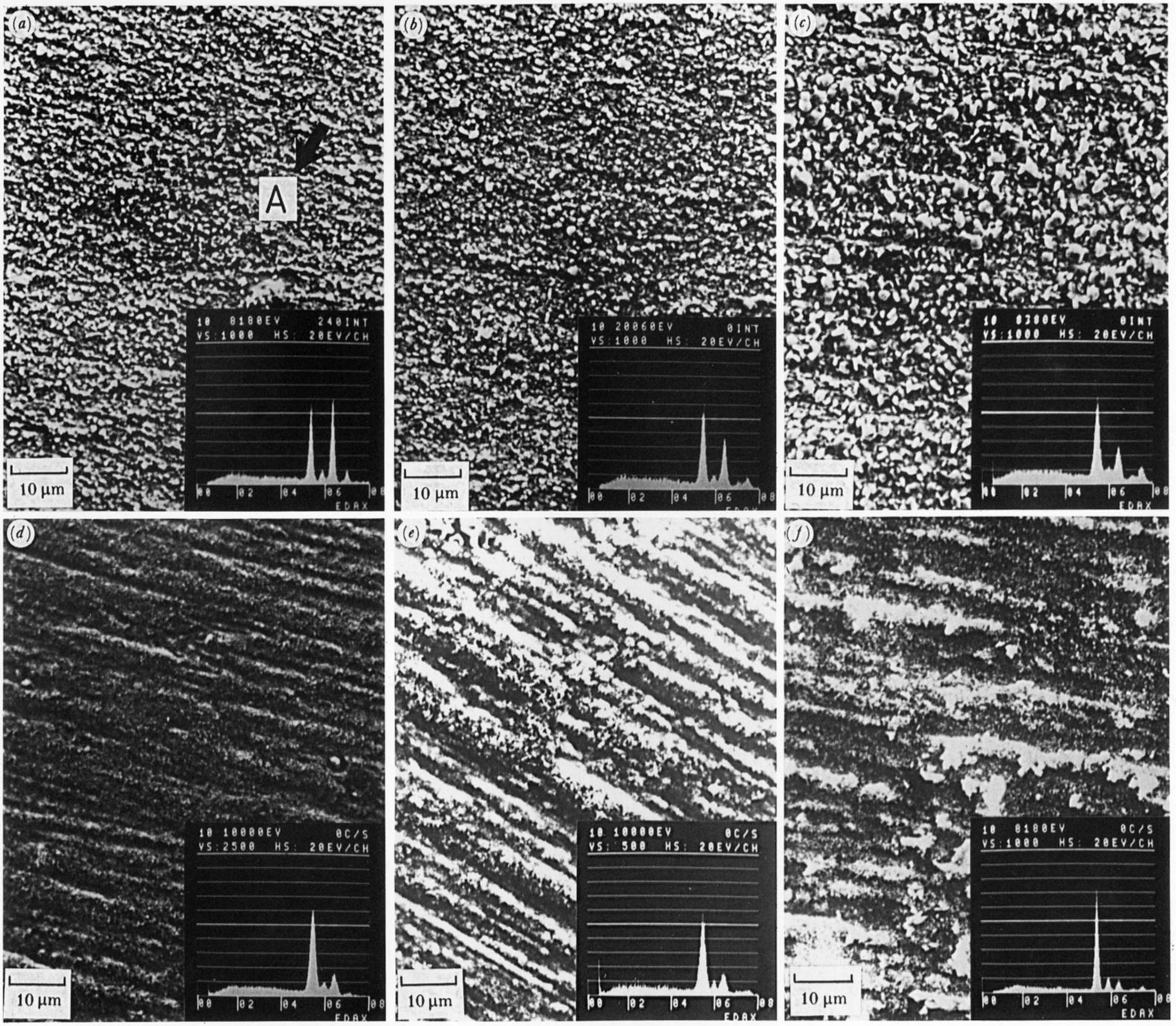

FIGURE 6. Scanning electron micrographs and 20 kV EDX analyses (Cr: 5.411, Fe: 6.398, Ni: 7.47 keV) of the surfaces of the oxides formed in air (*a*)–(*c*) and in CO–CO_2 (*d*)–(*f*) for 1000 h at 600 °C.

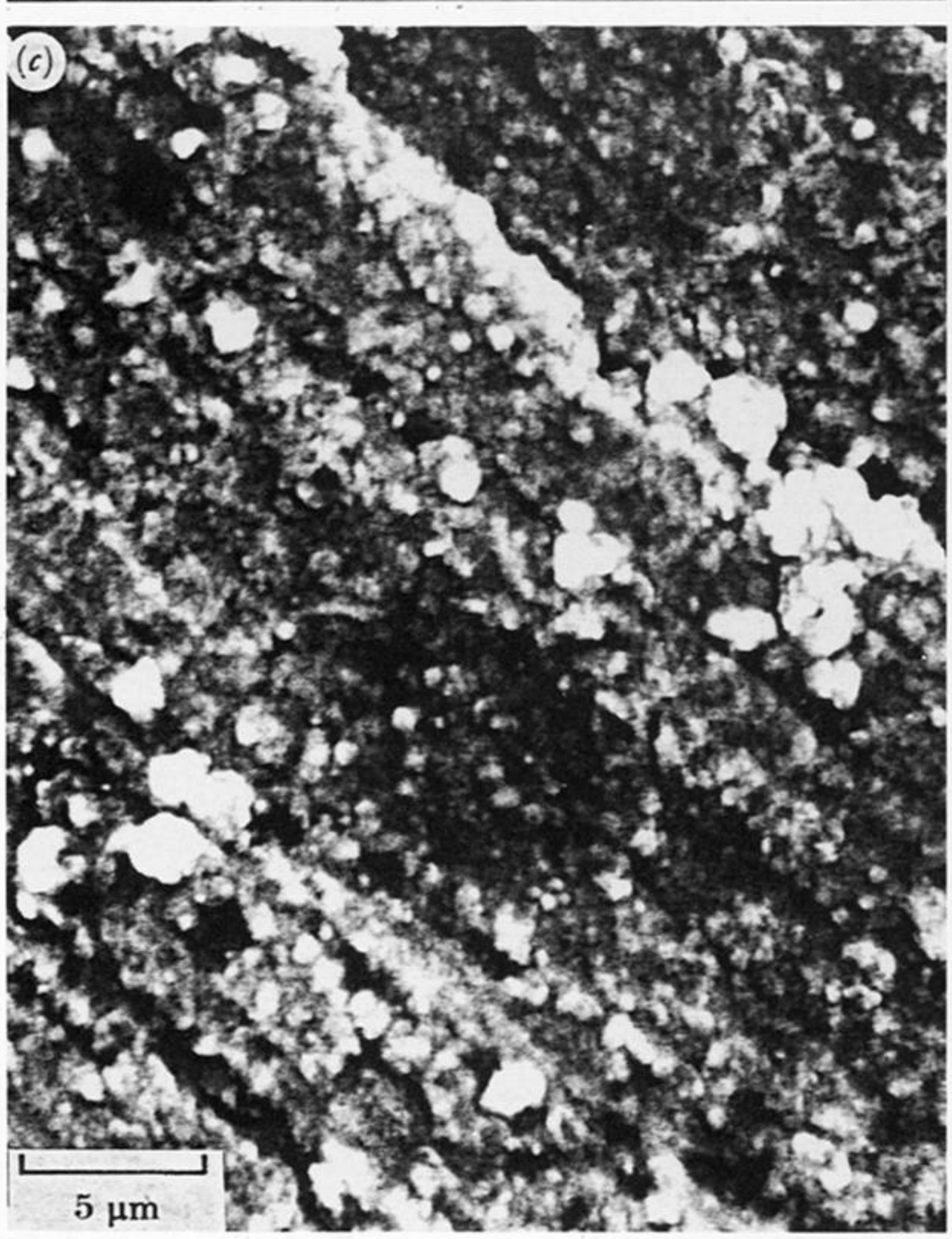

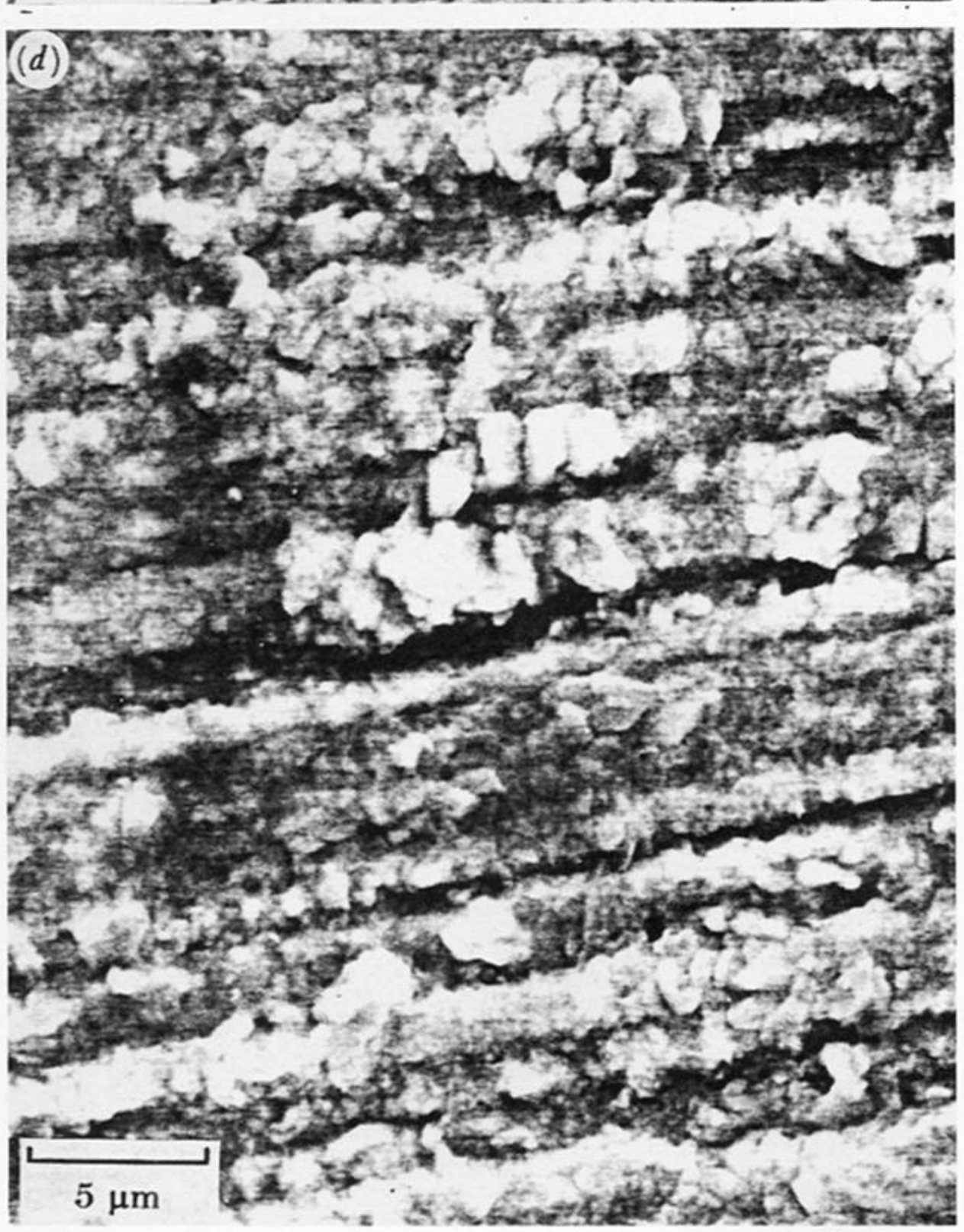

FIGURE 7. Scanning electron micrographs of the Fe–20Cr–34Ni alloy (*a*) before oxidation and the surface the oxides formed after (*b*) 30 min, (*c*) 2 h and (*d*) 17.5 h in air at 600 °C. It may be noted that the post-anneal grinding treatment is reflected in the form of the developing scale.

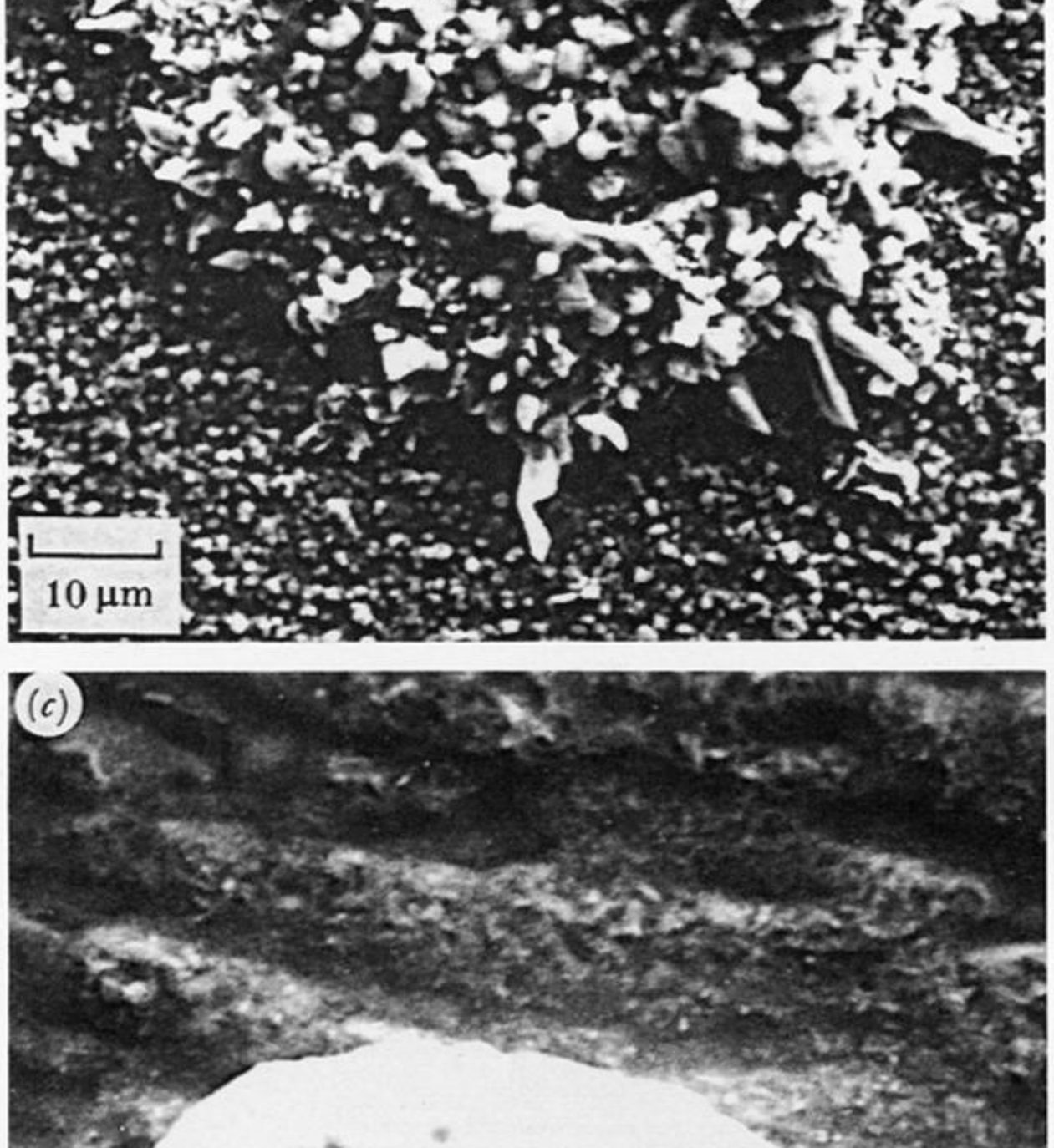

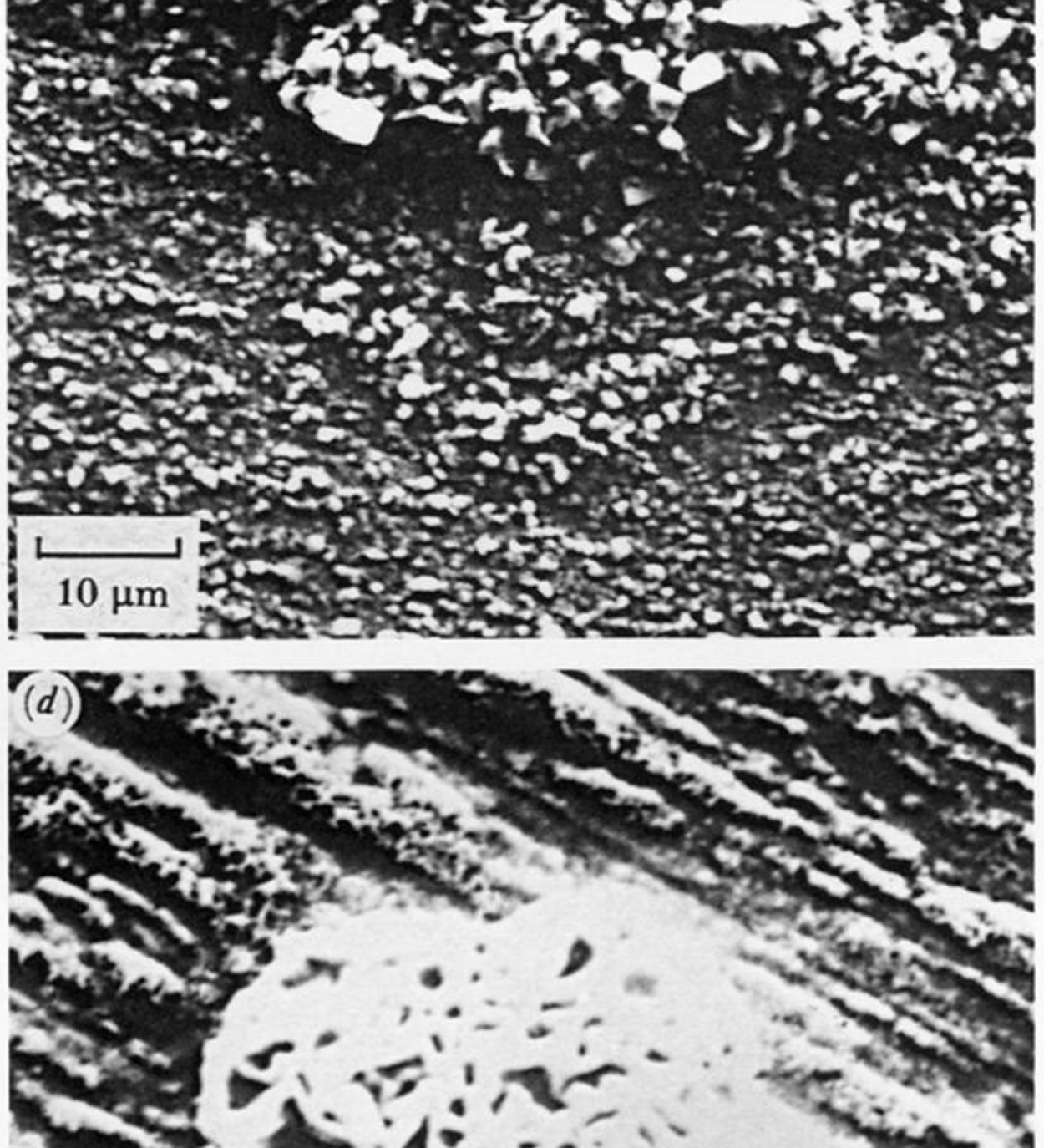

FIGURE 8. Scanning electron micrographs showing the morphologies of oxide nodules formed on (*a*) Fe–20Cr–2Ni and (*b*) Fe–20Cr–20Ni in air, and on (*c*) Fe–20Cr–2Ni and (*d*) Fe–20Cr–20Ni in CO–CO_2 after 1000 h at 600 °C.

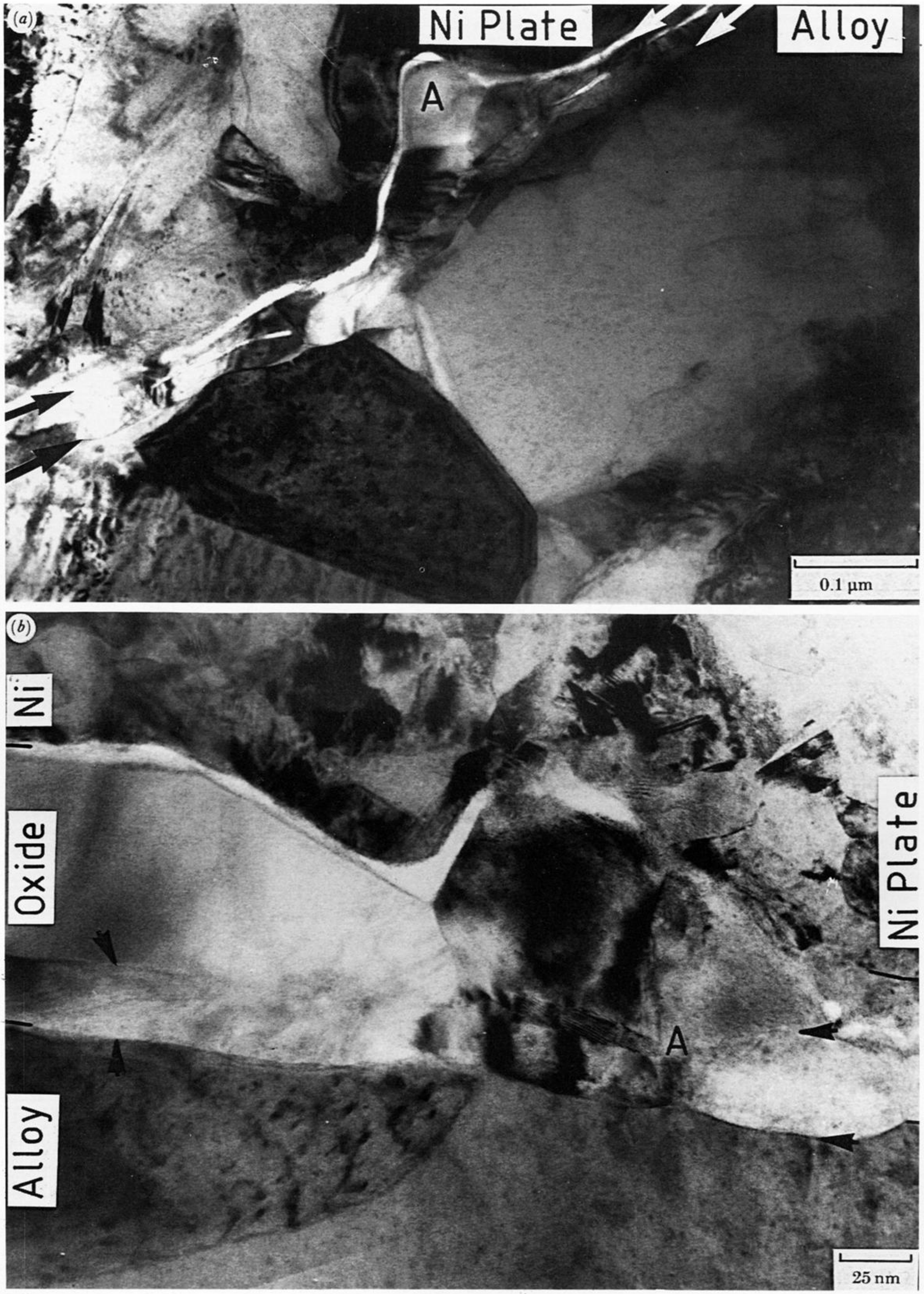

FIGURE 9. Fe–20Cr–34Ni oxidized for 6 h in air at 600 °C. 'Edge-on' bright-field micrographs showing (*a*) a low magnification image of a thin oxide layer (M_2O_3) sandwiched between the alloy and nickel plate, as arrowed (note the relatively fine alloy grains immediately beneath the scale); (*b*) a higher magnification image of the two-layered oxide morphology where the thinner and innermost layer is delineated by arrows (note the cusped morphology of the scale at the alloy–oxide and oxide–nickel plate interfaces).

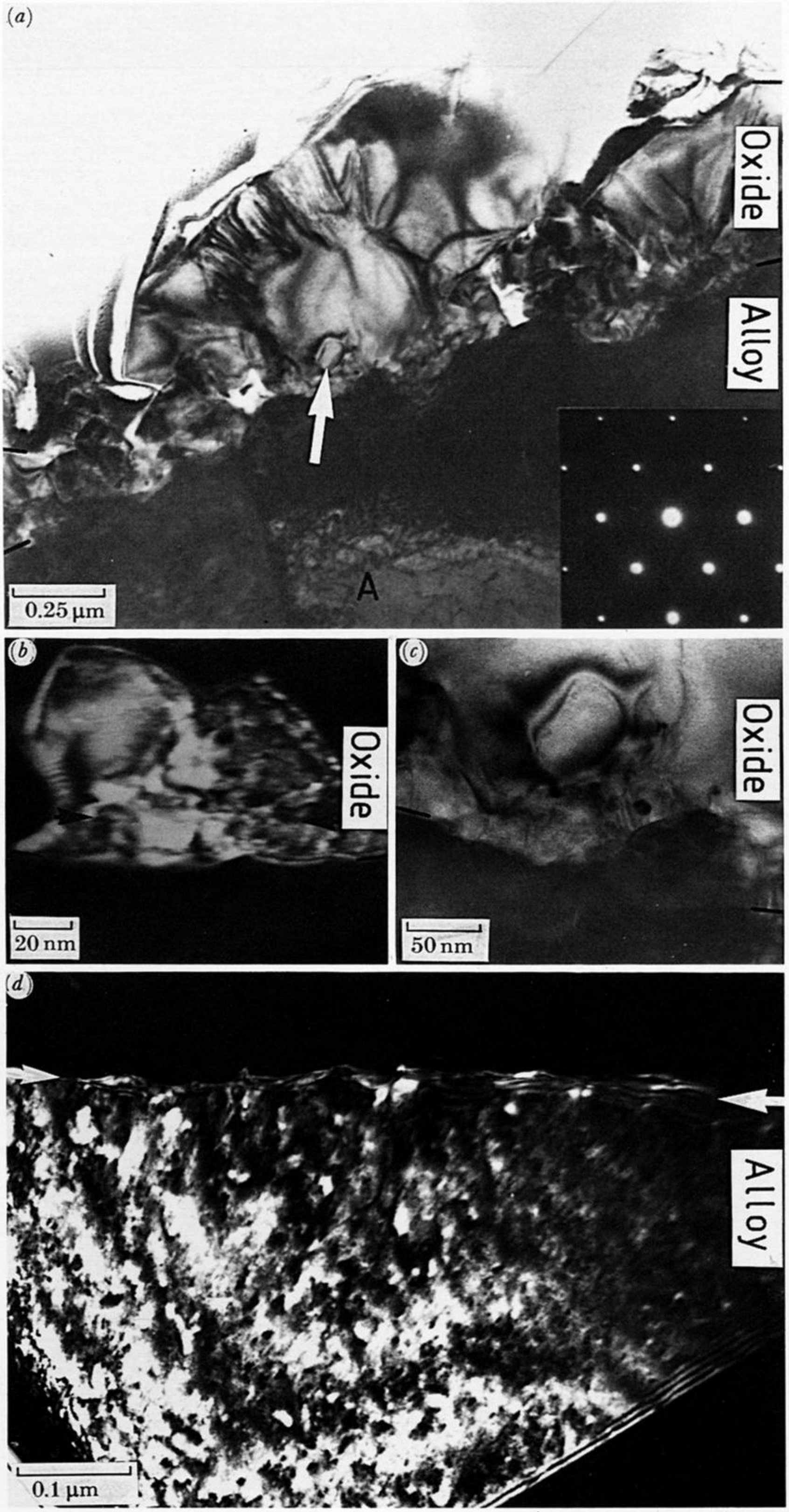

FIGURE 10. Fe–20Cr–34Ni oxidized for 1000 h in air at 600 °C. 'Edge-on' TEM. (*a*) Bright-field micrograph showing large faceted Cr_2O_3 grains and the underlying alloy (the inset is a (011) austenite diffraction pattern) which in some regions is dislocated, as at A. A 75 nm oxide grain near the metal–oxide interface is arrowed. (*b*) Dark-field micrograph showing the two-layered morphology of the scale. An interface between the oxide layers is arrowed. (*c*) Higher magnification image of fine grained oxide at the metal–oxide interface, bright field. (*d*) Dark-field micrograph demonstrating the more fully recovered alloy microstructure beneath the scale. The arrows delineate the metal–oxide interface, which is both inclined and clearly cusped.

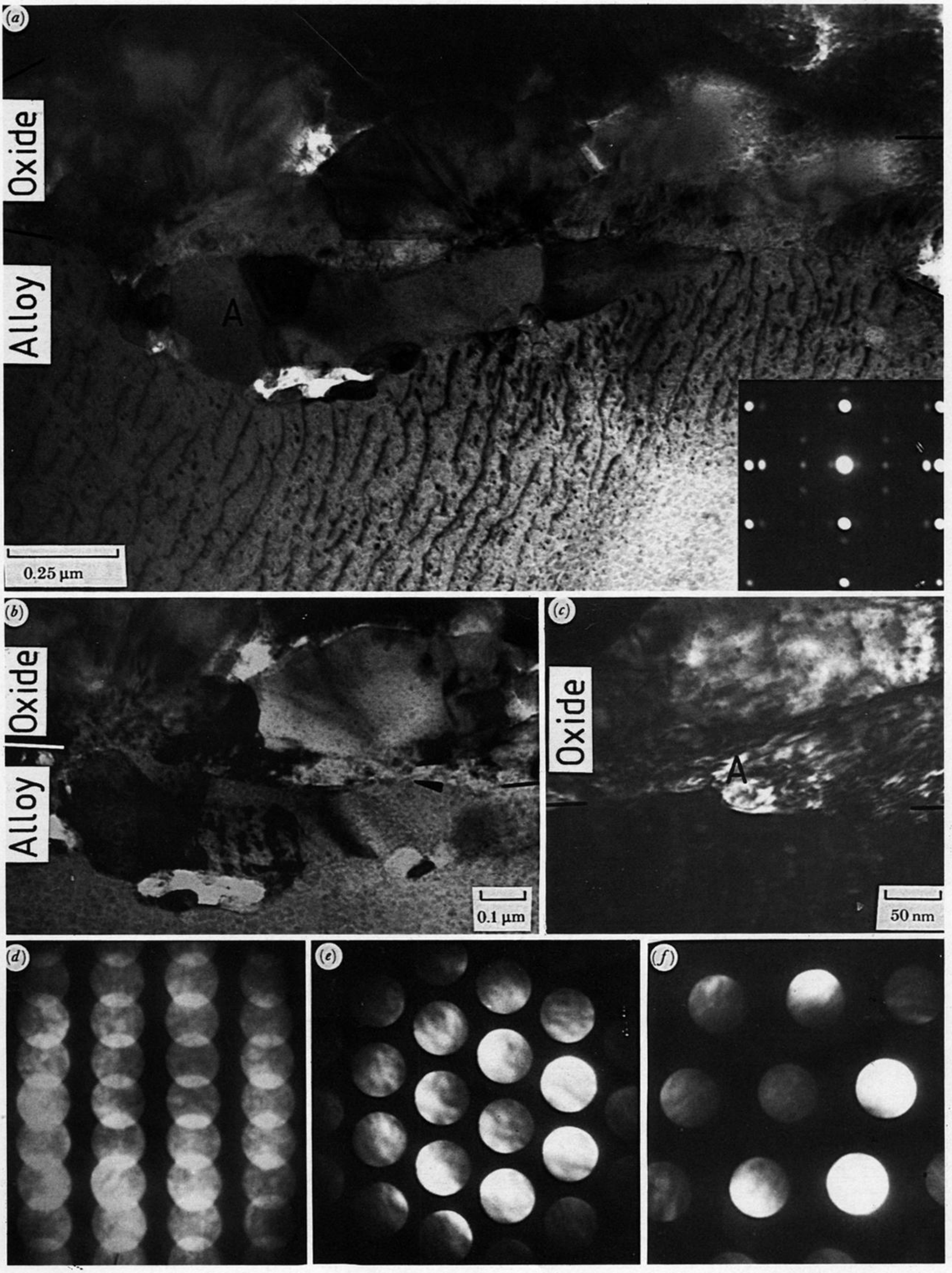

FIGURE 12. Fe–20Cr–20Ni oxidized in air for 1000 h at 600 °C. (*a*) Bright-field micrograph of the scale and underlying oxide. The outer surface of the faceted oxide grains are covered with sputter contamination from the ion beam milling while the surface of the alloy is partly oxidized, as demonstrated by the inset $(112)_{\gamma}//(112)_{M_3O_4}$ diffraction pattern. (*b*) The metal–oxide interface where a discrete layer (*ca.* 50 nm) of fine-grained oxide is arrowed, bright-field. (*c*) Dark-field micrograph showing the cusped morphology of the scale at the metal–oxide interface, as at A. (*d*) $(211)_{Cr_2O_3}$ diffraction pattern. (*e*) (011) austenite diffraction pattern taken from the fine-grained alloy immediately beneath the oxide, as at A in (*a*).

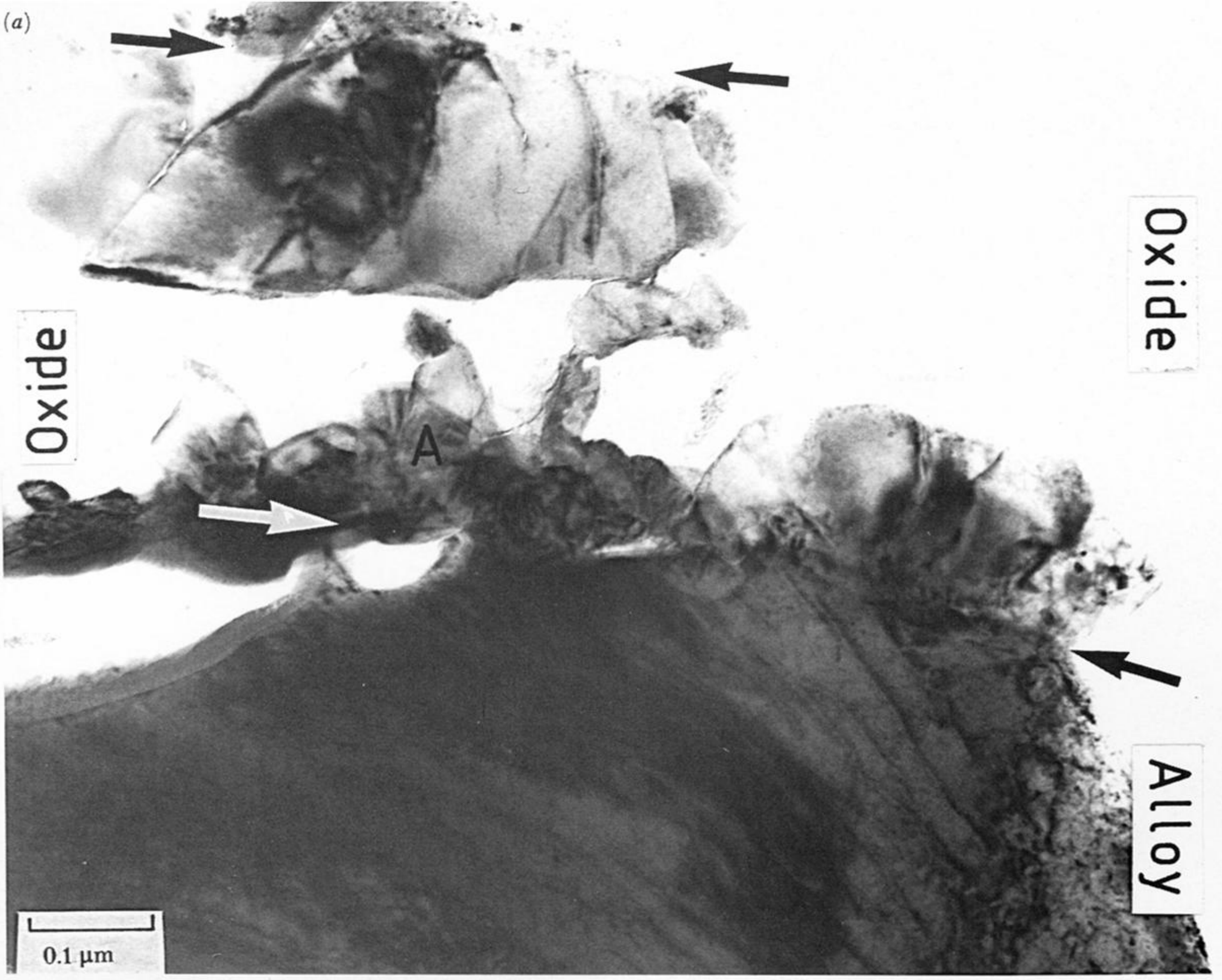

FIGURE 14. Fe–20Cr–2Ni oxidized in air for 1000 h. (*a*) Bright-field micrograph showing the scale and underlying alloy. Note the comparatively 'open' morphology of the scale (see figure 6*a*) and the fine oxide grains at the metal–oxide interface, as at A. (*b*) Dark-field micrograph showing the cusped morphology of the metal–oxide interface (arrowed) which is inclined. The surface of the ferrite has also been partly oxidized during the preparation of the foil, as indicated by the moiré fringes.

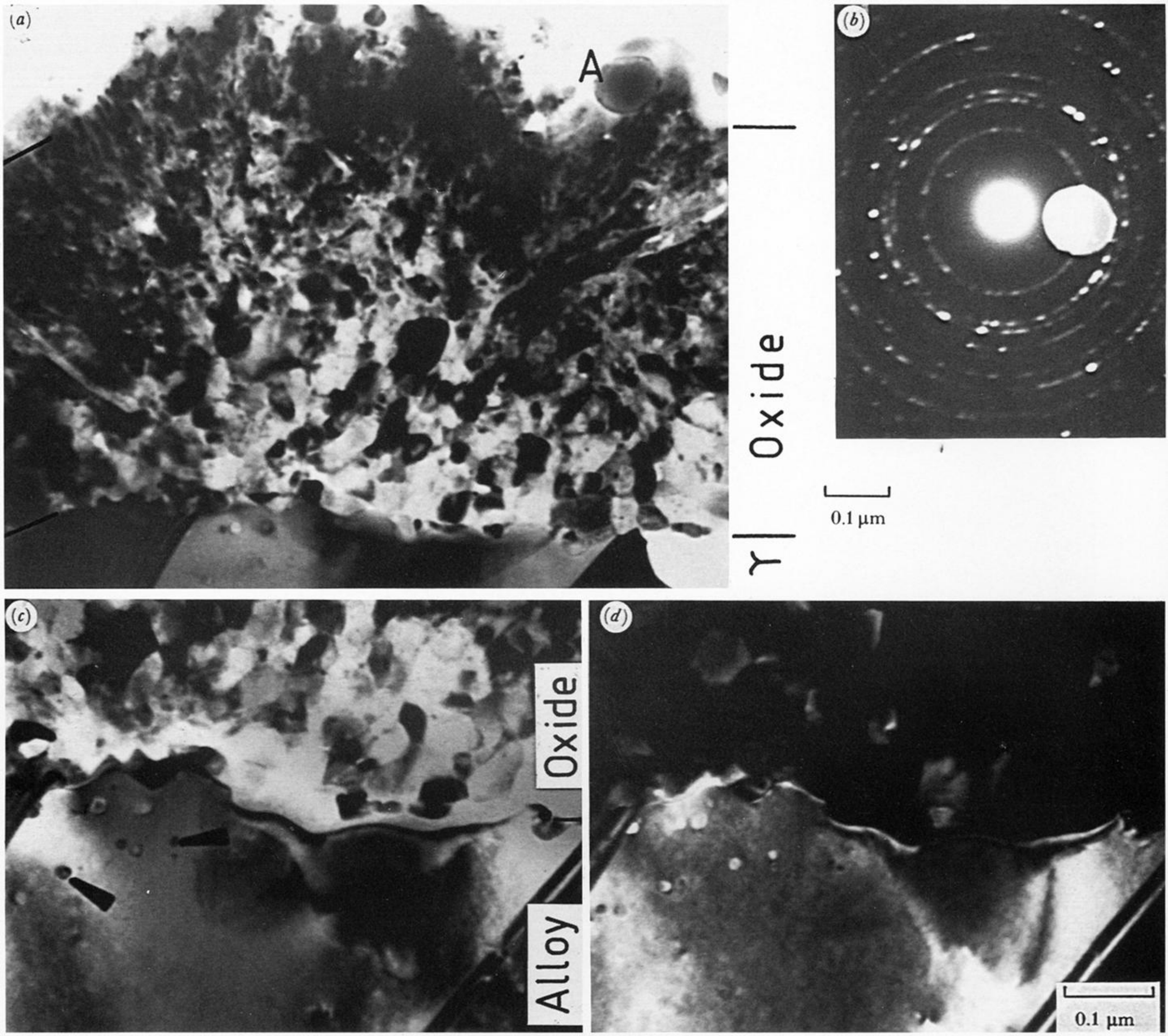

FIGURE 16. Fe–20Cr–34Ni oxidized in 1% CO–CO_2 for 1000 h at 600 °C. 'Edge-on' TEM. (*a*) Bright-field micrograph showing the scale morphology. Note the progressive change in morphology towards the oxide gas interface, which in some regions is sputter contaminated from ion beam thinning, as at A. (*b*) α-M_2O_3 diffraction pattern. (*c*) Bright-field and (*d*) dark-field micrograph (imaged with an austenite reflection) showing the cusped morphology of the metal–oxide interface. The arrowed particles in (*c*) are again sputter contamination.

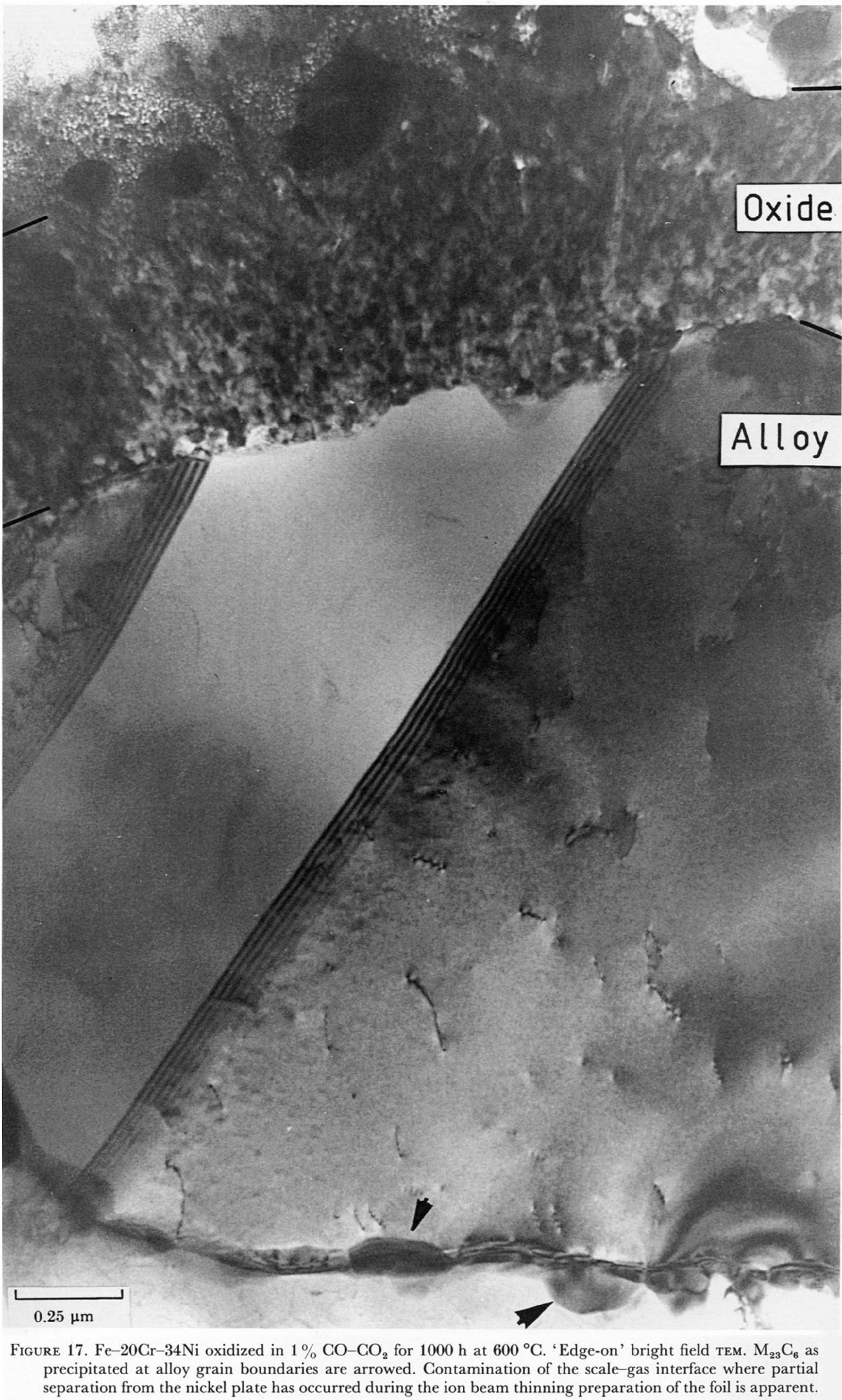

FIGURE 17. Fe–20Cr–34Ni oxidized in 1 % CO–CO_2 for 1000 h at 600 °C. 'Edge-on' bright field TEM. $M_{23}C_6$ as precipitated at alloy grain boundaries are arrowed. Contamination of the scale–gas interface where partial separation from the nickel plate has occurred during the ion beam thinning preparation of the foil is apparent.

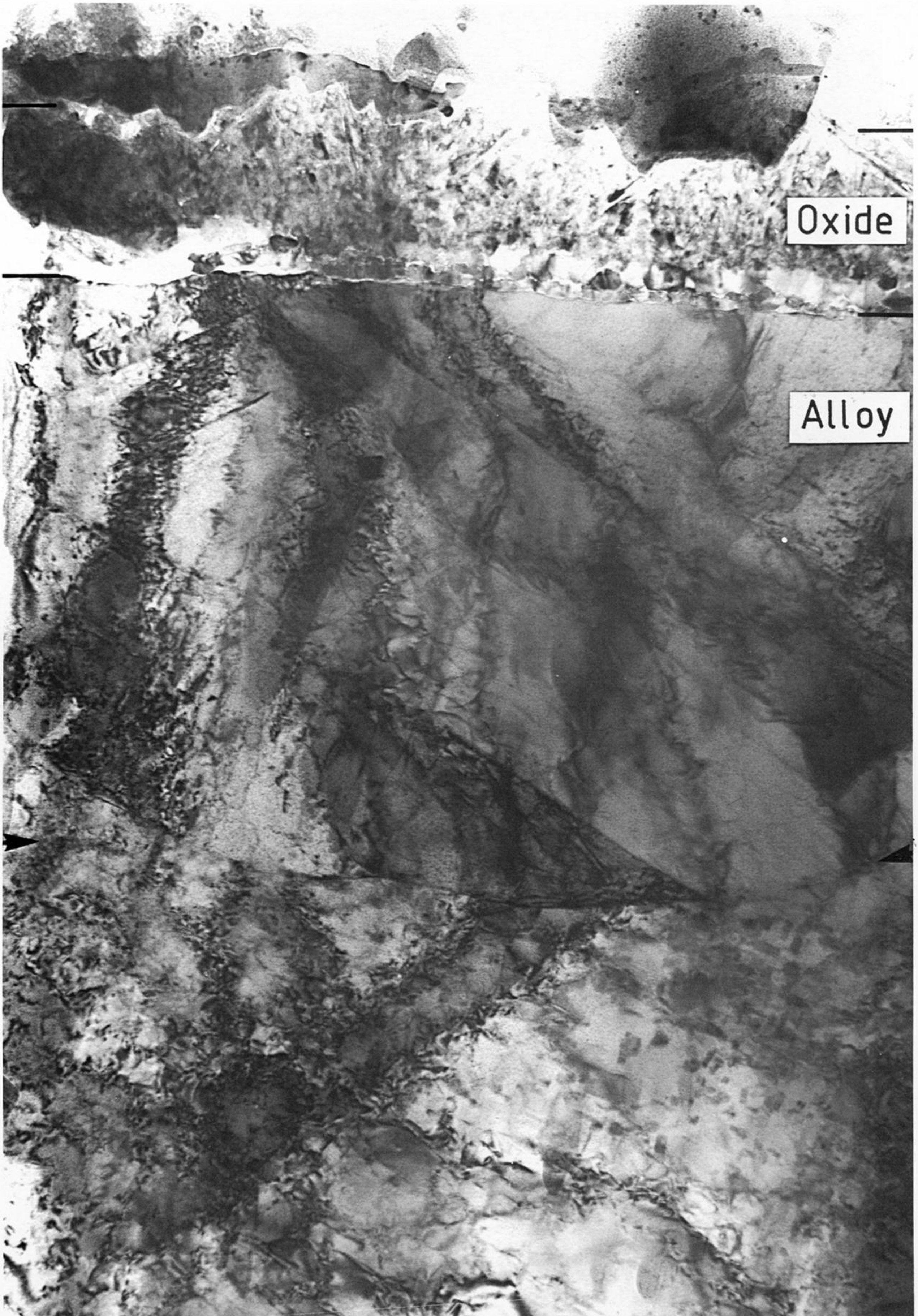

FIGURE 19. Fe–20Cr–20Ni oxidized in 1 % CO–CO_2 for 1000 h at 600 °C. 'Edge-on' bright-field TEM. The interface between the recrystallized austenite, which extends for *ca.* 1 μm beneath the scale, and the bulk of the alloy is arrowed. Note the equiaxed oxide grains at the metal–oxide interface which give the scale a two-layered appearance.

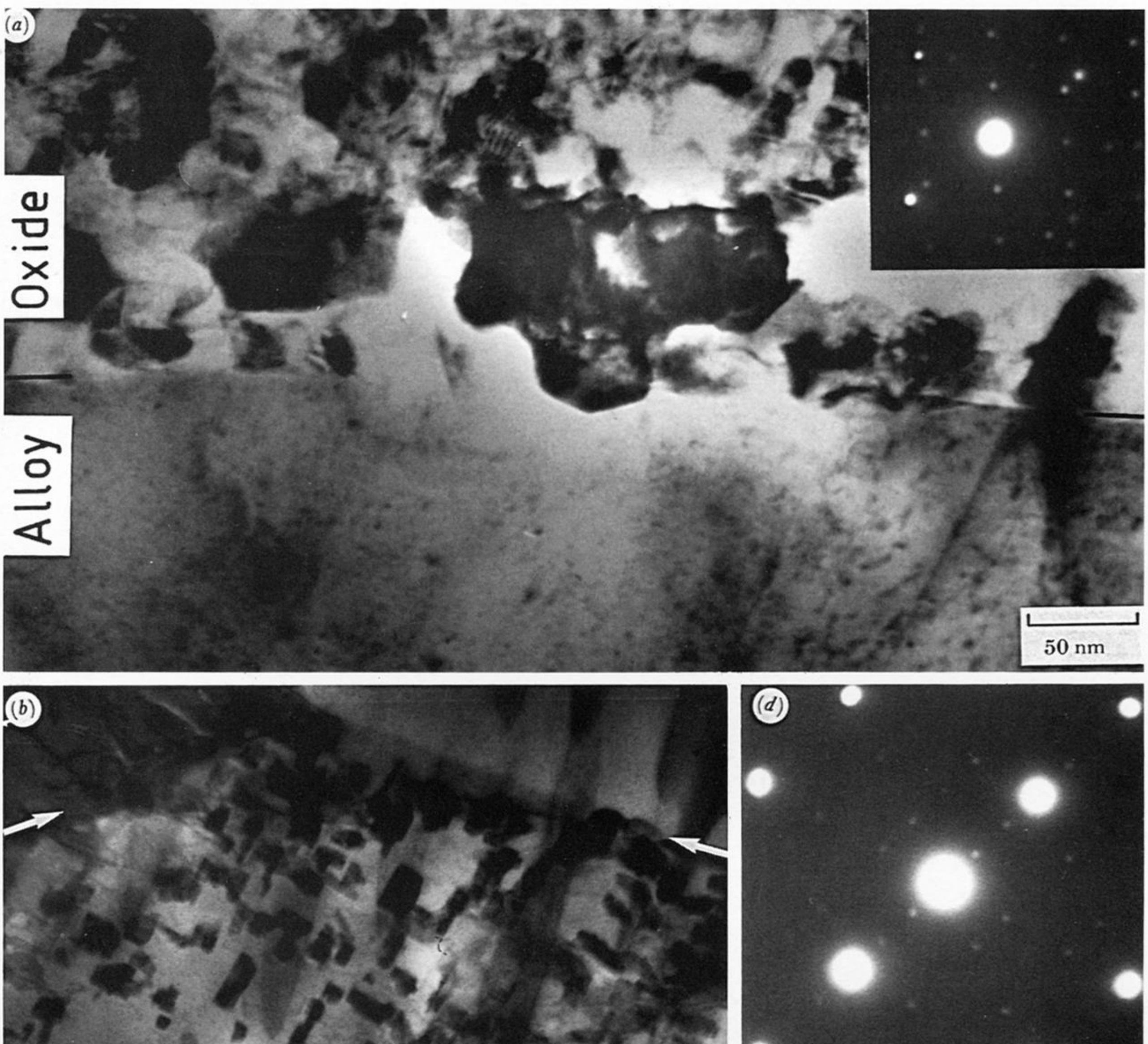

FIGURE 20. Fe–20Cr–20Ni oxidized in 1 % CO–CO_2 for 1000 h at 600 °C. (*a*) Bright-field micrograph of the alloy scale interface showing equiaxed oxide grains which again have a cusped morphology. The inset shows a $(\bar{1}2\bar{1}6)_{Cr_2O_3}$ diffraction pattern. (*b*) Bright-field and (*c*) dark-field micrograph (imaged with a (200) carbide reflection showing $M_{23}C_6$ precipitates in the alloy. The interface between the recrystallized and bulk alloy (see figure 19) is arrowed in (*b*) and (*c*). It is apparent that carbide precipitation has not occurred in the recrystallized region of the alloy. (*d*) $(310)_\gamma // (310)_{M_{23}C_6}$ diffraction pattern.

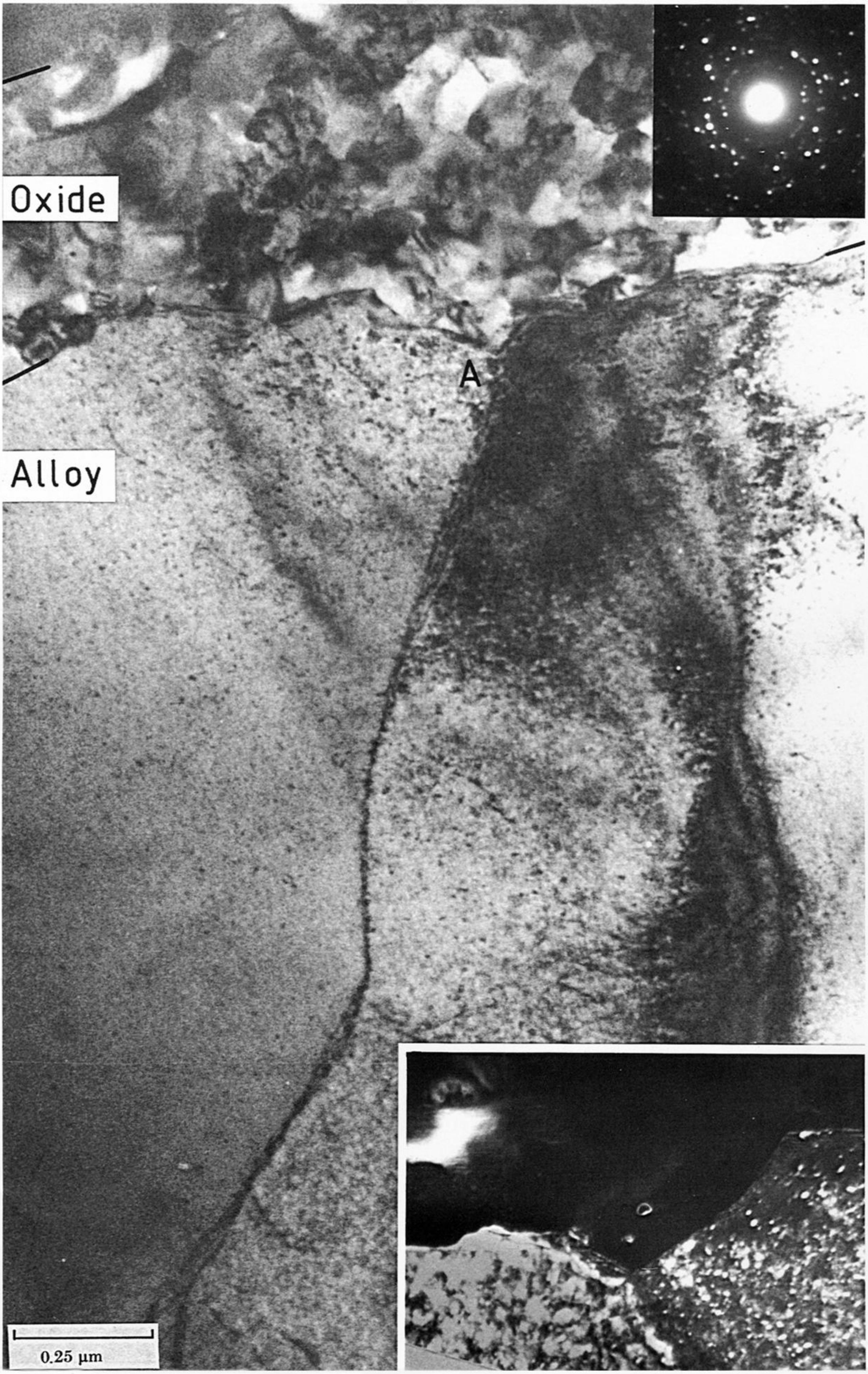

FIGURE 22. Fe–20Cr–2Ni oxidized in 1 % CO–CO_2 for 1000 h at 600 °C. 'Edge-on' bright-field TEM. Partial growth of the fine-grained oxide into the metal has occurred at the alloy grain boundary, as at A, a region which is shown enlarged in the inset dark field micrograph (imaged with a ferrite reflection). Carbide precipitation in either the alloy or the scale is not apparent.

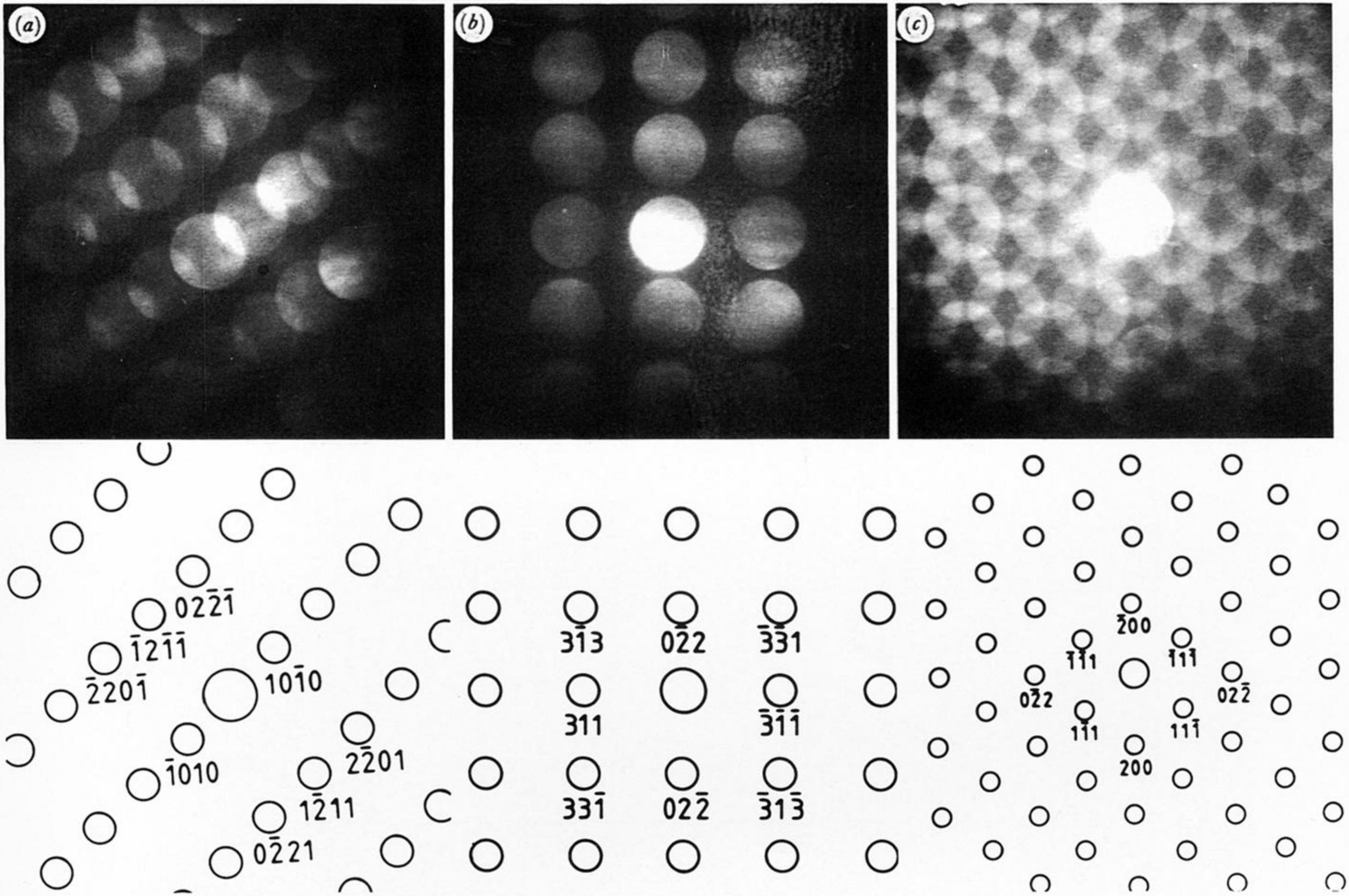

FIGURE 23. Diffraction patterns from the 'protective' scale formed on Fe–20Cr–2Ni in 1 % CO–CO_2 after 1000 h at 600 °C showing α-sesquioxide and cubic oxide phases. (*a*) $(\bar{1}2\bar{1}6)_{M_2O_3}$, (*b*) $(233)_{M_3O_4}$, (*c*) $(011)_{M_3O_4}$.

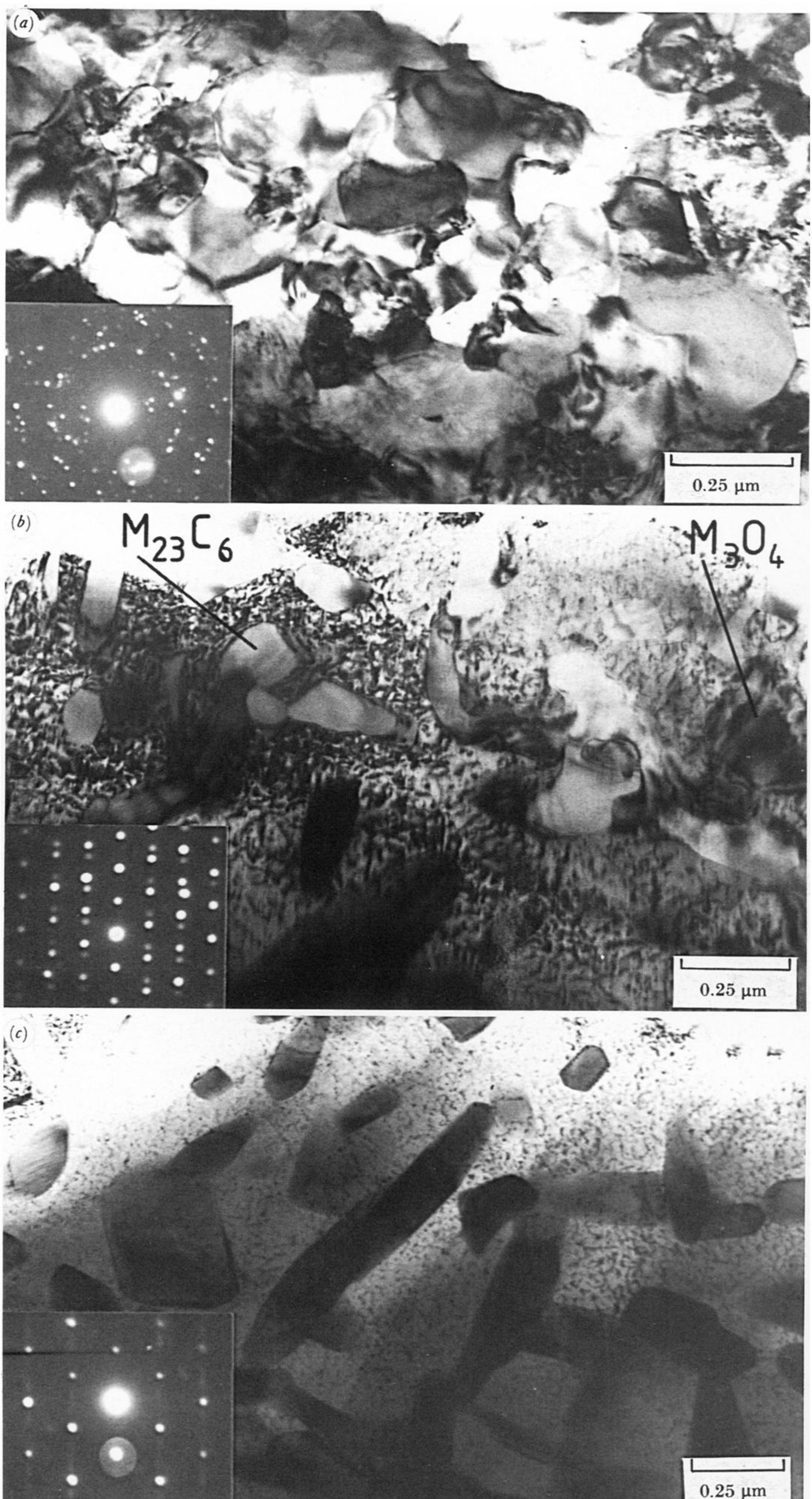

FIGURE 25. Fe–20Cr–2Ni oxidized for 1000 h in 1 % $CO–CO_2$ at 600 °C. 'Edge-on' bright-field micrographs showing the microstructure of the 'non-protective' and inward grown scale formed beneath 'hopper' magnetite. (*a*) Fine-grained spinel (see inset diffraction pattern) approximately 5 μm from the duplex oxide interface. (*b*) Approximately 10 μm beneath the duplex oxide interface. M_3O_4 spinel grains encapsulating ferrite, beneath which $M_{23}C_6$ carbides have been precipitated in the alloy. The inset shows a twinned $(011)_{M_3O_4}$ diffraction pattern. (*c*) Coarse $M_{23}C_6$ precipitates in the alloy approximately 5 μm beneath the region shown in (*b*). The inset shows an $(011)_{M_{23}C_6}$ diffraction pattern, which exhibits streaking indicative of internal faulting in the carbides.